

Doctoral Dissertation

博士論文

**Probing the Evolution of Massive Galaxies with Millimeter-wave  
Emission Lines**

(ミリ波輝線を用いた大質量銀河の進化の調査)

A Dissertation Submitted for the Degree of Doctor of Philosophy

December 2023

令和5年12月博士(理学)申請

Department of Astronomy, Graduate School of Science, The University of Tokyo

東京大学大学院理学系研究科 天文学専攻

Shuo Huang

黄 燦

## Acknowledgement

I am grateful to my supervisors, Ryohei Kawabe and Kotaro Kohno, who have taken a large amount of time to discuss research related to this thesis and supported my graduate life. I thank the referees for their helpful comments and discussion: Kentaro Motohara (chair), Naoto Kobayashi, Ryouhei Kano, Norio Kuno, and Hidenobu Yajima. I would like to thank the co-authors of the two papers based on the contents of this thesis for their valuable comments and suggestions: Hideki Umehata, Minju Lee, Yoichi Tamura, Bunyo Hatsukade, Ken Mawatari, Toshiki Saito, Shoichiro Mizukoshi, Daisuke Iono, Tomonari Michiyama and Christopher C. Hayward. I would like to give special thanks to Shun Ishii for his help in ALMA observations. Finally, I would like to thank people who spent with me in Room 2016, Institute of Astronomy, The University of Tokyo : Noriaki Arima, Akiyoshi Tsujita, Ryotaro Koshi and Taiga Sasaoka.

The main contents of Sections 2 and 3 in this thesis have been published in the *Astrophysical Journal* and the *Astrophysical Journal Letters*, which make use of the following ALMA data: ADS/JAO.ALMA #2013.1.00469.S, #2013.1.01057.S, #2015.1.00973.S, #2015.1.00902.S, #2013.1.00740.S, #2019.1.01102.S, #2021.1.01207.S, and #2023.1.01262.S. ALMA is a partnership of ESO (representing its member states), NSF (USA), and NINS (Japan), together with NRC (Canada), MOST and ASIAA (Taiwan), and KASI (Republic of Korea), in cooperation with the Republic of Chile. The Joint ALMA Observatory is operated by ESO, AUI/NRAO, and NAOJ. Herschel is an ESA space observatory with science instruments provided by European-led Principal Investigator consortia and with important participation from NASA. This thesis uses data from the Karl G. Jansky Very Large Array operated by the National Radio Astronomy Observatory under project VLA/23B-024. The National Radio Astronomy Observatory is a facility of the National Science Foundation operated under cooperative agreement by Associated Universities, Inc.

## Abstract

Spectroscopic observations of galaxies in the distant universe provide essential information for elucidating their formation and evolution. This is especially relevant to the most massive galaxies with stellar mass  $\gtrsim 10^{11} M_{\odot}$  because they have been actively forming stars at  $z \sim 2-3$ , a period called cosmic noon. Historically, spectroscopy of high-redshift galaxies has been done mainly in optical and near-infrared bands. Such observations are very time-consuming, and more importantly, may suffer from the heavy dust obscuration in high-redshift dusty star-forming galaxies. Emission lines at millimeter (mm)/submillimeter (submm) wavelength provide a window to overcome the dust extinction and look into the structure of these galaxies during their assembly phase. In the past two decades, much progress has been made in both observations of mm/submm emission lines from high-redshift galaxies and theoretical works for the interpretation of the results. However, targeted mm line surveys may have biased samples, and only one blind mm line survey with detailed source characterization exists. It is unclear whether the preselection of targeted surveys will affect the results. It is also unknown if there is any type of galaxies overlooked by previous surveys, and the nature of mm line-selected galaxies is waiting to be explored. In this thesis, we present an analysis of five massive distant galaxies discovered by the detection of emission lines in ALMA spectral scan observations of the SSA22-AzTEC26 and VV114 fields. The goals are (1) presenting new mm line searches (2) investigating the physical properties of mm line emitters and discussing galaxies missed before.

We first experiment with line search algorithm using the ALMA Band 3 spectral scan observation of the SSA22-AzTEC26 field. In addition to the targeted submm galaxy SSA22-AzTEC26, we detect four new line emitters with signal-to-noise ratio  $> 5.2$  in the spectral cube smoothed with a  $300 \text{ km s}^{-1}$  FWHM Gaussian filter. Based on photometric redshifts from UV-to-FIR spectral energy distribution modeling, we reveal that two of them are CO(2-1) at redshifts of 1.113 and 1.146 and one is CO(3-2) at  $z = 2.124$ . The three sources are massive galaxies with a stellar mass  $\gtrsim 10^{10.5} M_{\odot}$ , but have different levels of star formation. Two lie within the scatter of the main sequence (MS) of star-forming galaxies at  $z \sim 1-2$ , and the most massive galaxy lies significantly below the MS. However, all three sources have a gas fraction within the scatter of the MS scaling relation, suggesting star formation suppression in the presence of a large gas reservoir.

For the other two line-emitting galaxies in the VV114 field with shallower ALMA data, we exploit the recently released JWST NIRCам/MIRI images. One of the two galaxies, J0107a, is a bright ( $\sim 8 \text{ mJy}$  at observed-frame  $888 \mu\text{m}$ ) and ultramassive (stellar mass  $\sim 4.5 \times 10^{11} M_{\odot}$ ) dusty star-forming galaxy at  $z = 2.467$ . The JWST NIRCам images of J0107a show a grand-design spiral with a prominent stellar bar extending  $\sim 15 \text{ kpc}$ . The ALMA Band 7 continuum map reveals that the dust emission originates from both the central starburst and the stellar bar. 3D disk modeling of the CO(4-3) emission line indicates a dynamically cold disk with rotation-to-dispersion ratio  $V_{\text{max}}/\sigma \sim 8$ . The other galaxy, J0107b at  $z = 2.310$  with a stellar mass of  $\sim 1.6 \times 10^{11} M_{\odot}$  shows spiral structure. Both galaxies are on the MS, but the gas depletion is faster in J0107a, suggesting the effect of the stellar bar. In addition, using photometric redshift, we identify CO(2-1) emission line from a  $z = 1.186$  spiral galaxy near J0107a, which is also on the MS.

The results show that untargeted mm/submm line surveys, which blindly select galaxies based on their molecular gas masses, mainly pick massive star-forming galaxies on the MS (4/5 of the sample). The consistency with various scaling relations means our knowledge of gas-regulated galaxy evolution in the distant universe based on optical/NIR galaxy catalogs and targeted CO line follow-up observations is mostly robust. However, the discovery of a possible gas-rich quiescent galaxy in the SSA22-AzTEC26 field suggests targeted line surveys may indeed miss certain types of galaxies which they are biased against. The analysis of J0107a/J0107b shows that a multiwavelength analysis including mm/submm emission line reveals plenty of information about the internal physical processes in star-forming galaxies at cosmic noon and possible nonmerger origin of some of the brightest submm galaxies. We conclude that new mm/submm emission line survey can be conducted using existing spectral scan data, and such studies significantly contribute to our understanding of gas-regulated galaxy evolution at high redshift.

# Contents

<b>1</b>	<b>Introduction to Galaxy Evolution</b>	<b>4</b>
1.1	Galaxy Formation and Evolution Across Cosmic Time . . . . .	4
1.2	Galaxy Evolution Probed by Millimeter/Submillimeter Emission Lines . . . . .	6
1.3	Scope of This Thesis . . . . .	8
<b>2</b>	<b>Blind Search of Emission Lines toward SSA22-AzTEC26</b>	<b>9</b>
2.1	Introduction of This Section . . . . .	9
2.2	Blind Line Search using ALMA Band 3 Spectral Scan Observation . . . . .	10
2.2.1	ALMA Data . . . . .	10
2.2.2	Source detection and line measurements . . . . .	11
2.3	A Multiwavelength Analysis of 3 mm Line Emitters . . . . .	13
2.3.1	Optical and NIR Data . . . . .	13
2.3.2	Infrared Data . . . . .	15
2.3.3	Spectral Energy Distribution Modeling . . . . .	18
2.4	Results . . . . .	18
2.4.1	Source Identification and Redshift Solutions . . . . .	18
2.4.2	Physical Properties of 3 mm Line Emitters . . . . .	20
2.4.3	Molecular Gas Mass . . . . .	23
2.5	Discussion: Comparison with Molecular Gas Scaling Relations and the Discovery of a Gas-rich Quiescent Galaxy Candidate . . . . .	28
2.5.1	Comparison with Molecular Gas Scaling Relations . . . . .	28
2.5.2	A Gas-rich Quiescent Galaxy Candidate at $z = 1.146$ . . . . .	30
2.5.3	Caveats of Galaxy 4's SFR Estimate . . . . .	34
2.6	Summary of Section 2 . . . . .	34
<b>3</b>	<b>Serendipitously Detected CO Line Sources in the VV114 Field</b>	<b>36</b>
3.1	Introduction of This Section . . . . .	36
3.2	Multiwavelength Dataset of the VV114 Field . . . . .	37
3.2.1	The Target: ALMA J010748.3-173028 (J0107a) . . . . .	37
3.2.2	ALMA Data . . . . .	37
3.2.3	JWST Data . . . . .	37
3.3	Analysis and Results . . . . .	39
3.3.1	JWST and ALMA Look at J0107a . . . . .	39
3.3.2	Photometry and Spectral Energy Distribution Modeling . . . . .	39
3.3.3	Properties of the Two Neighboring galaxies and Association with J0107a . . . . .	41
3.3.4	Dynamical Modeling . . . . .	42
3.4	Discussion and Conclusion: An Ultramassive Barred Spiral Galaxy at $z = 2.467$ and the Implications . . . . .	44
3.5	A Quick Glimpse of J0107b at $z = 2.310$ . . . . .	46
3.6	Follow-up Observations of J0107a in the VV114 Field . . . . .	47
3.6.1	VLA Semester 2023B Follow-up Observation . . . . .	47
3.6.2	Total Molecular Gas Mass and Excitation of J0107a/J0107b . . . . .	47
3.6.3	ALMA Cycle 10 Follow-up Observations . . . . .	50
<b>4</b>	<b>Concluding Remarks and Future Prospects</b>	<b>52</b>
<b>5</b>	<b>Bibliography</b>	<b>54</b>



# 1 Introduction to Galaxy Evolution

## 1.1 Galaxy Formation and Evolution Across Cosmic Time

Galaxies, including our Milky Way, are collections of dark matter, gas, dust, stars, and remnants of stars bounded by gravitational force. The typical size of a galaxy ranges from  $\sim 1$  kpc to  $\sim 100$  kpc, and the total mass spans from only  $\sim 10^7 M_\odot$  to  $\sim 10^{13} M_\odot$ . Based on their visual appearance, galaxies are classified into irregular, spiral/barred spiral, lenticular, and elliptical galaxies. Generally, in the local universe, the above morphology categories form a sequence gradually varying in physical properties, from the bluest colors, youngest stellar population, and highest levels of star formation in irregular galaxies, to the reddest colors, oldest stellar population, and the lowest levels of star formation in elliptical galaxies. Understanding the formation and evolution of the diverse galaxy population is one of the most important goals in modern astronomy.

The formation of galaxies in the framework of  $\Lambda$ CDM cosmology can be briefly summarized as follows (Mo et al. 2010). Shortly after the Big Bang, the overdense regions in the initial density field attract their surroundings and collapse to form dark matter halos inside which galaxies are born. These dark matter halos continue to accrete materials from the environment and grow with time. At the same time, the baryonic component (i.e., hydrogen and helium gas,  $\sim 1/5$  of the dark matter in mass) cools and settles into a protogalaxy at the center of the halo. Then, as the gas cooling processes proceed, catastrophic collapse and fragmentation under the gravity of the gas lead to star formation and produce a visible galaxy. If enough angular momentum of the inflowing gas is conserved, the resulting protogalaxy will spin up and form a rotating disk. The formation of the first galaxies is predicted to happen around  $z \sim 15$ – $20$  ( $\sim 200$  Myrs after the Big Bang, e.g., Springel et al. 2005; Bromm & Yoshida 2011).

The cosmic star formation rate density (CSFRD) gradually increases from early times to its peak at  $z \sim 2 - 3$ , an epoch called cosmic noon, and then decreases steadily to the present day (for a review, see Madau & Dickinson 2014). The cosmic evolution trends of molecular gas density (e.g., Decarli et al. 2020) and supermassive black hole (SMBH) activity (e.g., Aird et al. 2010) remarkably resemble that of CSFRD, the assembly history of galaxies. The former similarity is a natural consequence of molecular gas being the immediate fuel of star formation. The gas supply is controlled by the baryon accretion rate as a function of the cosmic epoch and the halo mass growth (Dekel & Birnboim 2006): below  $z \sim 2$  and above a certain halo mass  $M_{\text{halo}} \gtrsim 10^{12} M_\odot$ , persistent shock waves develop and heat up the cold gas, preventing it from arriving the central galaxy (Kereš et al. 2005). At higher redshifts, such massive halos are increasingly rarer and resident in the densest regions of the cosmic web, so that cold gas streams can manage to penetrate the

hot medium in the halo and feed the central galaxy (Dekel et al. 2009). On the other hand, the latter similarity impacts the CSFRD in an opposite way. As suggested by the observed stellar mass distribution of galaxies (stellar mass function, e.g., Caputi et al. 2011; Muzzin et al. 2013), a galaxy cannot keep its growth forever and the acquisition of fresh gas and star formation must be halted around a certain point. To reproduce the observed stellar mass function, active galactic nucleus (AGN, i.e., accreting SMBH) and supernovae feedback processes are commonly implemented in cosmological simulations (e.g., Weinberger et al. 2017; Davé et al. 2019). The energy injection from AGN and supernovae can remove the cold gas and suppress star formation (e.g., Hopkins et al. 2006; Hopkins & Elvis 2010). In addition, heating of the accreted gas by persistent shocks in massive halos (e.g., Kereš et al. 2005) and dynamical stabilization of gas disk against collapse by the steep gravitational potential of stellar bulge (morphological quenching, e.g., Martig et al. 2009) also contribute to star formation suppression. These processes make the galaxy 'red and dead', giving rise to the quiescent galaxy population.

Galaxy-galaxy mergers also shape the galaxy evolution. In standard  $\Lambda$ CDM cosmology, dark matter halos (and hence their central galaxies) grow with time by accreting the surrounding material, and by merging with other halos. The hierarchical growth via mergers plays an important role in galaxy evolution, especially for massive galaxies and in the early universe, where the merger rate was high (e.g., Conselice et al. 2003; Lotz et al. 2011; Mundy et al. 2017). While the exact impact of a merger depends on the orbit orientation and progenitor properties, it can drive cold gas into the center of the merging galaxy pair and destroy the galactic disks, providing an explanation for the triggering mechanisms of starburst and AGN activities in interacting systems and morphology transformation from star-forming disk to 'red and dead' elliptical galaxies. For example, Hopkins et al. (2008) show that AGN activities caused by gas-rich major merger dominate the  $z \gtrsim 1$  quasar luminosity density, and the growing SMBH deep inside the dusty starbursting core will blow out the gas and dust, resulting in an unobscured quasar; finally the quasar fades away and leaves a 'red and dead' spheroidal remnant. The comparison of observed clustering properties suggests this scenario can be the main formation channel of massive elliptical galaxies (Hickox et al. 2012).

Though significant progress has been made in both theoretical modeling and observational explorations, the picture of galaxy formation and evolution is still not complete. One of the most outstanding questions is what are the mechanisms that drive star formation and quenching in massive galaxies, or *what governs the birth, life, and death of galaxies*. The most massive galaxies (stellar mass  $M_\star \gtrsim 10^{11} M_\odot$ ) have built the bulk of their  $M_\star$  around or earlier than the cosmic noon and ceased star formation in late epochs (e.g., Thomas et al. 2010; Muzzin et al. 2013; Tomczak et al. 2014; McDermid et al. 2015; Davidzon et al. 2017), and characterizing the physical processes during their assembly phase requires expensive spectroscopic ob-

servations of high-redshift galaxies. So far such observations have been limited to some of the most extreme objects such as merger-induced starburst (e.g., [Engel et al. 2010](#)) and luminous quasars (e.g., [Zakamska et al. 2016](#)) due to the faintness of distant galaxies. Even with an eight-meter-class optical telescope, detecting such galaxies in emission line may require an exposure time of tens of hours, and the stellar continuum could be even not reachable in realistic observing time. The limited access to spectroscopic information and biased samples plague the comparison with theoretical predictions, and many of the proposed processes in galaxy evolution models have not been confirmed observationally. To push our understanding of galaxy evolution, a full census targeting objects of different types and multiple observational probes are needed.

## 1.2 Galaxy Evolution Probed by Millimeter/Submillimeter Emission Lines

Spectroscopic observations yield a wealth of information on the physical processes in galaxies such as stellar and gas motion, gas cooling (e.g.,  $\text{Ly}\alpha$  121.6 nm), star formation rate (SFR, e.g.,  $\text{H}\alpha$  656.5 nm,  $[\text{O II}]$  372.7 nm emission lines), stellar age (e.g., Balmer break and metal absorption lines), AGN activity (high ionization emission lines, e.g.,  $\text{C IV}$  154.9 nm and  $\text{N V}$  124.0 nm), outflow (e.g., blueshifted broad  $[\text{O III}]$  500.7 nm emission line), molecular gas mass (e.g., CO rotational transition and  $[\text{C I}]/[\text{C II}]$  emission lines), and atomic hydrogen mass and dynamics via the HI 21 cm emission line. These spectral features, if all observed, draw a full picture of galaxy life cycle including gas accretion, star formation, merger/interaction, AGN activity, feedback, and quenching.

Historically, most spectroscopic galaxy surveys have been conducted at optical and near-infrared (NIR) wavelengths due to the availability of observing facilities. Despite the success of such surveys in providing demographic information of galaxies in the local universe (e.g., [Bundy et al. 2015](#); [Liske et al. 2015](#)), reaching high-redshift remains challenging. For example, the VUDS survey ([Tasca et al. 2017](#)), a deep survey targeting galaxies at  $2 < z < 6$  using the 8.1m VLT UT3 telescope, uses 28 hours of exposure time per  $14' \times 16'$  pointing, and the total surveyed area of  $1 \text{ deg}^2$  is only  $2.4 \times 10^{-5}$  of the whole sky. What's worse, high-redshift massive star-forming galaxies are dusty, as more than 90% of star formation in a  $M_\star > 10^{11} M_\odot$  galaxy is obscured ([Whitaker et al. 2017](#)). For some very dusty galaxies, 1–2 hours of exposure using the VLT may result in non-detection ([Förster Schreiber et al. 2009](#)), and some of them are even invisible in deep NIR images (e.g., [Smail et al. 2021](#)). This means deep optical and NIR surveys may miss the most massive galaxies in the distant universe, which are nonetheless intrinsically luminous.

Emission lines in the millimeter (mm) and submillimeter (submm) regimes offer a new window to galaxy evolution at high redshift. These emission lines are free from dust extinction and hence the optimal probe of massive dusty star-forming galaxies. Furthermore, they carry unique information for deciphering astrophys-

ical processes. For example, the brightest emission lines at mm wavelength, CO rotational transition lines, are commonly used as a tracer of cold molecular gas because molecular hydrogen is a poor emitter and CO is the second abundant molecule in the interstellar medium (ISM). Thus, observations of CO lines can measure the molecular gas mass  $M_{\text{mol}}$  in galaxies and give an estimate of their lifetime (e.g., depletion timescale  $t_{\text{dep}} = M_{\text{mol}}/\text{SFR}$ ), which evolves across cosmic time and is distinct in galaxies with different star formation mechanisms. For studies of galaxy structure and dynamics, mm/submm emission lines can be a proxy of the cold/neutral phase of ISM (e.g., [Tadaki et al. 2017](#); [Rizzo et al. 2020](#)) and complement warm/ionized phase observed by optical/NIR spectroscopy. Simulations have shown the dynamics of [C II] 158  $\mu\text{m}$  line is less turbulent than that of  $\text{H}\alpha$  ([Kohandel et al. 2023](#)), highlighting the importance of including mm/submm lines in galaxy kinematic analysis. Lastly, the underlying continuum traces the dust mass and obscured SFR. The observations of mm/submm continuum benefit from the negative  $K$ -correction ([Casey et al. 2014](#)), which means the observed flux is roughly constant for a fixed infrared (IR) luminosity in redshift range  $z \sim 1\text{--}10$ . Thus, blank field mm/submm survey can be used to constrain the cosmic evolution of obscured star formation (e.g., [Zavala et al. 2021](#)).

Despite of less dust obscuration, spectroscopic survey in millimeter bands, mainly targeting CO lines, is more challenging than that at optical/NIR wavelengths. The sensitivity and spatial resolution required for the detection and counterpart identification of high-redshift CO lines necessitate interferometric observation with long integration times. Majority of the existing surveys draw their samples from optical/NIR galaxy redshift catalogs (e.g., [Tacconi et al. 2013](#); [Freundlich et al. 2019](#)), and often biased to high SFR galaxies to ensure detection. Consequently, the derived scaling relations between gas mass traced by CO lines and other galaxy properties may need extrapolation. The results from targeted studies should be complemented by blind CO surveys, which provide a gas mass-limited sample of galaxies by scanning the sky in a continuous frequency range. Such surveys can also directly constrain the cosmic molecular gas density evolution ([Decarli et al. 2019](#)) and give valuable insight into the galaxy assembly history. Unfortunately, blind spectral scans are time-consuming, even with the most advanced mm telescope, Atacama Large Millimeter/submillimeter Array (ALMA). The ASPECS-LP ([González-López et al. 2019](#)) program uses 150 hours of ALMA time to scan the sky frequency ranges of 84–115 GHz and 212–272 GHz with a 4.6  $\text{arcmin}^2$  half-sensitivity area, resulting in detection of 16 emission lines. To the best of the author’s knowledge, currently, this is the only blind mm line survey with a statistical sample size and thoroughly investigated source properties. The still small sample size and sky area make the conclusions vulnerable to cosmic variance. Furthermore, the question of whether there are certain types of galaxies, for example, gas-rich but low SFR galaxies overlooked by previous surveys, is waiting to be answered as ASPECS did not find noticeable extreme objects.

### 1.3 Scope of This Thesis

From the background, it is clear that blind mm line surveys play a unique role in studying galaxy evolution at high redshift, and new surveys are urged to push our further explorations. Meanwhile, the telescope time investment almost prohibits new ASPECS-like surveys in other fields considering the  $> 6\times$  oversubscription of ALMA time. An alternative approach to survey the sky at mm wavelength is to make use of data from existing targeted spectral scan observations and search for off-center emission line sources. This method is particularly promising when the target is extragalactic source so accompanying multiwavelength data are often deep enough for extracting counterpart properties. By mining the ALMA archive, it is possible to extend blind line surveys to much larger sky areas and to multiple sightlines, thus giving a better understanding of how targeted surveys may be biased and the overall characteristics of gas-mass selected galaxies. In addition, the discovery of galaxies unique to mm surveys will also benefit from the wider search area.

In this thesis, we demonstrate the use of targeted mm spectral scans to conduct new blind CO line surveys. We present a thorough analysis of six distant galaxies discovered by ALMA line scan observations in two distinct fields: SSA22-AzTEC26 in Section 2 and VV114 in Section 3. For one galaxies with barred spiral sturcture and high SFR, we describe our follow-up observations in Section 3.6.

Throughout this thesis, we adopt the [Chabrier \(2003\)](#) initial mass function and Planck 2018 cosmology ( $H_0 = 67.4 \text{ km s}^{-1} \text{ Mpc}^{-1}$ ,  $\Omega_m = 0.315$  and  $\Omega_\Lambda = 0.685$ ; [Planck Collaboration et al. 2020](#)).

## 2 Blind Search of Emission Lines toward SSA22-AzTEC26<sup>1</sup>

### 2.1 Introduction of This Section

The cosmic star formation rate (SFR) density increases from early times to its peak at  $z \sim 2$ , called cosmic noon, then decreases progressively to the present day (for a review, see [Madau & Dickinson 2014](#)). Across cosmic history, the most massive galaxies (stellar mass  $M_\star \gtrsim 10^{11} M_\odot$ ) have formed the bulk of their  $M_\star$  around or earlier than the cosmic noon and ceased star formation in late epochs (e.g., [Thomas et al. 2010](#); [Muzzin et al. 2013](#); [Tomczak et al. 2014](#); [McDermid et al. 2015](#); [Davidzon et al. 2017](#)), while the formation of less massive galaxies continues for a longer period. Molecular gas is a key factor in shaping the history of galaxy assembly, as it is the immediate material of star formation (for a review, see [Carilli & Walter 2013](#)). It has been suggested that galaxies acquire molecular gas via accretion from the intergalactic medium (e.g., [Dekel et al. 2009](#); [Narayanan et al. 2015](#)) or mergers to fuel their star formation and central black hole growth (e.g., [Hopkins et al. 2008](#)). Observations of molecular gas content in local and distant galaxies thus provide important clues about galaxy formation and evolution.

CO rotational transition lines are commonly used to trace the molecular gas content of galaxies because molecular hydrogen is a poor emitter and CO is the second most abundant molecule in the interstellar medium (ISM). Numerous observations of CO line emission have been conducted to obtain statistical samples of galaxies at intermediate and high redshifts ( $z \sim 1 - 3$ ) to study the relation between gas and other properties of galaxies, such as  $M_\star$  and SFR. CO observations of high-redshift galaxies typically select massive normal star-forming galaxies (SFGs; e.g., [Daddi et al. 2010a](#); [Tacconi et al. 2010](#)) or the most extreme starbursting galaxies (e.g., [Neri et al. 2003](#); [Engel et al. 2010](#); [Bothwell et al. 2013](#)). These surveys have successfully established scaling relations that describe how galaxy properties evolve with the gas mass (e.g., [Genzel et al. 2015](#); [Tacconi et al. 2018, 2020](#)).

Observations of a large sample of galaxies have revealed a tight correlation between  $M_\star$  and SFR called the main sequence (MS; e.g., [Elbaz et al. 2007](#); [Daddi et al. 2010a](#); [Wuyts et al. 2011](#); [Whitaker et al. 2012](#); [Speagle et al. 2014](#); [Schreiber et al. 2015](#)). SFGs on the MS dominate the cosmic star formation ([Rodighiero et al. 2011](#); [Sargent et al. 2012](#)), implying the existence of mechanisms that regulate star formation from gas and the steady buildup of galaxies (e.g., [Lilly et al. 2013](#)). Below the scatter of the MS, there is another population of passive or quiescent galaxies (QGs), with little or no ongoing star formation (e.g., [Strateva et al. 2001](#); [Kauffmann et al. 2003](#); [Baldry et al. 2004](#); [Chang et al. 2015](#)). Many physical processes have

---

<sup>1</sup>The contents of this section are published in the *Astrophysical Journal*: <https://iopscience.iop.org/article/10.3847/1538-4357/ace0c0>

been proposed to explain the shutdown of star formation, including the starvation of gas, either due to the removal of cold gas by stellar and supermassive black hole feedback (e.g., [Hopkins et al. 2006](#); [Hopkins & Elvis 2010](#)) or rapid gas consumption by vigorous star formation (e.g., [Gao & Solomon 1999](#); [Man et al. 2019](#)), and the inability of the conversion of gas into stars due to changes in the ISM condition ([French et al. 2018](#)) or stabilization against collapse and fragmentation (e.g., [Martig et al. 2009](#)). In order to understand the roles of these processes in galaxy quenching, it is essential to characterize the gas properties such as the gas fraction, depletion timescale, and kinematics.

In the case of massive galaxies, this requires detecting CO emission at  $z \gtrsim 1$ , which corresponds to the epoch when many of them are undergoing formation and subsequent quenching. Most of the aforementioned high-redshift CO observations target preselected MS galaxies or starbursts, thus current scaling relations (e.g., [Tacconi et al. 2018](#)) only account for SFGs. Whether these relations are still valid when extrapolated to passive galaxies remains unknown. Recent targeted observations of CO emission from QGs have shown a mixed picture (e.g., [Belli et al. 2021](#); [Williams et al. 2021](#)). An unbiased CO survey of galaxies in various stages of star formation is needed to investigate the evolution of gas content before and after galaxy quenching. By detecting both low and medium to high  $J$  transitions, it is also possible to study the redshift evolution of the molecular gas in galaxies. Several studies have used the Atacama Large Millimeter/submillimeter Array and JVLA to perform blind line searches toward deep cosmological fields or ALMA calibrators ([Walter et al. 2016](#); [González-López et al. 2019](#); [Riechers et al. 2019, 2020](#); [Hamanowicz et al. 2023](#)). However, because of the large amounts of telescope time needed, the surveyed area and the number of detected sources are still very limited.

In this section, we present serendipitous detections and physical properties of four CO emitters in the vicinity of the bright submillimeter galaxy (SMG) SSA22-AzTEC26 from ALMA band 3 observations. In Section 2.2 and 2.3 we describe the ALMA observation and data analysis. In Section 2.4 we present the extracted galaxy properties utilizing multiwavelength data in the SSA22 field. In Section 2.5, we discuss the gas content of CO-selected galaxies in the context of galaxy evolution, and then we summarize in Section 2.6.

## 2.2 Blind Line Search using ALMA Band 3 Spectral Scan Observation

### 2.2.1 ALMA Data

SSA22-AzTEC26 is a bright SMG first discovered by the AzTEC/ASTE 1.1 mm extragalactic survey in the SSA22 field ([Tamura et al. 2009](#); [Umehata et al. 2014](#)). The ALMA band 3 spectral scan observations

(Project ID: 2019.1.01102.S; PI: Umehata) were conducted from 2020 March 20 to 2020 April 3, toward the sky position of SSA22-AzTEC26 (R.A. 22:17:13.34, decl. 00:26:51.66). The observations had a maximum baseline of 313.7 m and continuously covered the sky frequency range from 84.5 to 113.7 GHz with five tunings. The total integration time was 6.2 hr. J2217+0220 and J2206-0031 were observed for phase calibration. To calibrate the flux and bandpass, J0006-0623, J2253+1608, J2258-2758, and J1924-2914 were observed.

We use the CASA package (CASA Team et al. 2022) to reduce the data and perform imaging. A spectral cube is created using the `tclean` task with natural weighting and a  $100 \text{ km s}^{-1}$  channel width. The resulting band 3 spectral cube has a  $\sim 1'.5$  arcmin diameter field of view (FOV) with a minimum primary beam (PB) response of 20% of the field center. The synthesized beam size is  $3''.80 \times 2''.45$  with a position angle (PA) of  $57^\circ.7$  to  $4''.38 \times 3''.65$  with PA of  $81^\circ.2$  degrees, depending on the sky frequencies. The RMS noise level range is  $0.06 - 0.18 \text{ mJy beam}^{-1}$  before PB correction.

We also include band 4 and band 7 data (Project ID: 2021.1.01207.S; PI: Umehata) in our analysis. The band 4 observations cover the frequency ranges of 143.0-146.7 GHz and 154.9-158.7 GHz with a single tuning and total integration time of 2.5 hr. We process the data in a similar manner as for band 3. The resulting band 4 cube has a synthesized beam size of  $0''.87 \times 0''.79$  to  $0''.96 \times 0''.88$  with PA of  $\sim 61$  degrees, and RMS noise level of  $0.05 - 0.09 \text{ mJy beam}^{-1}$  in a  $\sim 40''$  FOV. The band 7 data cover the frequency range 340.4-356.2 GHz with the beam size of  $0''.63 \times 0''.52$  with a PA of  $88^\circ.8$  and an RMS noise of  $0.09 \text{ mJy beam}^{-1}$  in the  $860 \mu\text{m}$  continuum map.

### 2.2.2 Source detection and line measurements

Inspired by Walter et al. (2016), we smooth the band 3 cube with a  $300 \text{ km s}^{-1}$  FWHM Gaussian filter and use the `DAOSTarFinder` routine in the `photutils` (Bradley et al. 2022) package to detect all positive and negative peaks above a peak signal-to-noise ratio (S/N) of 1.5 in the smoothed cube. The central AzTEC source is masked because its continuum emission is visible in the smoothed cube and contaminates source statistics. We show the number of detected peaks as a function of peak S/N in the left panel of Figure 1. No negative peak is found above  $S/N = 5.2$ . The purity of detection as a function of S/N is defined as

$$\text{Purity} = 1 - \frac{N_{\text{negative}}}{N_{\text{positive}}}. \quad (1)$$

We fit the measured purity as a function of S/N with

$$P(S/N) = \frac{1}{2} \text{erf} \left( \frac{S/N - a}{b} \right) + 0.5, \quad (2)$$

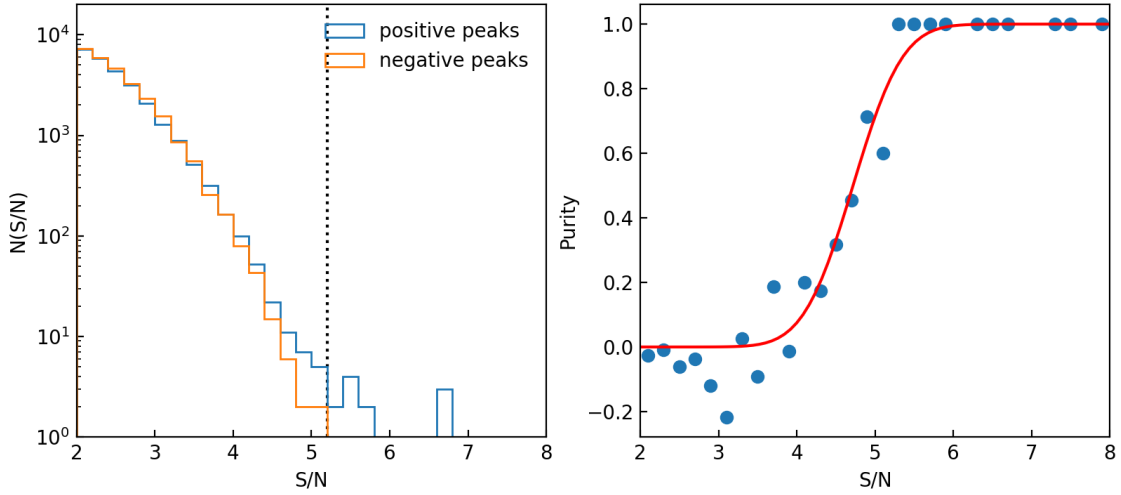


Table 1. Results of Blind Line Emitter Search in the Band 3 Cube and Source Measurements.

ID	R.A.	Decl.	$\nu_{\text{obs}}$ (GHz)	S/N	FWHM (km s <sup>-1</sup> )	$S\Delta v$ (Jy km s <sup>-1</sup> )	$S_{3\text{mm}}$ ( $\mu\text{Jy}$ )	$S_{2\text{mm}}$ ( $\mu\text{Jy}$ )	$S_{860\mu\text{m}}$ (mJy)
1	22:17:12.36	00:26:43.59	110.698	5.9	697 $\pm$ 153	0.569 $\pm$ 0.075	14.8 $\pm$ 2.4	90 $\pm$ 18	-
2	22:17:13.00	00:26:54.06	109.151	7.8	635 $\pm$ 137	0.358 $\pm$ 0.036	< 13	39 $\pm$ 7.3	0.815 $\pm$ 0.194
3	22:17:15.01	00:27:13.32	91.785	7.3	252 $\pm$ 85	0.450 $\pm$ 0.075	21.7 $\pm$ 3.1	-	-
4	22:17:11.93	00:27:14.82	107.414	5.5	630 $\pm$ 123	0.713 $\pm$ 0.141	< 27	< 100	-

Note. The 3mm fluxes and the 2 mm flux of source 1 are measured using line-free spectral windows. For non-detection, we report  $3\sigma$  upper limit. Source 1 has another line detection at 157.548 GHz, with  $S\Delta v = 0.320 \pm 0.044$  Jy km s<sup>-1</sup> and FWHM of 683  $\pm$  201 km s<sup>-1</sup>.

and determine the free parameters  $a = 4.72$  and  $b = 0.71$ , which gives a purity of 83% at S/N=5.2. Using this as a detection threshold, we find four sources with S/N > 5.2 (Figure 2). We have also tested other filter FWHM values from 100 to 500 km s<sup>-1</sup> with 100 km s<sup>-1</sup> steps but do not find any new detection.



**Figure 1.** Left: the number of detections as a function of positive or negative peak S/N. The S/N > 5.2 detection threshold is marked as a vertical dotted line. Right: purity as a function of peak S/N. The best-fit relation of Equation 2 is shown as a red curve.

For each source, we fit a single Gaussian profile to the 1D spectrum to derive the observed line frequency and FWHM (the bottom row in Figure 3). The velocity-integrated fluxes are measured by fitting a 2D Gaussian profile to the zeroth-moment map, which sums along the spectral axis over a velocity range  $\pm\text{FWHM}$  from the line center. The measured properties are listed in Table 1. Sources 1, 2, and 4 are covered by the band 4 observation, so we also report the 2 mm continuum flux densities for these three sources. Source 1

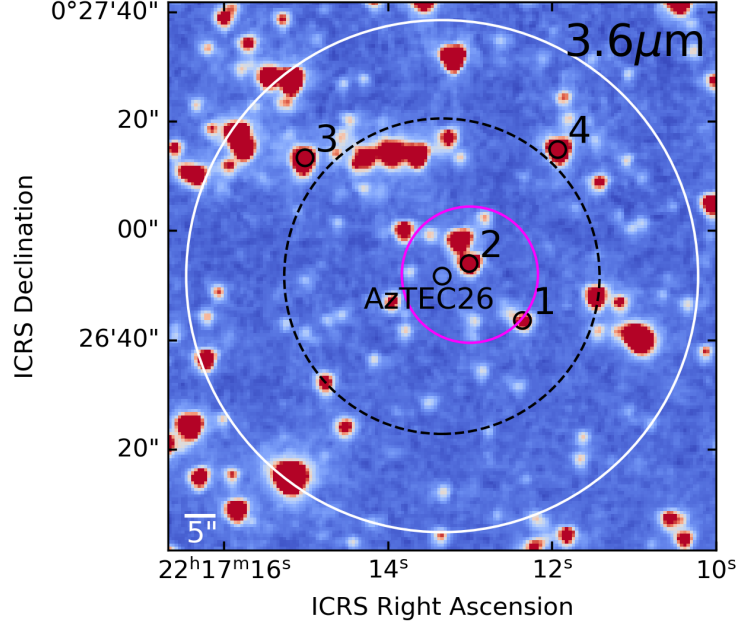


**Figure 2.** IRAC  $3.6\ \mu\text{m}$  image of the targeted field. The sky locations of SSA22-AzTEC26 and the four line emitters are marked with black empty circles. The ALMA FOVs with 20% PB response in bands 3, 4, and 7 are shown as the white, black dashed, and magenta circles, respectively.

has a second line detection at 157.548 GHz in the band 4 cube, and we will show that this is the redshifted [C I] line in the next section.

## 2.3 A Multiwavelength Analysis of 3 mm Line Emitters

### 2.3.1 Optical and NIR Data

The SSA22 field has rich multiwavelength data coverage. We collect ground-based optical-to-NIR images from the  $u$  to  $K$  bands from archives and literature. The thumbnails of the sources are shown in the top row of Figure 3. The astrometry is corrected by stacking cutout images at the positions of 1.1 mm continuum sources detected by ALMA in the SSA22 field (B. Hatsukade, private communication) and fitting a 2D circular Gaussian profile to the stacked image to determine the average positional offset between the ALMA source and its counterpart in each band. Sources 1, 2, and 4 have a coincident  $K$ -band counterpart with a centroid offsets of  $0''.27$ ,  $0''.23$ , and  $0''.14$ , respectively, comparable with a position uncertainty of  $\sim 0.2''$  of the line detection. The NIR counterpart of source 3 lies  $0''.62$  southeast of the CO position,  $\sim$ three times of the uncertainty of the line position.

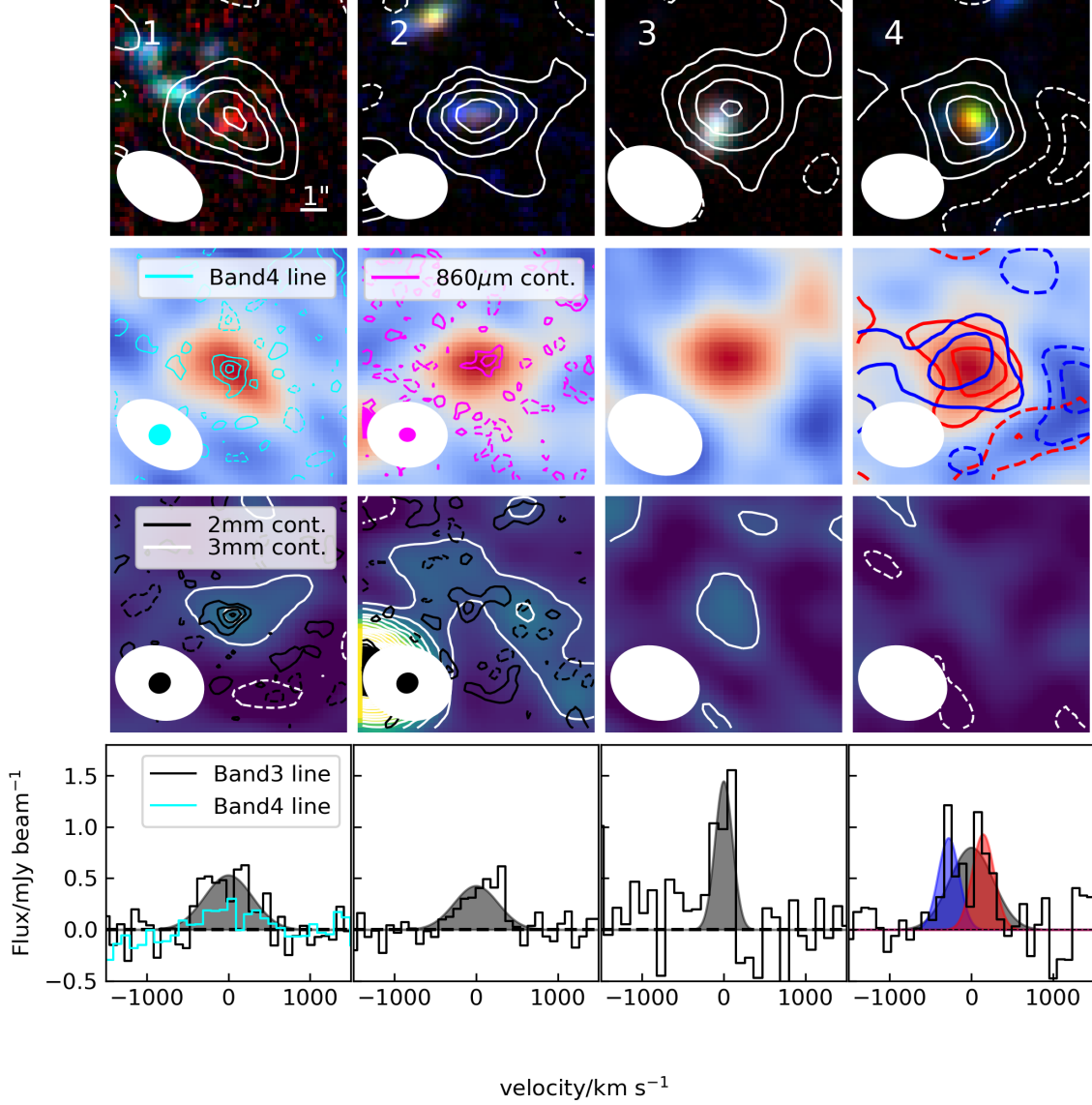


**Figure 3.** Top row: color-composite (red:  $K$ ; green:  $z'$ ; blue:  $B$ ) cutout images of the line emitters. Each image is  $10'' \times 10''$  in size. The zeroth-moment maps of the band 3 emission line are overlaid as white contours. The corresponding beam sizes are shown with white ellipses. Second row: the zeroth-moment maps of the band 3 emission line. The zeroth-moment map of the band 4 157.548 GHz emission line of source 1 is shown with cyan contours. For source 2 we show the band 7 continuum image with magenta contours. All contours start from  $\pm 1.5\sigma$  with a step of  $1.5\sigma$ , and the corresponding beam sizes are shown with the same colors. Third row: band 3 continuum images are shown with background and white contours. The band 4 images of sources 1 and 2 are overlaid as black contours. Bottom row: 1D band 3 spectra at the position of each source. The best-fit single Gaussian model is shown with a black shaded region. For source 1, the band 4 emission line is shown in cyan. For source 4, we fit two Gaussian components and show the corresponding zeroth-moment contour in the second row with the same color.

We measure the flux densities using a  $2''$  diameter circular aperture placed at the CO position in bands shorter than IRAC. The errors are estimated by taking the standard deviations of fluxes from 1000 randomly placed apertures at blank positions. Then we aperture correct the fluxes using the point spread function (PSF) and correct for galactic extinction using the [Schlegel et al. \(1998\)](#) dust map and [Cardelli et al. \(1989\)](#) Milky way extinction curve. PSFs are generated using the `PSFEX` ([Bertin 2011](#)) and `SExtractor` ([Bertin & Arnouts 1996](#)) codes from unsaturated point sources with  $S/N \geq 20$ .

As shown in Figure 3, the aperture flux of source 4 is contaminated by two blue neighboring sources. At this moment, we simply assume the two blue sources are foreground galaxies and subtract their contributions using 2D image modeling. We use a single Sérsic profile convolved with the PSF to model each galaxy and then perform Bayesian inference using the `dynesty` code ([Speagle 2020](#)) to derive posterior probability density functions (PDFs) of the model parameters. Flat priors of  $[0, 6]$  and  $[0.1, 5a_{\text{image}}]$  pixels are adopted for the Sérsic index  $n$  and half-light radius  $R_e$ , respectively, where  $a_{\text{image}} \sim 2$  pixels is the semi-major axis sigma value given by `photutils` and the pixel size is  $0''.2$ . We first model the central source using the  $K$ -band image and then the two neighboring galaxies jointly using the  $B$ -band image to minimize the effect of blending. In subsequent subtraction processes, the Sérsic shape parameters are limited to the 16th to 84th percentile range from the previous procedure and the central position can vary by  $\pm 0.5$  pixels from the median. The source flux is always allowed to vary freely. Then we simultaneously fit all three sources in each band from  $u$  to  $K$ . When measuring the flux of neighboring sources, we subtract the central source, and for the central source, we subtract the two neighboring clumps. Deblended fluxes and errors are derived from the posterior PDF in each band, with formal photometric errors added in quadrature. Examples of subtracting processes are demonstrated in Figure 4. Further discussion of the relation between the central and neighboring blue sources is given in section 2.5.2.

### 2.3.2 Infrared Data

For long-wavelength NIR ( $3.6 \mu\text{m}$ ) to MIR, we obtain IRAC  $3.6\text{--}8 \mu\text{m}$  and MIPS  $24 \mu\text{m}$  images from the Spitzer archive. At FIR wavelengths, we use Herschel SPIRE  $250\text{--}500 \mu\text{m}$  images from the ESA Herschel archive. Flux densities are derived from PSF photometry to overcome source blending issues. For the IRAC data, we apply the method introduced by [Hsieh et al. \(2012\)](#) which iteratively decomposes the image into a combination of ideal point sources and background noise. We consider decomposed point sources within  $1''$  ( $1.5$  pixels of IRAC images) from the CO position as associated with the target and use the sum of their amplitudes as the total flux. Errors are estimated from the RMS of the residual image.

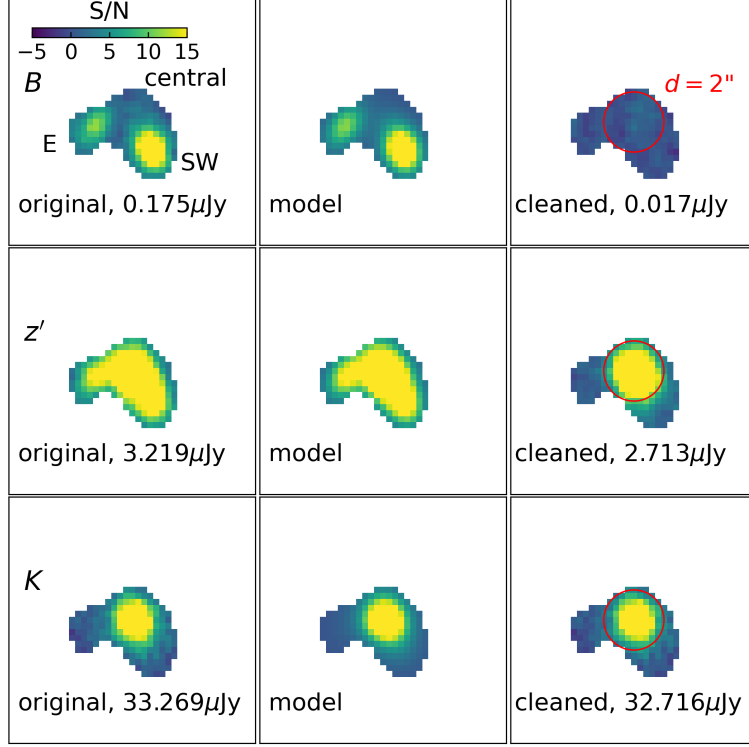
In the Spitzer/MIPS and Herschel/SPIRE bands, we measure the flux densities by directly fitting PSF

Table 2. Multiwavelength Photometry of the Four CO Emitters in Units of  $\mu\text{Jy}$ , Extracted at the CO Position.

Band	Instrument	1	2	3	4	Reference
<i>u</i>	CFHT/MegaCam	...	$0.125 \pm 0.020$	$1.183 \pm 0.019$	$0.078 \pm 0.020$	1
<i>B</i>	Subaru/SuprimeCam	$0.057 \pm 0.006$	$0.113 \pm 0.007$	$1.388 \pm 0.007$	$0.018 \pm 0.009$	2
<i>V</i>	-	$0.109 \pm 0.009$	$0.199 \pm 0.010$	$2.303 \pm 0.009$	$0.106 \pm 0.010$	2
<i>R</i>	-	$0.142 \pm 0.014$	$0.371 \pm 0.013$	$3.316 \pm 0.013$	$0.346 \pm 0.018$	3
<i>i'</i>	-	$0.186 \pm 0.018$	$0.748 \pm 0.018$	$5.853 \pm 0.020$	$0.911 \pm 0.024$	2
<i>z'</i>	-	$0.311 \pm 0.034$	$1.609 \pm 0.036$	$8.122 \pm 0.038$	$2.772 \pm 0.042$	2
NB359	-	$0.067 \pm 0.019$	$0.058 \pm 0.020$	$1.223 \pm 0.019$	$0.131 \pm 0.020$	4
NB497	-	$0.099 \pm 0.014$	$0.124 \pm 0.015$	$1.874 \pm 0.015$	$0.082 \pm 0.017$	5
NB816	-	$0.249 \pm 0.036$	$1.023 \pm 0.037$	$6.455 \pm 0.036$	$1.336 \pm 0.044$	2
NB912	-	$0.265 \pm 0.029$	$1.462 \pm 0.030$	$7.906 \pm 0.029$	$3.064 \pm 0.038$	2
<i>g</i>	Subaru/HSC	$0.083 \pm 0.017$	$0.133 \pm 0.016$	$1.828 \pm 0.017$	$0.089 \pm 0.020$	6
<i>r</i>	-	$0.115 \pm 0.031$	$0.280 \pm 0.033$	$3.077 \pm 0.034$	$0.321 \pm 0.043$	6
<i>i</i>	-	$0.177 \pm 0.027$	$0.793 \pm 0.030$	$6.245 \pm 0.030$	$0.990 \pm 0.038$	6
<i>z</i>	-	$0.284 \pm 0.079$	$1.668 \pm 0.076$	$7.797 \pm 0.077$	$2.828 \pm 0.098$	6
<i>Y</i>	-	...	$2.123 \pm 0.126$	$8.042 \pm 0.123$	$4.289 \pm 0.146$	6
<i>J</i>	UKIRT/WFCAM	$1.019 \pm 0.206$	$4.137 \pm 0.214$	$13.052 \pm 0.214$	$8.458 \pm 0.241$	7
<i>K</i>	-	$4.071 \pm 0.322$	$13.838 \pm 0.310$	$25.458 \pm 0.340$	$32.887 \pm 0.388$	7
IRAC1	Spitzer/IRAC	$11.565 \pm 0.220$	$25.925 \pm 0.192$	$44.430 \pm 0.704$	$67.229 \pm 0.556$	8,9
IRAC2	-	$18.926 \pm 0.851$	$25.833 \pm 1.121$	$44.152 \pm 0.815$	$59.478 \pm 2.734$	8,9
IRAC3	-	$17.952 \pm 2.103$	$17.459 \pm 1.747$	$40.255 \pm 1.980$	$37.444 \pm 2.027$	8,9
IRAC4	-	$15.686 \pm 2.269$	$18.327 \pm 2.857$	$28.632 \pm 2.483$	$32.981 \pm 3.147$	8,9
MIPS1	Spitzer/MIPS	$305 \pm 149$	$20 \pm 44$	$392 \pm 169$	$115 \pm 189$	8,9
PSW	Herschel/SPIRE	$6133 \pm 4584$	$4931 \pm 4861$	$4997 \pm 5191$	$3432 \pm 4442$	10,11
PMW	-	$6437 \pm 7227$	$11129 \pm 6856$	$5741 \pm 6574$	$2406 \pm 4033$	10,11
PLW	-	$1941 \pm 3710$	$4385 \pm 5905$	$2523 \pm 4818$	$1284 \pm 2745$	10,11

References. 1: K. Mawatari, private communication; 2: Nakamura et al. (2011); 3: Hayashino et al. (2004); 4: Iwata et al. (2009); 5: Yamada et al. (2012); 6: Aihara et al. (2018) 7: Lawrence et al. (2007); 8: Webb et al. (2009); 9: IRSA (2022) 10: Kato et al. (2016); 11: [http://herschel.esac.esa.int/Science\\_Archive.shtml](http://herschel.esac.esa.int/Science_Archive.shtml)

Note. “-” means the same as the previous band.



**Figure 4.** Examples of the neighbor subtraction of galaxy 4. The left, middle, and right columns show original data, the best-fit Sersic model, and the neighbor-subtracted data, respectively. The 2'' diameter aperture used to measure the flux is shown as a red circle. The relationship between the three components will be further discussed in section 2.5.2.

models to the image with IRAC 4.5  $\mu$ m and 1.1 mm source positions as priors, following the method of Hurley et al. (2017). Since our sources lie on the edge of the MIPS coverage, we also add sources detected at  $S/N > 5$  in IRAC 8  $\mu$ m images when deblending the SPIRE images to add dusty sources that are not covered by MIPS but might appear in SPIRE images. Starting from MIPS, we create a  $2' \times 2'$  cutout image centered at the line position. For each position  $(x_i, y_i)$  in all prior sources, the source model  $S_i(x, y)$  is made by interpolating the PSF centered at  $(x_i, y_i)$  to the pixel grid  $(x, y)$  and scaling it to unity flux density. The  $\chi^2$  can be expressed as

$$\chi^2 = \sum_{x,y} \left( \frac{I(x,y) - \sum_i f_i S_i(x,y)}{\sigma(x,y)} \right)^2, \quad (3)$$

where  $I(x, y)$  is the data and  $\sigma(x, y)$  is the flux uncertainty at each pixel. Then we perform Bayesian inference to derive the posterior PDF of the source flux densities  $f_i$ . Only sources that have a deblended  $S/N > 1$  will be used to fit the next band. None of the sources is detected at  $S/N > 3$  in any of the MIR/FIR images. The

measured fluxes are listed in Table 2.

### 2.3.3 Spectral Energy Distribution Modeling

We adopt the methodology of `prospector` (Leja et al. 2019b) to model the observed spectral energy distribution (SED), which fits all physical parameters simultaneously and yields the joint PDF as a result. We model the dust attenuation for old and young stars with two Noll et al. (2009) dust attenuation curves, which are the Calzetti et al. (2000) dust extinction curve multiplied by a power-law modification  $(\lambda_{\text{rest}}/550\text{nm})^\beta$ . For the two stellar populations separated by age, the slope  $\beta$  and amplitude of each curve can vary independently within a flat prior  $[-0.7, 0.4]$  for  $\beta$  and  $[0, 10]$  for  $E(B - V)$ , while the dust attenuation of old stars is forced to be smaller than that of young stars. This adds some additional flexibility in taking possible complex dust geometry into account. To implement the modification, SED models are built with the `CIGALE` code (Boquien et al. 2019). Before line identification, we let the redshift vary freely within a flat prior  $[0, 8]$  (i.e., the photometric redshift mode of SED fitting).

## 2.4 Results

### 2.4.1 Source Identification and Redshift Solutions

Each of the sources has only one robust line detection in the band 3 cube. The most probable identification of the detected line will be one of CO  $J_{\text{up}} = 4, 3, 2, 1$  from galaxies at  $z \lesssim 3 - 4$  because our  $\sim 29$  GHz bandwidth will cover two CO lines or one CO and [CI]( $^3\text{P}_1 - ^3\text{P}_0$ ) (hereafter, [CI](1-0)) atomic carbon emission line for  $z \gtrsim 3 - 4$ . To find the redshift solution, we plot the marginalized PDF of the photometric redshift from our SED fitting and `EAZY`<sup>2</sup> code (Brammer et al. 2008), together with the observed frequency as a function of redshift for the CO lines and [CI](1-0) line in Figure 5.

Based on the results of SED fitting, we find that all four sources are distant galaxies at a cosmological distance. For galaxies 1, 2, and 4, there is a unique solution for CO line redshift that is allowed by the photometric redshift PDF. The redshift of 2.124 given by the CO J=3-2 line of galaxy 1 agrees with the second line in band 4 being redshifted [CI](1-0), which yields a consistent redshift  $z_{[\text{CI}](1-0)} = 2.124$ . The photometric redshift PDF of galaxy 3 is incompatible with all solutions. Since the flux is extracted at the CO position, we check the results by changing the position of the photometry aperture to the center of the nearby NIR object, then the photometric redshift of  $0.63^{+0.07}_{-0.06}$  still does not overlap with any solution. Thus, the flux is likely to be dominated by an NIR source that is not associated with the CO emission. Given

<sup>2</sup><https://github.com/gbrammer/eazy-py>

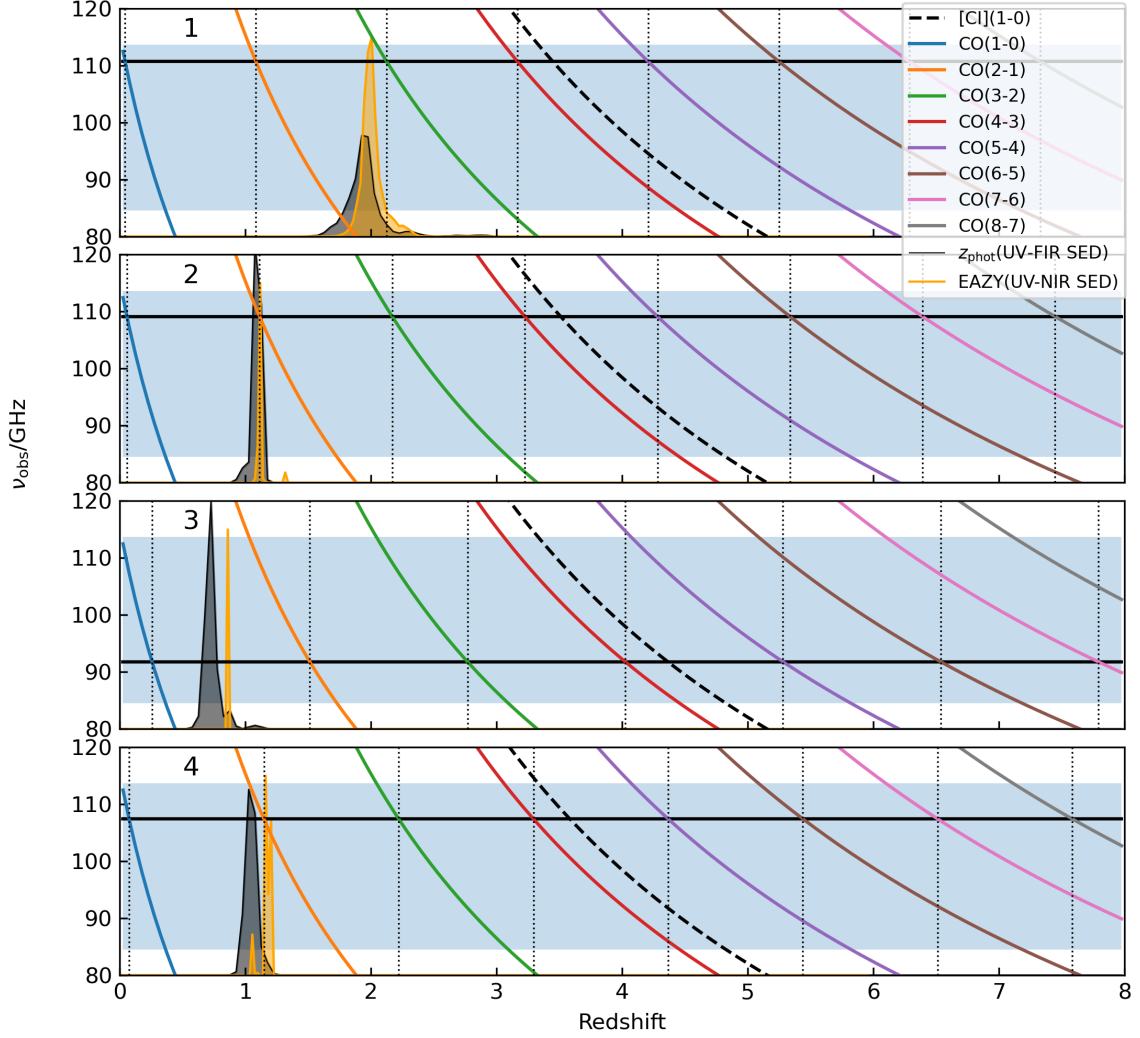


**Figure 5.** Observed frequency as a function of redshift for different spectral lines. CO lines are shown with colored curves and the [CI] line is shown with the dashed black curves. The blue shaded regions show the frequency coverage of the ALMA band 3 observations. We mark the observed frequency of each galaxy with a horizontal black line and the corresponding redshift of each solution with a vertical dotted line. The PDFs of photometric redshift are illustrated by lines and shaded regions, with black color for the SED fitting method described in Section 2.3.3 and orange color for EASY. A successful solution requires the vertical line to locate within the photometric redshift PDF.



Table 3. Results of Line Identification.

ID	CO transition ( $J_{\text{up}} - J_{\text{low}}$ )	$z_{\text{CO}}$	$L'_{\text{CO}(J_{\text{up}}-J_{\text{low}})}$ ( $10^{10} \text{ K km s}^{-1} \text{ pc}^2$ )	$M_{\text{mol}}^1$ ( $10^{10} M_{\odot}$ )
1	3-2	2.124	$1.45 \pm 0.19$	$12.5 \pm 1.6$
2	2-1	1.113	$0.62 \pm 0.06$	$2.9 \pm 0.3$
4	2-1	1.146	$1.31 \pm 0.26$	$6.2 \pm 1.2$

<sup>1</sup>CO-based molecular gas mass (Section 2.4.3). Alternatively, galaxy 1 has  $M_{\text{mol}} = (9.4 \pm 1.3) \times 10^{10} M_{\odot}$  based on its [CII](1-0) line luminosity  $L'_{[\text{CII}](1-0)} = (4.04 \pm 0.55) \times 10^9 \text{ K km s}^{-1} \text{ pc}^2$ .

only one line detection within the  $\sim 29 \text{ GHz}$  bandwidth, possible solutions will be  $z_{\text{CO}(2-1)} = 1.512$  or  $z_{\text{CO}(3-2)} = 2.767$ , but these need to be verified by detecting other spectral lines in future observations (e.g., Tamura et al. 2014; Mizukoshi et al. 2021).

The line luminosity is calculated from the velocity-integrated line flux  $S\Delta v$ , following Solomon & Vanden Bout (2005):

$$\frac{L'}{\text{K km s}^{-1} \text{ pc}^2} = \frac{3.25 \times 10^7 S\Delta v}{\text{Jy km s}^{-1}} \frac{D_L^2}{(1+z)^3 \nu_{\text{obs}}^2} \left[ \frac{\text{GHz}}{\text{Mpc}} \right]^2, \quad (4)$$

where  $D_L$  is the luminosity distance in megaparsecs corresponding to redshift  $z$ , and  $\nu_{\text{obs}}$  is the observed frequency of the line in gigahertz. We list the results of the line identification in Table 3. With the spectroscopic redshift determined from the CO line, we fix the redshift and refit the photometry for galaxies 1, 2, and 4, including band 3, 4, and 7 continuum measurements. In the following sections, we will focus on the derived physical properties of these three galaxies.

#### 2.4.2 Physical Properties of 3 mm Line Emitters

We show the SED fit and joint posterior distributions of the derived parameters in Figures 7–9 and 10–12, respectively. The results from SED fitting are summarized in Table 4. All reported values and errors represent median values and 68% confidence intervals, respectively, from marginalized posterior PDFs.

In Figure 6 we plot the three galaxies in the SFR- $M_{\star}$  plane, together with the MS relations at  $z = 1.1$ ,  $z = 2.1$  and  $z = 2.5$  from Speagle et al. (2014). For comparison, we also show the two galaxies (J0107a/J0107b) from shallower ALMA spectral scan data in Section 3 and the CO-selected galaxy sample from ASPECS-LP (Boogaard et al. 2019) that surveyed a larger area at a similar depth. The ASPECS-LP  $M_{\star}$  and SFR are derived using the MAGPHYS code (da Cunha et al. 2015). Different star formation history (SFH) and dust attenuation models can lead to a  $\sim 0.3$  dex systematic offset in the SED-derived  $M_{\star}$  and SFR (Buat et al.

Table 4. Derived Physical Properties from SED Fitting.

ID	$M_*$ ( $10^{10} M_\odot$ )	SFR ( $M_\odot \text{ yr}^{-1}$ )	$M_{\text{dust}}$ ( $10^8 M_\odot$ )	$L_{\text{dust}}$ ( $10^{11} L_\odot$ )	$A_V$ (mag)
1	$9.73^{+2.22}_{-2.47}$	$126^{+37}_{-54}$	$3.13^{+0.61}_{-0.54}$	$12.79^{+2.90}_{-4.00}$	$2.39^{+0.16}_{-0.25}$
2	$4.60^{+1.39}_{-1.00}$	$22^{+12}_{-8}$	$2.35^{+0.54}_{-0.52}$	$2.97^{+1.36}_{-0.69}$	$2.15^{+0.29}_{-0.30}$
4	$21.98^{+3.92}_{-3.88}$	$0.7^{+0.8}_{-0.6}$	$0.27^{+0.92}_{-0.01}$	$1.27^{+0.29}_{-0.27}$	$1.28^{+0.18}_{-0.20}$
4.E	$0.03^{+0.02}_{-0.01}$	$9^{+1}_{-1}$	$0.13^{+0.16}_{-0.05}$	$0.64^{+0.07}_{-0.06}$	$0.77^{+0.07}_{-0.05}$
4.SW	$0.18^{+0.11}_{-0.08}$	$4^{+2}_{-2}$	$0.07^{+0.11}_{-0.03}$	$0.33^{+0.20}_{-0.15}$	$0.56^{+0.30}_{-0.25}$

Note. The SFRs are averaged over the past 30 Myr. For the E and SW clumps near galaxy 4, we also fix the redshifts at  $z = 1.146$ .

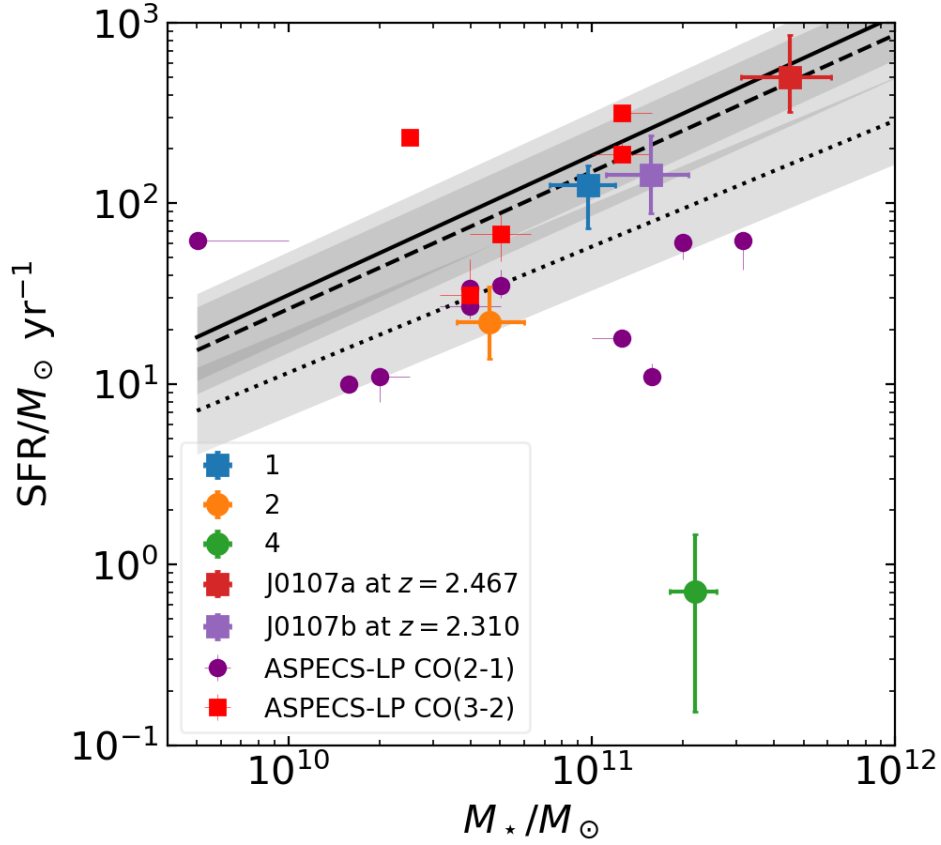


**Figure 6.** The positions of the five galaxies with CO redshift in the SFR- $M_*$  plane. The  $M_*$  and SFRs are derived from SED modeling (Table. 4). Circles mark galaxies detected with CO(2-1) while squares mark those with CO(3-2). The MS relations at  $z = 1.1$ ,  $z = 2.1$ , and  $z = 2.5$  are shown with dotted, dashed, and solid lines, respectively. The shaded regions indicate the scatter of the MS.

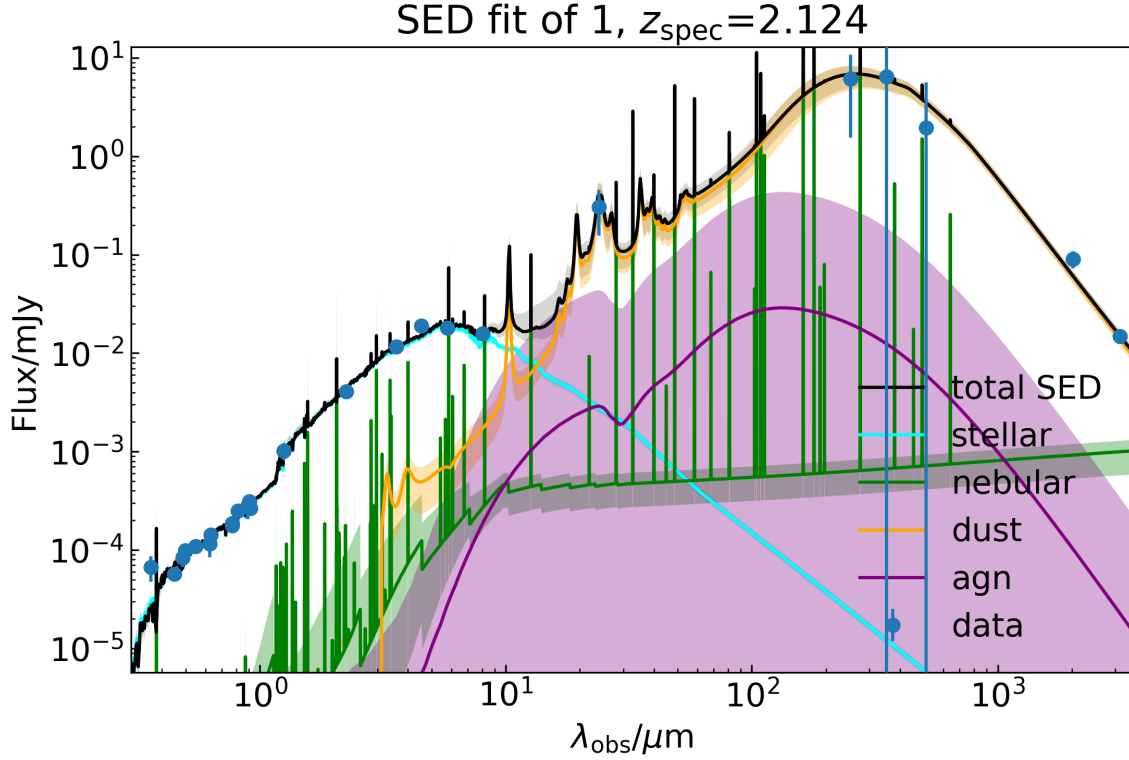


**Figure 7.** Median (solid lines) and 16th-84th percentile range (shaded regions) SEDs of galaxy 1 in the SSA22-AzTEC26 field, with individual components shown. The arrows indicate the ALMA  $3\sigma$  flux upper limits used in the SED fitting. MIPS and Herschel fluxes from Bayesian deblending (Section 2.3.2) are directly fitted, regardless of S/N. The number of stacked ALMA sources with peak S/N > 2 is less than 10 in the  $u$  and NB359 bands, so the flux excesses of galaxy 4 in these bands might result from deblending issues due to poorly aligned astrometry.

2019). Tests on simulated galaxies show the nonparametric SFH used in this study gives a larger  $M_*$  than simple exponential SFH models ( $\sim 0.3$  dex; Leja et al. 2019a; Lower et al. 2020). However, the results should still agree within error for the same object, as long as each method allows a wide range of SFHs and dust curves.

All three galaxies with CO-based redshift are massive, with  $M_* > 10^{10.5} M_\odot$  but different levels of star formation. Galaxies 1 and 2 lie within the scatter of the MS at their redshifts. In contrast, galaxy 4 is quiescent, with specific SFR  $\text{sSFR} = \text{SFR}/M_* = 0.9^{+2.8}_{-0.8} \times 10^{-12} \text{ yr}^{-1}$  and  $\log(\Delta\text{MS}) = \log(\text{SFR}/\text{SFR}_{\text{MS}}) = -2.7^{+0.6}_{-0.9}$  (or  $\text{sSFR} = 6.6^{+2.5}_{-1.5} \times 10^{-11} \text{ yr}^{-1}$  and  $\log(\Delta\text{MS}) = -0.9 \pm 0.1$  when using UV+IR SFR estimates). Compared with the ASPECS-LP galaxies, galaxies 1 and 2 have comparable  $M_*$  and SFR, but galaxy 4 is a significant outlier, with SFR much lower than the median value ( $30 M_\odot \text{ yr}^{-1}$ ) for galaxies detected with

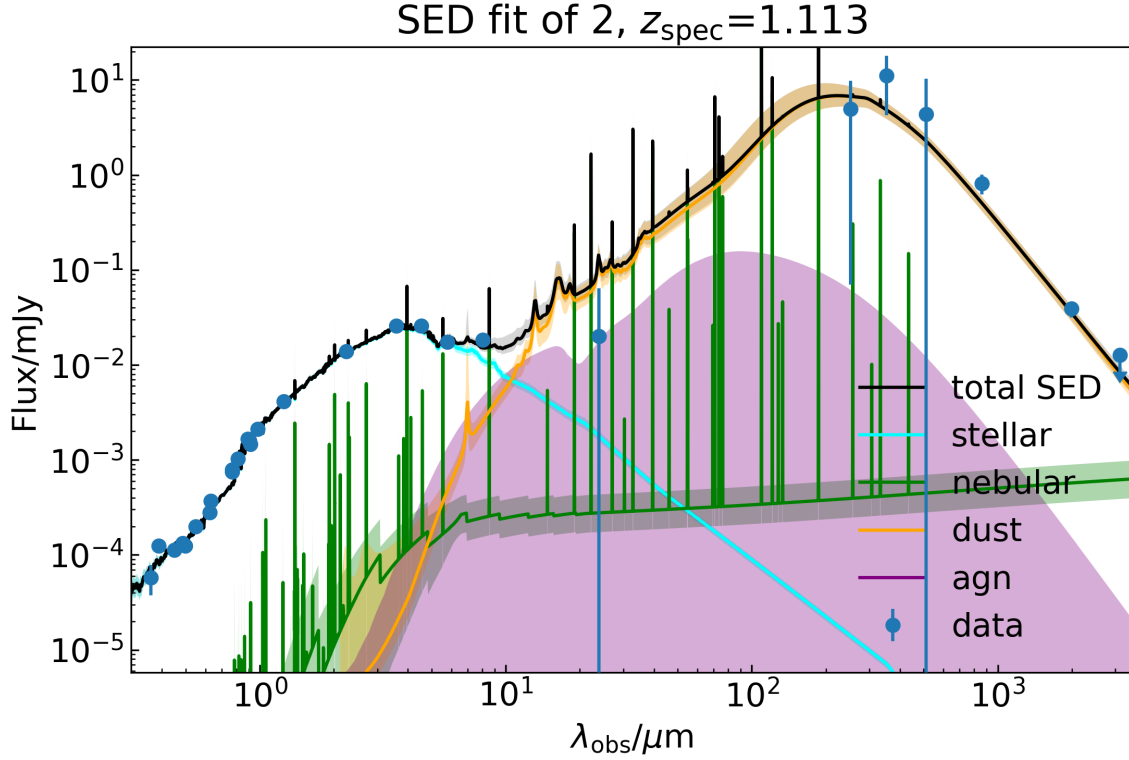


**Figure 8.** The same as Figure 7 but for galaxy 2 in the SSA22-AzTEC26 Field.

CO(2-1) in the ASPECS-LP survey. The ALMA band 3 data of the VV114 field has an RMS noise level three times of the SSA22-AzTEC26 field, and the two CO-detected galaxies in the VV114 field are on the MS but more massive and have higher SFR.

### 2.4.3 Molecular Gas Mass

In order to derive their molecular gas mass, we first convert the CO luminosity to the ground transition, assuming line ratios  $r_{21} = 0.76 \pm 0.09$  and  $r_{31} = 0.42 \pm 0.07$  appropriate for high-redshift normal SFGs (Daddi et al. 2015; Decarli et al. 2016). The total molecular gas mass  $M_{\text{mol}}$  is calculated using the conversion factor of normal SFGs:  $\alpha_{\text{CO}} = M_{\text{mol}}/L'_{\text{CO}(1-0)} = 3.6 M_{\odot}/(\text{K km s}^{-1} \text{ pc}^2)$ ; (Daddi et al. 2010b). The resulting gas masses are listed in Table. 2. For galaxy 1, we can also estimate  $M_{\text{mol}}$  from the [CI] line flux. The conversion factor  $\alpha_{[\text{CI}](1-0)} = M_{\text{mol}}/L'_{[\text{CI}](1-0)}$  is calculated using the equation 11 of Dunne et al. (2022):

$$\frac{\alpha_{[\text{CI}](1-0)}}{M_{\odot}(\text{K km s}^{-1} \text{ pc}^2)^{-1}} = 16.8 \left( \frac{X_{\text{CI}}}{1.6 \times 10^{-5}} \right)^{-1} \left( \frac{Q_{10}}{0.48} \right)^{-1}, \quad (5)$$

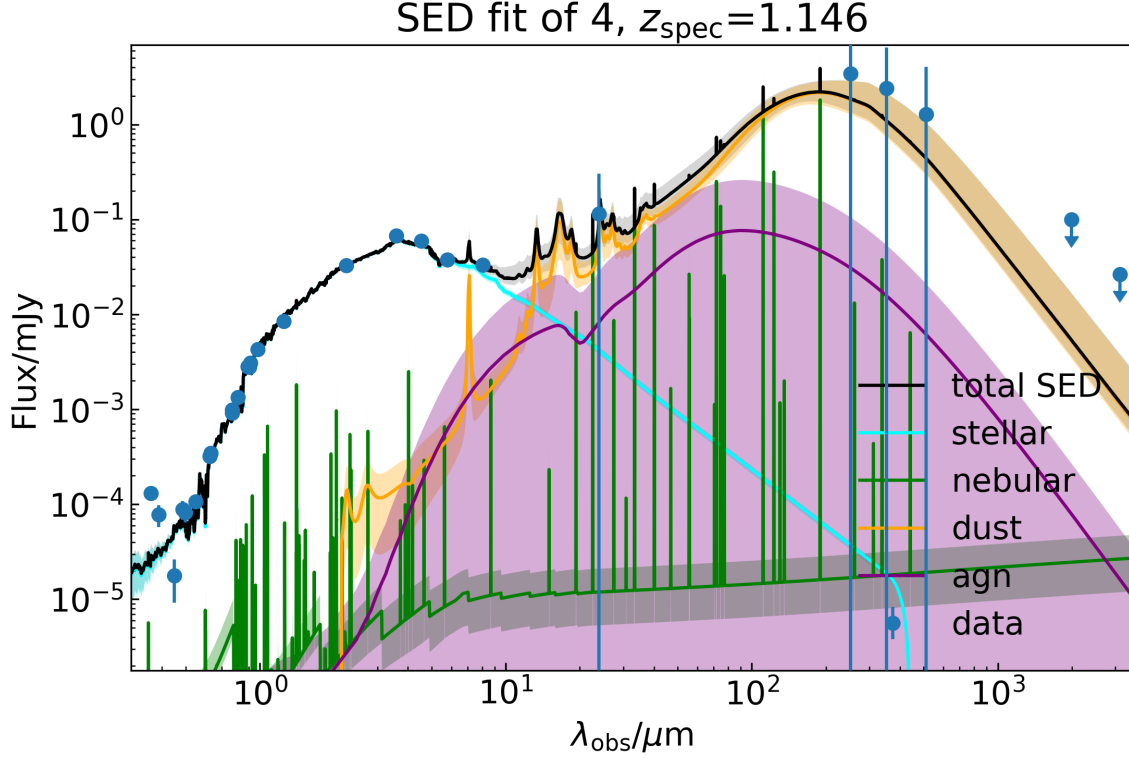


**Figure 9.** The same as Figure 7 but for galaxy 4 in the SSA22-AzTEC26 Field.

where  $X_{\text{CI}}$  is the average abundance ratio of atomic carbon and  $Q_{10}$  is the excitation term. We adopt  $X_{\text{CI}} = 10^{-4.8}$  and  $Q_{10} = 0.35$  following Lee et al. (2021). Using the band 4 data, we find the velocity-integrated [CI](1-0) line flux  $S_{[\text{CI}](1-0)}\Delta v = 0.320 \pm 0.044 \text{ Jy km s}^{-1}$ . This translates to a [CI](1-0)-based molecular gas mass of  $(9.4 \pm 1.3) \times 10^{10} M_{\odot}$ , roughly consistent with the CO-based gas mass.

We note that molecular gas mass estimates suffer from substantial uncertainties in  $\alpha_{\text{CO}}$  and excitation. In this study, we have adopted  $\alpha_{\text{CO}}$  and line ratios of normal SFGs. Some recent ALMA studies have revealed compact star formation with intense starburst-like conditions in high-redshift MS galaxies, or “hidden starburst in the MS” (e.g., Puglisi et al. 2021). In this case, starburst-like conversions should be used to derive gas mass, despite their SFR being within the scatter of the MS. If we instead assume SMG-like  $\alpha_{\text{CO}} = 1.36 M_{\odot}/(\text{K km s}^{-1} \text{ pc}^2)$ ,  $r_{21} = 0.84 \pm 0.13$  and  $r_{31} = 0.52 \pm 0.09$  (Bothwell et al. 2013), the gas mass will decrease by 2.96 and 3.28 times for CO(2-1) and CO(3-2), respectively. For the [CI](1-0) line, with SMG-like  $X_{[\text{CI}]} = 10^{-4.2}$  and  $Q_{10} = 0.48$  (Walter et al. 2011; Valentino et al. 2018) the estimated molecular gas mass of galaxy 1 becomes  $(1.7 \pm 0.2) \times 10^{10} M_{\odot}$ , or 45% of the CO-based gas mass.

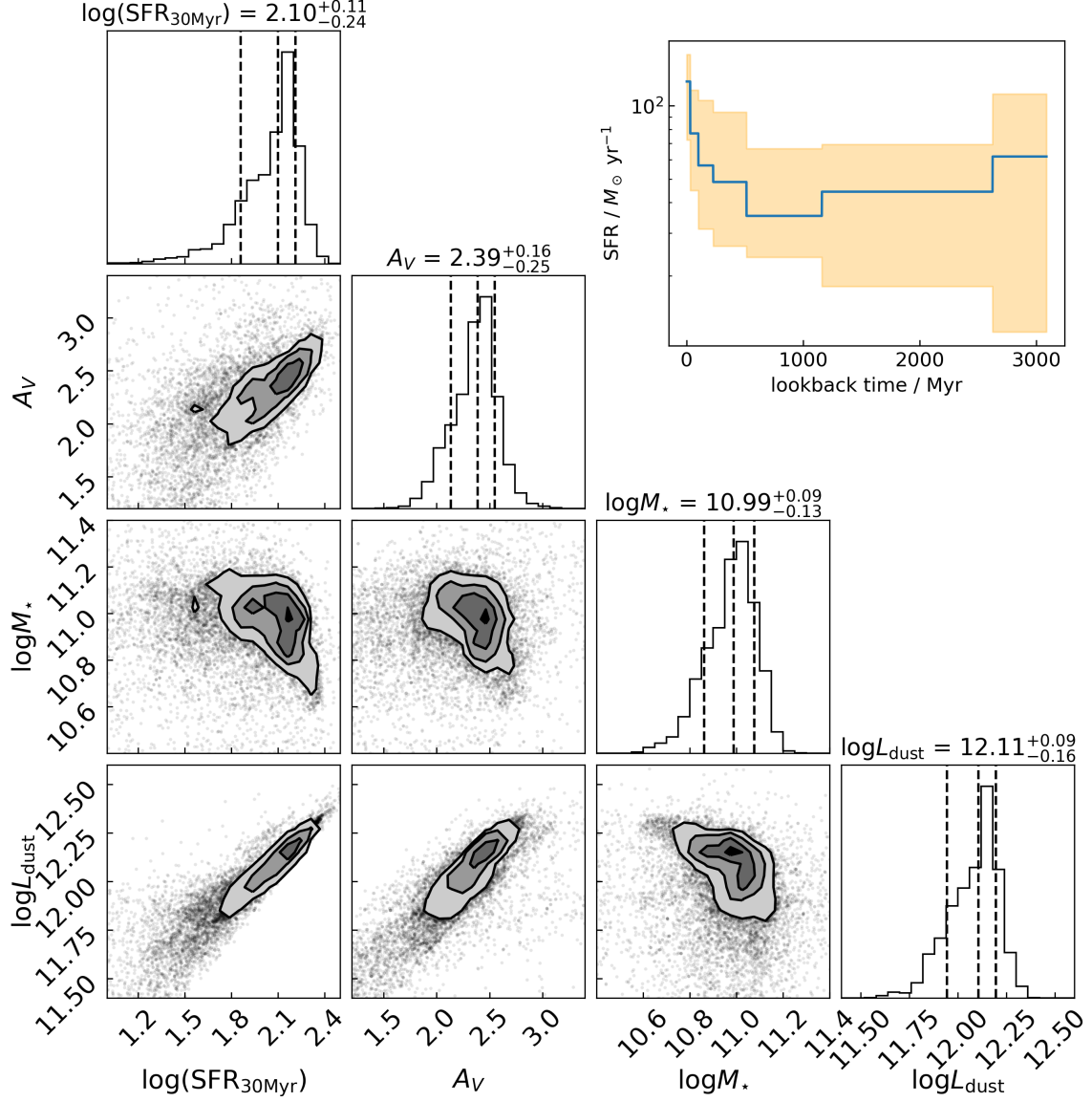


**Figure 10.** Joint posterior distribution of derived physical parameters of galaxies 1 in the SSA22-AzTEC26 Field. Inserted panels show SFH from SED fitting with a blue solid line for the median and orange region for the 68% percentile range.

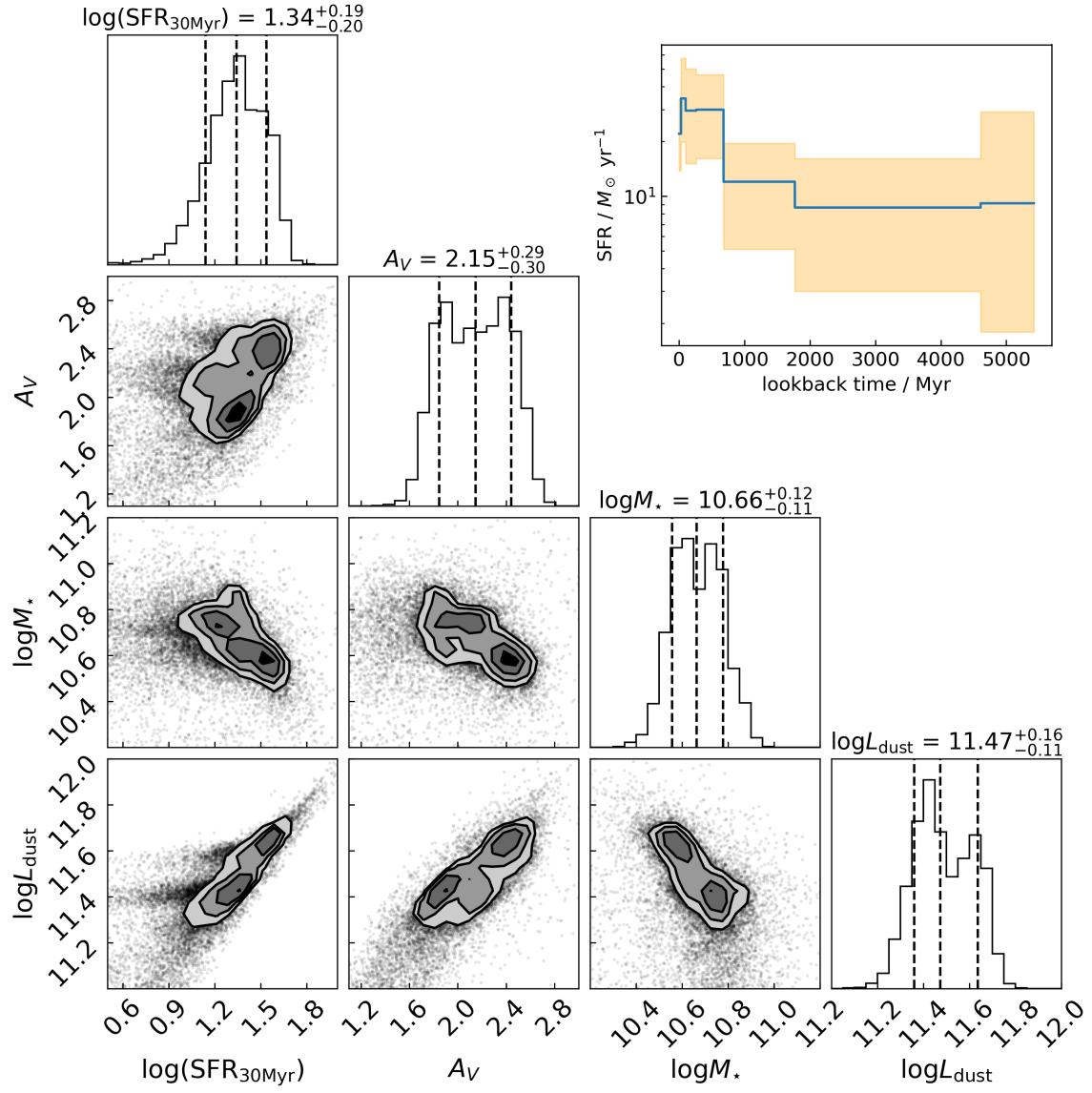


**Figure 11.** The same as Figure 10 but for galaxy 2 in the SSA22-AzTEC26 Field.

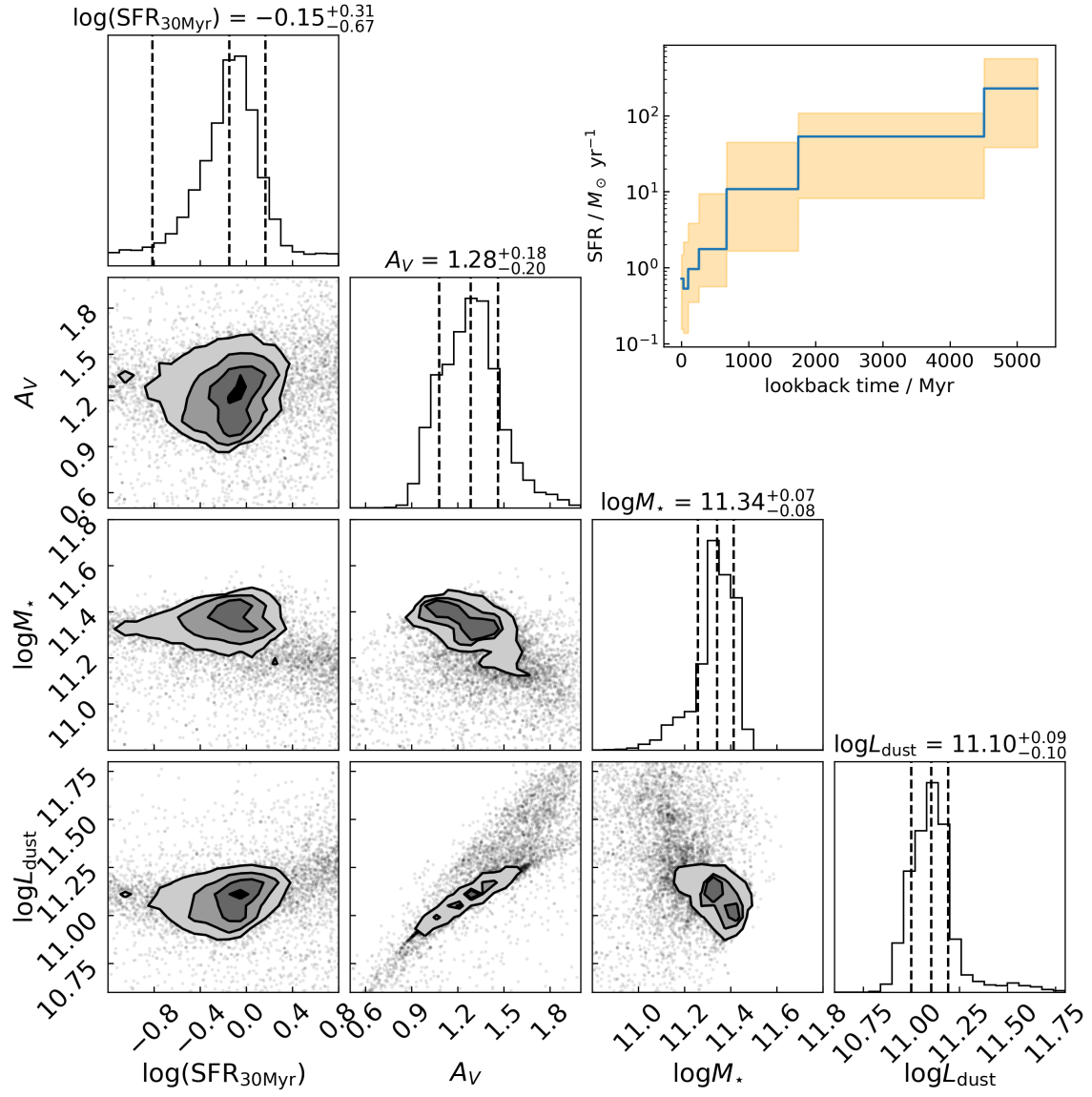


**Figure 12.** The same as Figure 10 but for galaxy 4 in the SSA22-AzTEC26 Field.



Our observations provide three tracers of the molecular gas, namely CO, [CI], and Rayleigh-Jeans tail dust continuum. However, there is a discrepancy between the derived  $M_{\text{mol}}$  using CO and dust in one of the two galaxies with continuum detection. Under normal SFG conversions of CO, galaxy 2 has a gas-to-dust mass ratio  $\delta_{\text{GDR}} = 126^{+39}_{-26}$  with  $M_{\text{dust}}$  from the SED fitting, which is consistent with  $\delta_{\text{GDR}} = 103$  from scaling relations (e.g., [Maiolino et al. 2008](#); [Leroy et al. 2011](#); [Genzel et al. 2015](#)). In contrast, galaxy 1 has  $\delta_{\text{GDR}} = 396^{+105}_{-81}$ , more than three times higher than  $\delta_{\text{GDR}} = 111$  expected by the  $M_{\star}$ -metallicity-redshift and metallicity- $\delta_{\text{GDR}}$  scaling relations.

For galaxy 1, SMG-like conversions bring  $\delta_{\text{GDR}} = 121^{+32}_{-25}$  into an agreement with the scaling relations, but this cannot be used to justify SMG-like conversion for galaxy 1. The dust-based  $M_{\text{mol}}$  is the least robust here, because of low S/N ( $< 2$ ) in all Herschel bands and the uncertainty in the dust SED fitting (e.g., [Berta et al. 2016](#)). The position of galaxy 1 with respect to the  $L_{\text{dust}} - L'_{\text{CO}(1-0)}$  relation also disfavors a starburst nature of galaxy 1. [Genzel et al. \(2010\)](#) find  $\log(L_{\text{dust}}) = 1.15 \log(L'_{\text{CO}(1-0)}) + 0.02 \pm 1.1$  for normal SFGs and the same slope, but with an intercept of  $0.63 \pm 0.12$ , for starbursts. For galaxy 1's  $L_{\text{dust}} = 12.11^{+3.57}_{-3.55} \times 10^{11} L_{\odot}$  and  $L'_{\text{CO}(3-2)} = (1.45 \pm 0.19) \times 10^{10} \text{ K km s}^{-1} \text{ pc}^2$ , we derive  $\log(L_{\text{dust}}/L'_{\text{CO}(1-0)})^{1.15} = -0.02^{+0.12}_{-0.16}$  under normal SFG conversion or  $0.08^{+0.12}_{-0.17}$  under SMG conversion, thus the galaxy seems to be closer to a normal SFG. In the following discussion, we continue using  $M_{\text{mol}}$  from normal SFG conversions.

## 2.5 Discussion: Comparison with Molecular Gas Scaling Relations and the Discovery of a Gas-rich Quiescent Galaxy Candidate

### 2.5.1 Comparison with Molecular Gas Scaling Relations

The left panel of Figure 13 shows the gas ratio  $\mu_{\text{mol}} = M_{\text{mol}}/M_{\star}$  of our sample and values of SFGs and QGs across cosmic time, color-coded by  $\log(M_{\star}/M_{\odot})$ . The SFG sample is collected from [Tacconi et al. \(2018\)](#), which uses the [Genzel et al. \(2015\)](#) metallicity-dependent prescription— $\alpha_{\text{CO}} = 3.8 - 12.4 M_{\odot} (\text{K km s}^{-1} \text{ pc}^2)^{-1}$  for  $z = 0 - 4$  and  $\log(M_{\star}/M_{\odot}) = 9 - 12$ . The  $M_{\text{mol}}$  of QGs in the comparison sample is derived using Galactic  $\alpha_{\text{CO}}$ . At  $z = 1 - 1.5$ , the  $\text{SFR} > 30 M_{\odot} \text{ yr}^{-1}$  and  $M_{\star} > 2.5 \times 10^{10} M_{\odot}$  cuts of the PHIBSS1 survey make their preselection slightly higher than MS SFR at this redshift, resulting in a median  $\mu_{\text{mol}}$  of 0.79. This is higher than  $\mu_{\text{mol}} = 0.63^{+0.20}_{-0.15}$  of galaxy 2 or  $0.28^{+0.09}_{-0.06}$  of galaxy 4. Similar differences have been found by the ASPECS-Pilot survey ([Decarli et al. 2016](#)), which found that CO(2-1) emitters from their ALMA band 3 line search in the HUDF field have a median SFR of  $34 M_{\odot} \text{ yr}^{-1}$  and a  $\sim$ two times lower median gas ratio than PHIBSS1. Also, in the subsequent larger ASPECS-LP sample ([Aravena et al. 2019](#)), the galaxies detected with CO(2-1) have median  $z = 1.20$  and  $\mu_{\text{mol}} = 0.48$ . At  $z > 2$ , the median gas ratio

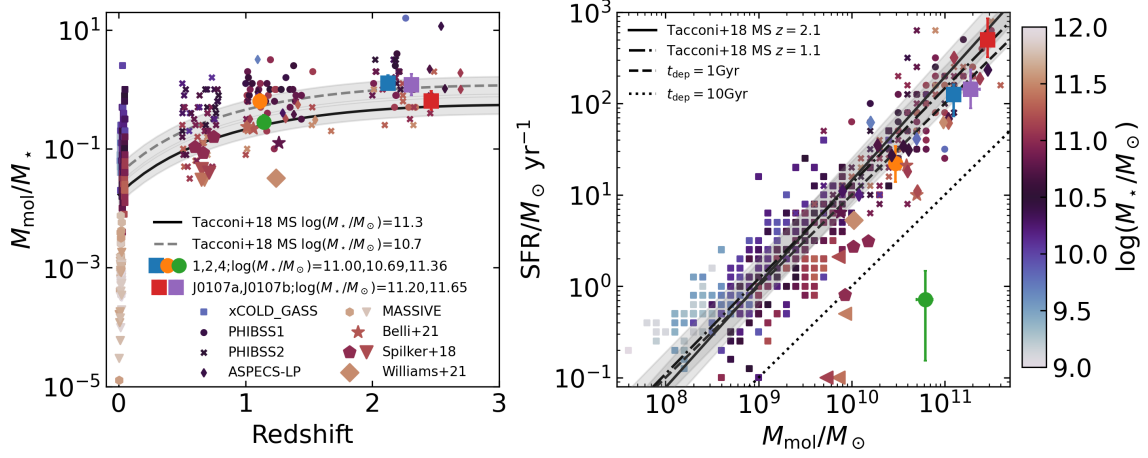


**Figure 13.** Left: molecular gas fraction as a function of redshift. For comparison, we show the scaling relation and its scatter from Tacconi et al. (2018), local SFGs (xCOLD GASS; Saintonge et al. 2017), intermediate- and high redshift star-forming galaxies (PHIBSS1/2; Tacconi et al. 2013; Freundlich et al. 2019), local QGs (MASSIVE; Davis et al. 2019), intermediate- and high-redshift QGs (Spilker et al. 2018; Belli et al. 2021; Williams et al. 2021). The triangles indicate upper limits. Right: SFR as a function of  $M_{\text{mol}}$ . The symbols are the same as in the left panel.

of PHIBSS1 galaxies is  $1.26$ , comparable with  $\mu_{\text{mol}} = 1.28^{+0.49}_{-0.29}$  of galaxy 1 or  $\mu_{\text{mol}} = 1.20^{+0.62}_{-0.41}$  of J0107b, only higher than  $\mu_{\text{mol}} = 0.64^{+0.31}_{-0.19}$  of the ultramassive galaxy J0107a. This is because the PHIBSS surveys' SFR and  $M_*$  cuts do not bias the sample to galaxies above the MS at  $z > 2$ . Our sample further contains one galaxy that is significantly below the MS, showing that a blind line search is able to cover a wider range of star formation levels.

The right panel of Figure 13 shows SFR as a function of  $M_{\text{mol}}$ . The two quantities are closely correlated with the modest time evolution of depletion time  $t_{\text{dep}} = M_{\text{mol}}/SFR \propto (1+z)^{-0.63}$  (Tacconi et al. 2018). In our sample, galaxies 1 and 2 show a lower SFR at a given  $M_{\text{mol}}$  compared to the targeted SFGs in the PHIBSS1 survey, but their  $t_{\text{dep}} = 1.0^{+0.7}_{-0.3}$  and  $1.3^{+0.8}_{-0.5}$  Gyr agree with the scaling relation, which expects  $\sim 0.7$  and  $\sim 1$  Gyr, respectively. This might be caused by the difference in the methods for deriving SFR and  $M_*$ . As mentioned in Section 2.4.2, the full UV-to-FIR SED fitting method with nonparametric SFH used in this study typically gives lower SFR and larger  $M_*$ . Such a trend is also found by ASPECS-LP (Aravena et al. 2019), as they use MAGPHYS, which also includes dedicated treatments of SFH and dust attenuation. In summary, while the target selection and methodology of analysis are different, our sample shows that the current scaling relations successfully describe the evolution of gas content as a function of redshift, mass, and SFR in SFGs.

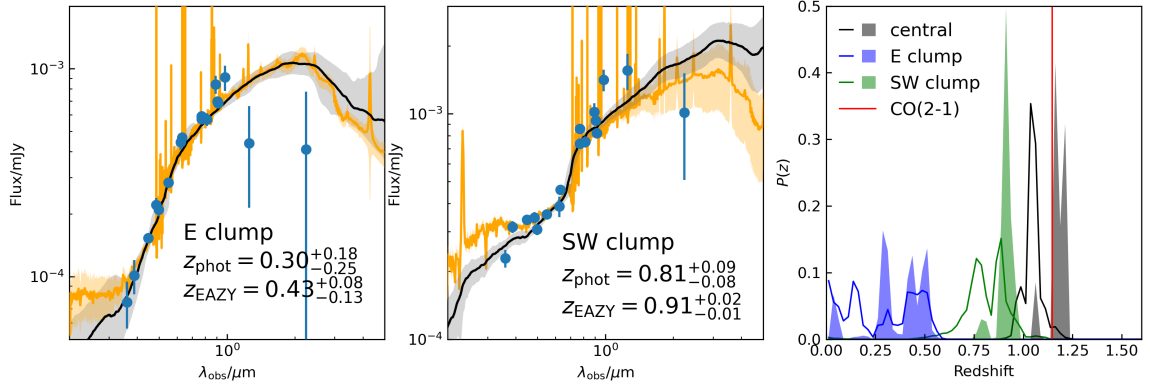


**Figure 14.** Left: deblended SED for the E clump. The median (or best-fit for EAZY) and 16th-84th percentile ranges of the SED fit are shown as the solid lines and shaded regions, with black color for the method in section 2.3.3 and orange color for the EAZY code. Middle: the same as left but for the SW clump. Right: the photometric redshift PDF  $P(z)$  of the central galaxy, E, and SW clumps. The solid lines show the photometric redshift from the SED fitting method in section 2.3.3 and the shaded regions are the results from the EAZY code.

### 2.5.2 A Gas-rich Quiescent Galaxy Candidate at $z = 1.146$

The most surprising finding from the analysis above is the large gas reservoir in the massive galaxy 4 with low sSFR. The analysis is based on the assumption that the two blue clumps (E and SW; Figure 4) are not physically associated with the CO(2-1) emission. If we ignore the clustering effect, so that galaxies are uniformly distributed, the probability of the chance alignment of a galaxy  $i$  can be expressed as (Bloom et al. 2002):

$$P_{\text{chance}} = 1 - \exp(-\sigma_i \pi r_i^2), \quad (6)$$

where  $\sigma_i$  is the surface density of sources brighter than galaxy  $i$  and  $r_i$  is the sky separation between the CO detection and galaxy  $i$ . Using the  $B$ -band image we measure  $\sigma_i = 0.011 \text{ arcsec}^{-2}$ ,  $r_i = 1''.34$  for the E clump and  $\sigma_i = 0.006 \text{ arcsec}^{-2}$ ,  $r_i = 1''.03$  for the SW clump. The random coincidence rate of two such galaxies is  $1.18 \times 10^{-3}$ . This low probability rejects the null hypothesis that the two clumps are randomly aligned at the  $3.2\sigma$  level. To assess whether this is a rare case of random alignment, we further examine the SED and physical properties of the two blue clumps and the central massive galaxy.

As shown in the right panel of Figure 14, the photometric redshifts from our SED fitting method are  $0.30^{+0.18}_{-0.25}$  and  $0.81^{+0.09}_{-0.08}$  for the E and SW clumps, respectively. Only the SW clump has a nonzero probability at  $z = 1.146$ . Meanwhile, the photometric redshifts from EAZY do not overlap with the redshift of the CO(2-1) emission line. On the other hand, by fitting the deblended photometry of the two clumps at fixed

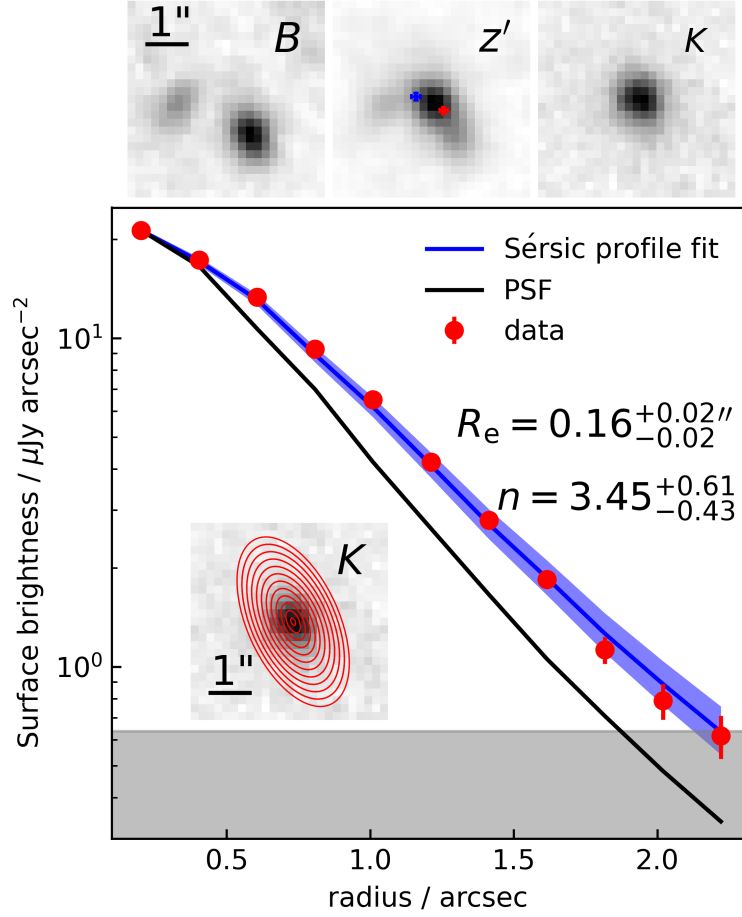


**Figure 15.** Top:  $5'' \times 5''$  cutout stamps centered at the CO position in  $B$ ,  $z'$  and  $K$  bands. The blue and red error bars in the  $z'$  band image mark the centroids of the two velocity components of the CO emission. Bottom:  $K$ -band surface brightness distribution along the major axis. The data points are derived from the  $K$ -band image without neighbor subtraction using the elliptical annuli shown in the insert panel. The black line indicates the PSF. The blue solid line and shaded region are the median and 16th-84th percentile range of the 2D Sérsic model of the central galaxy, which is derived by fitting three objects jointly (section 2.3.1). The gray region represents the RMS of a single pixel.

$z = 1.146$ , we derive  $\text{SFR} = 9_{-1}^{+1} M_{\odot} \text{ yr}^{-1}$ ,  $M_{\star} = 0.03_{-0.01}^{+0.02} \times 10^{10} M_{\odot}$  for the E clump and  $\text{SFR} = 4_{-2}^{+2} M_{\odot} \text{ yr}^{-1}$ ,  $M_{\star} = 0.18_{-0.08}^{+0.11} \times 10^{10} M_{\odot}$  for the SW clump (Table 4).

High-redshift galaxies have been shown to host blue clumpy structures, which are the sites of star formation (e.g., Elmegreen et al. 2009). However, the properties of the two clumps surrounding galaxy 4 are incompatible with such a picture. Firstly, the central galaxy appears like a spheroid (Figure 15) without a disk component, which is the expected location of star-forming clumps. Also, the clumps are outside the central galaxy, because the separations of  $\sim 1''$  are larger than the  $R_e = 0''.16 - 0''.35$  of individual components. Secondly, the sizes of the two clumps are too large compared to the central galaxy. For the central spheroid, we measure  $R_e = 0.16_{-0.02}^{+0.02}$  arcsec, while the E clump has  $R_e = 0.30_{-0.08}^{+0.09}$  arcsec and the SW clump has  $R_e = 0.35_{-0.01}^{+0.01}$  arcsec. Assuming the spherical symmetry of the central spheroid and thickness =  $0.1 R_e$  disk of the two clumps, and using  $M_{\star}$  from the SED fitting (Table 4), the Roche limit is  $\sim 2''.8$  for the E clump and  $\sim 1''.8$  for the SW clump in the image plane. This means the tidal force from the central massive galaxy will destruct these two clumps to form a ring or disk if the two clumps are located inside the sphere with the Roche radius. However, such features are not seen in the image. Last, the centroids of the blue and red components of the CO(2-1) emission are closer to the central galaxy (the  $z'$  band cutout in Figure 14). If the CO emission is from the two clumps, the  $\mu_{\text{mol}}$  will be  $\sim 100$  for the E clump and  $\sim 15$  for the SW clump under  $\alpha_{\text{CO}} = 3.6 M_{\odot} (\text{K km s}^{-1} \text{ pc}^2)^{-1}$  and  $r_{21} = 0.76$ . Such an extreme molecular gas-rich dwarf has not been detected in the local universe (Saintonge et al. 2017).

Overall, the positions and properties of the two clumps near galaxy 4 suggest that they are likely to be interlopers rather than companions or parts of the central massive galaxy, from which the CO emission originates. Future optical/NIR spectroscopy is needed to obtain accurate redshifts and verify the discussion presented above.

CO/dust observations of QGs outside the local universe based on preselection of sSFR typically find a low gas fraction of  $\mu_{\text{gas}} \lesssim 10\%$  (Sargent et al. 2015; Spilker et al. 2018; Bezanson et al. 2019; Caliendo et al. 2021; Williams et al. 2021, see also the left panel of Figure 13 for CO samples). On the other hand, higher values of  $\mu_{\text{mol}}$  in QGs have also been reported (Rudnick et al. 2017; Gobat et al. 2018; Hayashi et al. 2018; Belli et al. 2021). Here, galaxy 4 has  $M_{\text{mol}} = (6.2 \pm 1.2) \times 10^{10} M_{\odot}$  and  $\mu_{\text{gas}}$  of  $0.28_{-0.06}^{+0.09} (\alpha_{\text{CO}}/3.6 M_{\odot} (\text{K km s}^{-1} \text{ pc}^2)^{-1}) ((0.76 \pm 0.09)/r_{21})$ , adding one more candidate to gas-rich QGs. With the results, we infer a very low star formation efficiency (SFE) of galaxy 4 with  $\text{SFE} = 1/t_{\text{dep}} = 1.15_{-0.89}^{+1.44} \times 10^{-11} \text{ yr}^{-1}$ . The SFE is not only lower than the targeted SFGs in the PHIBSS surveys, but also lower than any blindly detected galaxies from ASPECS-LP, which has the lowest  $\text{SFE} = 2.2_{-0.3}^{+0.5} \times 10^{-10} \text{ yr}^{-1}$ . In contrast, preselected QGs detected in CO at  $z \gtrsim 1$  show SFEs closer to normal SFGs (the right panel of Figure 13)

If the gas reservoir is left over after the end of the main star formation episode without being depleted or destroyed, there must be some mechanisms to halt new star formation. In bulge-dominated systems, the gas disk can be stabilized against collapse (Martig et al. 2009; Genzel et al. 2014), so further star formation is dynamically suppressed. However, the gas fraction of galaxy 4 is too high for morphological quenching to effectively reduce the star formation ( $\lesssim 5\%$ ; Martig et al. 2013; Gensior et al. 2020), though its contribution to maintaining quiescence is possible (Gensior & Kruijssen 2021). From the SFH (Figure 8), we see that the bulk of stars were formed  $\gtrsim 2$  Gyr ago and the SFR drops after  $z \sim 2$ , with a mass-weighted stellar age of  $3.3^{+1.4}_{-0.4}$  Gyr. Other sources such as supernovae or active galactic nuclei (Nesvadba et al. 2010) can also inject kinematic energy into the ISM and prevent collapse, but these processes take place on shorter timescales ( $\lesssim 100$  Myr; Guillard et al. 2015) and may also remove the cold gas, so they are at least not the main reason for galaxy 4’s quiescence while maintaining a high gas fraction. Finally, the  $\gtrsim 1$  Gyr lookback time is much longer than the remaining lifetime of the gas reservoir after the quenching inferred from post-starburst galaxies ( $\sim 150$  Myr; Bezanson et al. 2022). Thus, the gas reservoir in galaxy 4 is no likely to be the remnant of the past major star formation event, but the listed mechanisms might have played a role in maintaining the low SFE.

Alternatively, the gas reservoir might be acquired in late times (Woodrum et al. 2022). Since galaxy 4 is already very massive ( $M_\star > 10^{11} M_\odot$ ), its halo mass will be  $M_{\text{halo}} > 10^{12.5} M_\odot$  assuming a stellar-to-halo mass ratio of  $-1.5$  dex (Behroozi et al. 2013). At this  $M_{\text{halo}}$ , shock heating can suppress further cold gas supply via accretion from the surrounding environment (Kereš et al. 2005; Dekel & Birnboim 2006). Rather than accretion, several minor mergers could have added gas to galaxy 4. According to the MS gas scaling relation, a normal galaxy with one-hundredth to one-quarter of galaxy 4’s  $M_\star$  and redshift  $1.146 - 2$  carries  $M_{\text{gas}} \sim 0.3 \times 10^{10} M_\odot - 4.8 \times 10^{10} M_\odot$ . Integrating the merger rate found by the Illustris simulation (Rodríguez-Gomez et al. 2015) over this mass and redshift range, there are 2.9 mergers expected and  $3.4 \times 10^{10} M_\odot$  of added molecular gas, which is only half of the gas mass of galaxy 4. The minor merger scenario also struggles to explain the low SFR, though it does not necessarily elevate the SFR immediately, due to dynamical effects (Davis et al. 2015; van de Voort et al. 2018). If minor mergers really happened to galaxy 4, there should be some imprints left in it, such as stellar gas misalignment (e.g., Khim et al. 2021). The CO data show that a rotating gas disk might exist in galaxy 4 (Figure 3), but currently we cannot perform kinematic diagnostics, due to a lack of optical/NIR spectroscopic data. We conclude that none of the mechanisms discussed above can explain galaxy 4’s high gas fraction alone, and future high-resolution observations are needed to reveal the nature of galaxy 4. Such observations may include high-resolution optical/NIR imaging to study stellar morphology; confirmations of quiescence and relations with neighbor

sources using optical/NIR spectroscopy; and interferometric observation of CO line kinematics, especially for diagnostics of stability via Toomre  $Q$  parameter, temperature, and the density of its gas disk.

### 2.5.3 Caveats of Galaxy 4's SFR Estimate

We caution that the current identification of galaxy 4 as a QG is only tentative. The assertion of the low SFR is based on very faint rest-frame UV fluxes and the obscured SFR of galaxy 4 is left not well constrained. In this  $M_*$  range, almost all of the star formation is obscured ( $> 90\%$ ; e.g., Whitaker et al. 2017), so FIR/radio observations are needed to measure the total SFR. The galaxy is not detected in Herschel SPIRE bands, which have a  $1\sigma$  depth of  $\sim 7$  mJy. The  $3\sigma$  upper limits of ALMA band 3/4 continuum fluxes are still one to two orders of magnitudes higher than that predicted by SED fitting (Figure 7). Assuming a modified blackbody model with dust temperature  $T_{\text{dust}} = 20 - 60$  K and emissivity index  $\beta = 1.5 - 2.0$ , the  $3\sigma$  upper limit of the 2 mm continuum flux density  $S_{2\text{mm}} < 0.1$  mJy translates to  $L_{\text{dust}} < 0.4 - 26.9 \times 10^{11} L_{\odot}$  or  $\text{SFR} < 4 - 294 M_{\odot} \text{ yr}^{-1}$  for dust heated by star formation.

A similar constraint on SFR can be obtained from JVL A 3 GHz observations (Ao et al. 2017) of the SSA22 field. The radio observations have a PB response of  $\sim 0.13$  at the position of galaxy 4, resulting in a  $3\sigma$  upper limit of  $33 \mu\text{Jy}$  at 3 GHz. Assuming a radio spectral index of  $-0.7$  (i.e.,  $S_{\nu} \propto \nu^{-0.7}$ ) and  $\text{SFR}/(M_{\odot} \text{ yr}^{-1}) = 6.35 \times 10^{-22} L_{1.4\text{GHz}}/(\text{W Hz}^{-1})$  (Murphy et al. 2011), the flux upper limit implies an SFR upper limit of  $\sim 220 M_{\odot} \text{ yr}^{-1}$ . Obviously, current FIR and radio data are not deep enough to constrain galaxy 4's SFR. Future follow-up observation at submillimeter/millimeter wavelengths will be critical to confirm its quiescence. If our current SFR estimate of galaxy 4 is broadly correct, this object will be particularly interesting for future studies, to test galaxy quenching scenarios, as discussed in the previous subsection.

## 2.6 Summary of Section 2

In this section, we have analyzed the data from  $\sim 29$  GHz bandwidth ALMA band 3 spectral scan observations toward SMG SSA22-AzTEC26 and detected four line emitters with S/N above 5.2 in a spectral cube smoothed with a  $300 \text{ km s}^{-1}$  FWHM Gaussian filter, after masking the central SMG. We combine ALMA band 4/7 and multiwavelength ancillary data to derive the photometric redshift and their physical properties. Our main findings are:

1. Using the photometric redshift, we identify that two of the sources are CO(2-1) at  $z = 1.113$  and  $z = 1.146$  respectively. Another is CO(3-2) at  $z = 2.124$  and confirmed with [CI](1-0) emission line detected in the ALMA band 4 observation. The remaining source might be  $z_{\text{CO}(2-1)} = 1.512$  or  $z_{\text{CO}(3-2)} = 2.767$  and need to be verified by future observations.

2. All three sources with a CO redshift solution are massive galaxies ( $M_\star > 10^{10.5} M_\odot$ ), with SFR in the order of  $\sim 1 - 100 M_\odot \text{ yr}^{-1}$ . Two of them lie within the scatter of the MS and the most massive galaxy 4 is significantly below the MS.

3. Using the CO data, we estimate a molecular gas mass of  $2.9 - 12.5 \times 10^{10} M_\odot$  under the assumption of normal SFG excitation and  $\alpha_{\text{CO}}$ . We compare different gas tracers and conversion factors, finding that our current choice of normal SFG excitation and  $\alpha_{\text{CO}}$  seems to be appropriate. The gas fraction and  $t_{\text{dep}}$  of galaxies 1 and 2 are consistent with the gas scaling relation. However, the most massive one, galaxy 4, is likely quiescent but maintains a gas ratio of  $\sim 28\%$ , comparable with SFGs on the MS.

It is difficult to explain the large gas reservoir of galaxy 4 as being left over after quenching because of its high gas fraction and old stellar age. We speculate that the gas content was obtained in later times, via accretion or minor mergers, while various quenching mechanisms might have acted to suppress the star formation. Future high-resolution observations are needed to investigate the stellar and gas kinematics to understand the origin of the large gas reservoir and the exact quenching channels in this galaxy.



### 3 Serendipitously Detected CO Line Sources in the VV114 Field<sup>3</sup>

#### 3.1 Introduction of This Section

During cosmic noon, dusty star-forming galaxies (DSFGs) populate the massive and high-SFR end of star-forming galaxies, with  $M_{\star} \sim 10^{11} M_{\odot}$  and  $\text{SFR} \sim 100 - 1000 M_{\odot} \text{ yr}^{-1}$  (e.g., da Cunha et al. 2015; Miettinen et al. 2017; Dudzevičiūtė et al. 2020). The large infrared luminosity of DSFGs makes them easy to be detected with submillimeter/millimeter observations, and they are often referred to as submillimeter galaxies (SMGs; e.g., Smail et al. 1997; Hughes et al. 1998; Casey et al. 2014)

The origin of DSFGs has been debated since their discovery. Based on insights from studying local ultraluminous infrared galaxies (ULIRGs), which are exclusively late-stage major mergers (e.g., Sanders & Mirabel 1996), and observations of high-redshift DSFGs, many authors have argued that bright DSFGs (or classical SMGs with  $S_{850\mu\text{m}} \gtrsim 5 \text{ mJy}$ ) are mainly major mergers (e.g., Tacconi et al. 2008; Engel et al. 2010; Chen et al. 2022a). Early theoretical models demonstrated that major mergers can indeed power bright DSFGs (e.g., Narayanan et al. 2010; Hayward et al. 2011), but it was unclear whether there were enough major mergers to account for the observed number counts of bright DSFGs. Hayward et al. (2011, 2012, 2013) argued that the high-redshift bright DSFG population is heterogeneous, with merger-driven starbursts dominating at the bright end and secular star-forming disks dominating at fainter submm fluxes. Others have argued that the DSFG population is predominantly gas-rich massive disks (i.e. not ongoing major mergers) that sustain high SFRs due to high gas accretion rates from the cosmic web (e.g., Dekel et al. 2009; Davé et al. 2010; Narayanan et al. 2015; Lovell et al. 2021).

Morphological information can thus place critical constraints on the formation channels of DSFGs by distinguishing disks and mergers. Previous studies using deep Hubble Space Telescope (HST) imaging have revealed a prevalence of disturbed morphology (e.g., Chen et al. 2015), inline with interaction or merger. However, due to the high redshift and heavy dust obscuration of DSFGs, the rest-frame UV/optical emission observed with HST might not be an ideal tracer of stellar distribution.

The advent of James Webb Space Telescope (JWST) makes rest-frame optical-to-NIR imaging with unprecedented sensitivity and spatial resolution available for DSFGs. Recent JWST studies of submm-selected galaxies have found a large fraction of isolated disks (Chen et al. 2022b; Cheng et al. 2023), in contrast to more clumpy and irregular shapes in HST bands. JWST rest-frame NIR imaging will provide a more robust view of the stellar distribution of DSFGs and hints for their possibly diverse formation channels.

---

<sup>3</sup>The analysis of J0107a in this section has been published in the Astrophysical Journal Letters: <https://iopscience.iop.org/article/10.3847/2041-8213/acff63>

In this section, we report J0107a, a  $z = 2.467$  DSFG with a clear barred spiral structure in JWST/NIRCam images and bright dust continuum and CO/[C I](1-0) line emission. We describe the observation in Section 3.2, then present data analyses and results in Section 3.3. We discuss the results in Section 3.4 and also briefly present another DSFG with line detection in the VV114 field, J0107b at  $z = 2.310$ , in Section 3.5.

## 3.2 Multiwavelength Dataset of the VV114 Field

### 3.2.1 The Target: ALMA J010748.3-173028 (J0107a)

The target of this study, J0107a was first identified by [Tamura et al. \(2014\)](#) as a serendipitously detected line emitter at the observed frequency of 99.75 GHz in ALMA band 3 observation towards the local galaxy merger VV114 at  $z = 0.0205$ . Based on photometric redshift, the line is identified as CO(3-2) at  $z = 2.467$ . The redshift is confirmed by [Mizukoshi et al. \(2021\)](#) with CO(3-2), CO(4-3), and [CI](1-0) emission lines (Figure 16a). J0107a is also detected in continuum with flux densities of  $3.4 \pm 0.3$  mJy at 1.3 mm and  $7.9 \pm 1.0$  mJy at 888  $\mu$ m, which satisfy the selection criteria of a classical SMG.

### 3.2.2 ALMA Data

J0107a has been covered by the ALMA campaigns toward VV114. In this study, we include ALMA band 3 (Project code 2013.1.00469.S and 2013.1.01057.S), band 4 (2013.1.01057.S), band 6 (2015.1.00973.S and 2015.1.00902.S), and band 7 (2013.1.00740.S) data. Data reduction and imaging are conducted with CASA ([CASA Team et al. 2022](#)) in a standard manner following [Mizukoshi et al. \(2021\)](#), except for band 3 and 4, additional spectral cubes with natural weighting are made to maximize sensitivity. The integrated 1D ALMA spectra of J0107a are shown in Figure 16a.

### 3.2.3 JWST Data

JWST observations of the VV114 field have been conducted as part of the GOALS-JWST survey ([Evans et al. 2022](#); [Linden et al. 2023](#)), with NIRCam imaging in the F150W, F200W, F356W, and F444W filters and MIRI imaging in the F560W, F770W, and F1500W filters<sup>4</sup>. We obtain images from the MAST archive and align the astrometry to GAIA DR3 ([Gaia Collaboration et al. 2016, 2023](#)). To remove the foreground emission from VV114, we first apply standard background subtraction, then identify point sources with a flux ratio  $\log(S_{F356W}/S_{F200W}) < -0.05$  as bright stars in VV114 and subtract them using the point spread

<sup>4</sup>The JWST data presented here were obtained from the Mikulski Archive for Space Telescopes (MAST) at the Space Telescope Science Institute. The specific observations analyzed can be accessed via DOI: [10.17909/g4k8-3922](https://doi.org/10.17909/g4k8-3922).

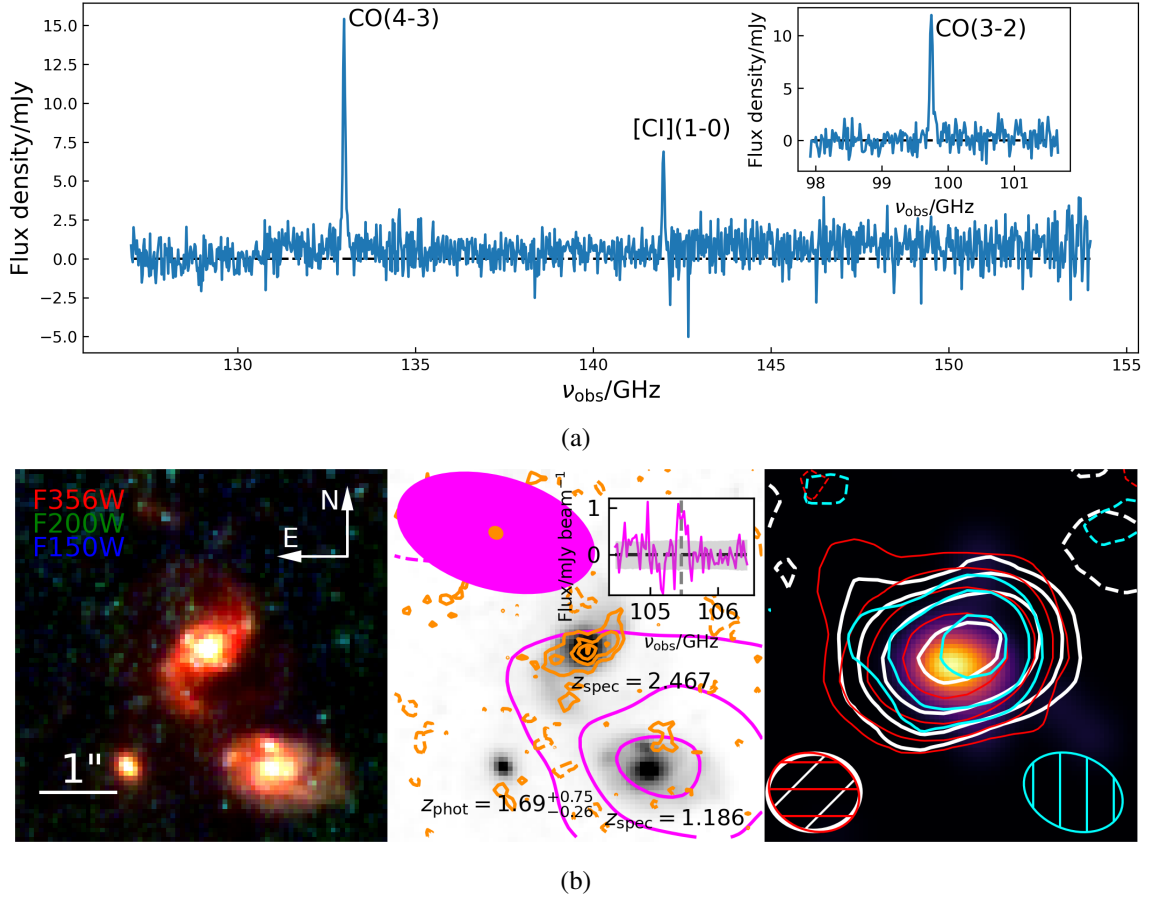


**Figure 16.** A multiwavelength view of J0107a: (a) the integrated 1D spectra of J0107a from ALMA Band 3/4 data. The channel widths are  $50 \text{ km s}^{-1}$ . (b) Left: JWST/NIRCam color composite image (red: F356W; green: F200W; blue: F150W) of J0107a. Middle: F356W image with ALMA band 7 continuum of J0107a (dark orange) and the zeroth-moment map of the band 3 emission line from the  $z = 1.186$  southwest (SW) spiral galaxy (magenta) overlaid. The insert panel shows the band 3 spectrum of the SW spiral galaxy, with the line's central frequency of 105.458 GHz marked with the gray dashed line. Right: Chandra ACIS-S 0.5-10 keV count image smoothed with a  $0''.5$  FWHM circular Gaussian kernel. Contours show the zeroth-moment maps of J0107a's emission lines, with white, red, and blue for CO(3-2), CO(4-3), and [CI](1-0), respectively. Each panel is  $5'' \times 5''$  in size. ALMA beam sizes are shown with the same colors as the contours. Contour levels are  $-2, 2, 4, 6, 8, 10 \dots \times \sigma$  in the middle panel and  $-2, 2, 4, 8, 16 \dots \times \sigma$  in the right panel.

function (PSF) model built with the WebbPSF<sup>5</sup> package before performing photometry.

<sup>5</sup><https://github.com/spacetelescope/webbpsf>

### 3.3 Analysis and Results

#### 3.3.1 JWST and ALMA Look at J0107a

The left panel of Figure 16b shows the NIRCam image of J0107a. J0107a is clearly resolved, showing a grand-design barred spiral structure with two arms and a blue central point-like source, in line with an active galactic nucleus (AGN) as indicated by its X-ray detection in Chandra ACIS-S data (Grimes et al. 2006). The bar structure is also visible in the ALMA band 7 continuum image with  $0''.18 \times 0''.15$  beam size, implying star formation in the bar (Figure 16b, the middle panel). To quantify the bar structure, we fit ellipse isophotes to the F444W image (Figure 17). The projected bar size is determined as the semimajor axis (SMA) at maximum ellipticity  $e_{\max}$ . For J0107a’s stellar bar, we find an SMA of 7.5 kpc and  $e_{\max} = 0.50$ . The  $e_{\max}$  is similar to that measured by Guo et al. (2023) for  $z > 1$  barred galaxies in the CEERS survey, but the SMA is longer. We also perform parametric modeling of the F444W image, assuming a PSF model for the AGN, three Sérsic profiles for the bar, bulge, and disk, and two logarithmic curves for the arms (Kennicutt 1981). We implement the models using the `numpy` (Harris et al. 2020), `scipy` (Virtanen et al. 2020), and `astropy` (Astropy Collaboration et al. 2018) packages, then use the `dynesty` code (Speagle 2020) to sample the joint posterior probability density function (PDF) of model parameters. The best-fit model and residual are shown in panels c and d of Figure 17, respectively. The rest-frame NIR light is dominated by the three Sérsic components with light fraction of  $11.8^{+2.3}_{-3.0}\%$ ,  $80.5^{+4.6}_{-5.0}\%$  and  $7.9^{+4.3}_{-3.5}\%$  for the AGN, sum of Sérsic components, and spiral arms, respectively.

J0107a is detected with three different molecular gas tracers, namely CO, [C I], and dust continuum. The derived  $M_{\text{mol}}$  ranges from  $(9.2 \pm 1.7) \times 10^{10} M_{\odot}$  using the CO(3-2) line to  $(3.2 \pm 1.6) \times 10^{11} M_{\odot}$  using the dust continuum, assuming SMG/ULIRG-like CO excitation and conversion factors (Mizukoshi et al. 2021). If normal star-forming galaxies-like conversions (Daddi et al. 2010b, 2015; Decarli et al. 2016) are adopted, the  $M_{\text{mol}}$  will be  $\sim 6 \times 10^{11} M_{\odot}$ . Therefore, J0107a is a very gas-rich DSFG with gas fraction  $\sim 20\text{--}60\%$ . No companion of J0107a is found in the band 3 cube. Assuming  $\alpha_{\text{CO}} = 3.6 M_{\odot}/(\text{K km s}^{-1} \text{ pc}^2)$ ,  $r_{31} = 0.42 \pm 0.07$  and a Gaussian line profile with FWHM of  $300 \text{ km s}^{-1}$ , the  $3\sigma$  sensitivity of  $1.45 \text{ mJy beam}^{-1}$  in  $50 \text{ km s}^{-1}$  channels translates to an upper limit of  $M_{\text{mol}} \lesssim 10^{11} M_{\odot}$ , implying the absence of any companion with molecular gas mass comparable with that of J0107a.

#### 3.3.2 Photometry and Spectral Energy Distribution Modeling

To derive the photometry in JWST bands, we first combine the F356W and F444W images and then run source detection routines in the `photutils` package to generate Kron apertures for J0107a and the two

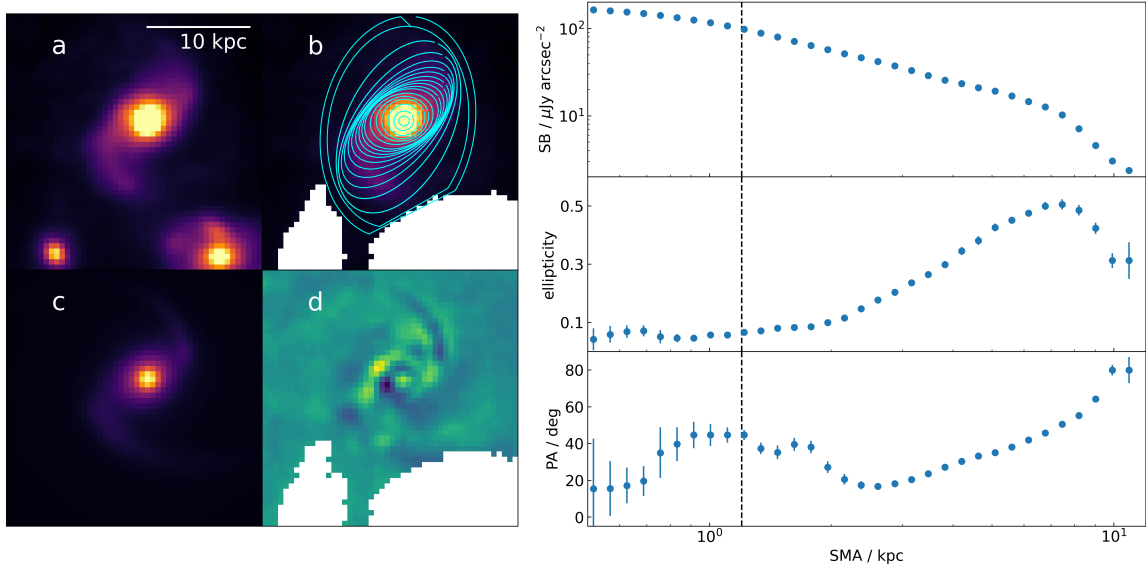


**Figure 17.** Left: a)  $3'' \times 3''$  F444W cutout of J0107a displayed in  $-2-80\sigma$  range; b) the ellipse isophote fit to J0107a (cyan); c) the best-fit 2D parametric model of J0107a; d) the residual of the best-fit model. During modeling processes, the two neighboring galaxies are masked. Right: radial surface brightness (SB, top), ellipticity (middle), and position angle (PA, bottom) distributions of J0107a. The vertical dashed line marks the spatial resolution in the F444W band.

neighboring galaxies in the combined  $5'' \times 5''$  cutout image. The fluxes are measured with the Kron apertures and corrected for aperture loss using the PSF in each band. Flux uncertainties are estimated from sky by taking the standard deviations of fluxes in 1000 apertures randomly placed at blank positions within  $5''$  radius from J0107a.

We fit the observed spectral energy distribution (SED) of J0107a using the CIGALE code (Boquien et al. 2019). In addition to the JWST data, we include ALMA band 6/7 continuum and Chandra X-ray fluxes taken from Tamura et al. (2014) and Mizukoshi et al. (2021). We assume a nonparametric star formation history (Leja et al. 2019b) and adopt Noll et al. (2009) dust attenuation laws. The AGN emission is modeled with a power-law X-ray component plus the SKIRTOR library (Stalevski et al. 2016). For dust emission, we use the Draine et al. (2014) templates. We fix the redshift of J0107a at  $z_{\text{spec}} = 2.467$  in CIGALE SED fitting.

The SED fit of J0107a is shown in the right panel of Figure 18. From SED fitting we derive the basic physical parameters of J0107a as follows:  $M_{\star} = 4.5^{+1.7}_{-1.4} \times 10^{11} M_{\odot}$ ,  $\text{SFR} = 499^{+357}_{-179} M_{\odot} \text{ yr}^{-1}$ , dust mass  $M_{\text{dust}} = 4.3^{+1.0}_{-1.0} \times 10^9 M_{\odot}$ , and rest-frame 2-10 keV luminosity of  $4.9^{+0.9}_{-0.9} \times 10^{43} \text{ erg s}^{-1}$ . The SFR of J0107a is  $0.8^{+0.9}_{-0.4}$  times of the main sequence value of star-forming galaxies with the same redshift and  $M_{\star}$  (Speagle et al. 2014).

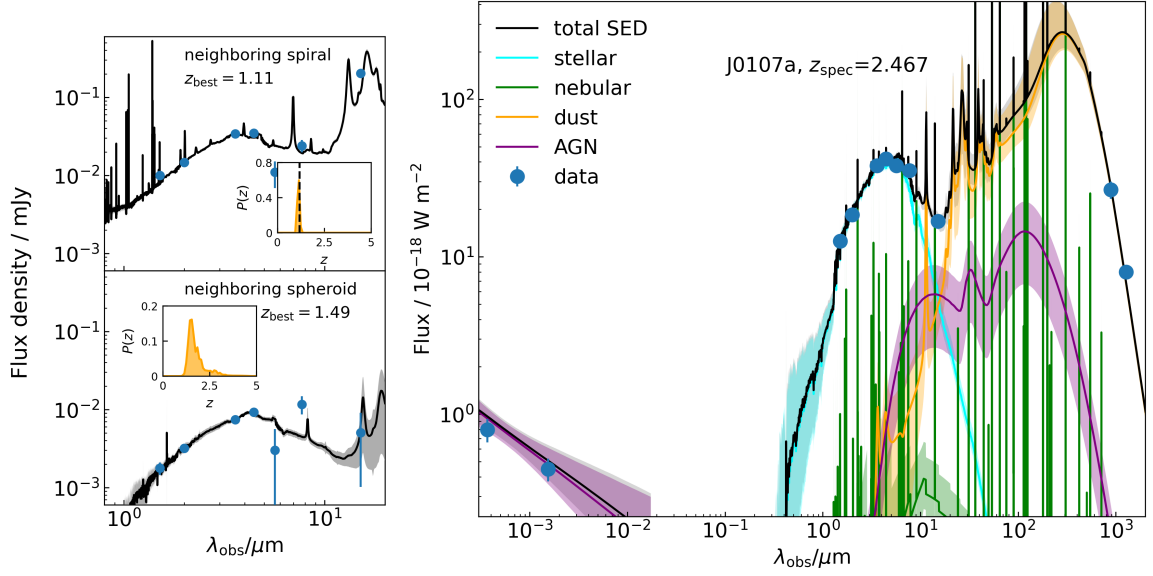


**Figure 18.** Left: EAZY fit of the JWST photometry (black circles and error bars). The median and 16th-84th percentile ranges of the SED at the best-fit redshift  $z_{\text{best}}$  are shown with the solid lines and shaded regions, respectively. The insert panels show the PDFs of photometric redshift. The photometric redshifts discussed in Section 3.3.3 are 16th-50th-84th percentile values of the PDF. The vertical dashed lines mark the spectroscopic redshift identification. Right: X-ray-to-millimeter SED fit of J0107a at  $z_{\text{spec}} = 2.467$ . For the total SED model and individual components, we show median and 16th-84th percentile ranges with the solid lines and shaded regions, respectively.

### 3.3.3 Properties of the Two Neighboring galaxies and Association with J0107a

Two neighboring galaxies are visible within  $2''.5$  from J0107a. The spiral galaxy  $1''.7$  southwest of J0107a exhibits a single-peaked redshift PDF (Figure 18, the top-left panel). This PDF, derived from the SED fit of the JWST photometry using the EAZY<sup>6</sup> (Brammer et al. 2008) code, yields a photometric redshift of  $z_{\text{phot}} = 1.12^{+0.05}_{-0.03}$ . An emission line at the central frequency of 105.458 GHz is detected at the position of the southwest spiral galaxy in the ALMA band 3 spectral cube (Figure 16b, the middle panel), with the direction of velocity gradient aligning with the NIR major axis. Therefore, we are able to identify the emission line as redshifted CO(2-1) and derive spectroscopic redshift  $z_{\text{spec}} = 1.186$  for this galaxy. Using the SED fitting method in Section 3.3.2, we derive  $M_{\star} = 5.0^{+1.4}_{-1.4} \times 10^{10} M_{\odot}$  and  $\text{SFR} = 43^{+16}_{-11} M_{\odot} \text{ yr}^{-1}$ . The SFR of this spiral galaxies is  $1.1^{+0.6}_{-0.3} \times$  the MS value at the same redshift and  $M_{\star}$ . The neighboring spheroid galaxy  $1''.6$  southeast to J0107a has  $z_{\text{phot}} = 1.69^{+0.75}_{-0.26}$  from the redshift PDF (Figure 18, the bottom-left panel) and no line or continuum detection in the ALMA data, so its relation with J0107a remains uncertain. If this

<sup>6</sup><https://github.com/gbrammer/eaazy-py>

spheroid galaxy is at the same redshift of J0107a, the  $M_*$  and SFR derived from SED fit of the JWST data will be  $6.9_{-1.3}^{+1.2} \times 10^{10} M_\odot$  and  $4_{-4}^{+18} M_\odot \text{ yr}^{-1}$ , respectively, and the stellar mass ratio of 1:6 does not satisfy the definition of a major merger.

### 3.3.4 Dynamical Modeling

A clear velocity gradient is seen in the velocity fields of all three spectral lines (Figure 19, see also Mizukoshi et al. (2021)). We choose CO(4-3) to perform kinematic modeling because it has the highest S/N. We create a  $9''.3 \times 9''.3$  cutout cube centered at J0107a with  $20 \text{ km s}^{-1}$  channel width and model the data with the GalPak3D code (Bouché et al. 2015), assuming an exponential disk profile and arctan rotation curve. This gives an inclination of  $9.7^\circ \pm 0.8^\circ$ , half-light radius  $r_e = 0''.54 \pm 0''.01$ , maximum rotation velocity  $v_{\text{MAX}} = 281 \pm 39 \text{ km s}^{-1}$ , and intrinsic velocity dispersion  $\sigma = 35 \pm 3 \text{ km s}^{-1}$ . In addition, we fit the data with the 3D-Barolo code (Di Teodoro & Fraternali 2015) and find consistent values of an inclination of  $10.4^\circ$ , maximum rotation velocity of  $283 \text{ km s}^{-1}$  and intrinsic velocity dispersion of  $31 \text{ km s}^{-1}$ . The best-fit models and residual maps are shown in Figure 19. These results show J0107a has a dynamically cold gas disk with  $v_{\text{MAX}}/\sigma \sim 8$ .

The dynamical mass within a radius of  $2.2r_e = 9.8 \text{ kpc}$  at  $z = 2.467$  can be calculated as:

$$M_{\text{dyn}} = \frac{2.2r_e v_{\text{circ}}^2}{G} \quad (7)$$

where  $G$  is the gravitational constant and  $v_{\text{circ}} = \sqrt{v_{\text{MAX}}^2 + 4.4\sigma^2}$  is the circularized velocity (Burkert et al. 2010) computed using the results from GalPak3D modelling. The resulting  $M_{\text{dyn}}$  of  $\sim 2 \times 10^{11} M_\odot$  is less than the sum of  $M_*$  and  $M_{\text{mol}}$ , indicating the total mass within a radius of  $10 \text{ kpc}$  is dominated by baryon.

Previous analysis in Mizukoshi et al. (2021) reported a dynamical mass of  $\sim 10^{10} M_\odot$  based on similar velocity dispersion but a much lower  $v_{\text{MAX}} = 69 \text{ km s}^{-1}$ , and their  $M_{\text{dyn}}$  conflicts with  $M_*$  and  $M_{\text{mol}}$ , mainly because of their initial guess of inclination of  $60^\circ$ . We have tested initial guesses of  $10^\circ$ ,  $30^\circ$ , and  $60^\circ$ , and let the value vary from  $0^\circ$  to  $90^\circ$ . For initial guesses of  $10^\circ$ ,  $30^\circ$ , the fit converges to the same results presented above, while for the initial guess of  $60^\circ$ , the fit converges to  $\sim 60^\circ$ . Apparently, the inclination cannot be constrained alone with the  $1''.2$  resolution CO data even the peak S/N reaches  $\sim 50$ , and the new low inclination solution seems more appropriate. The outermost isophote of J0107a has an ellipticity of  $\sim 0.3$  which translates to an inclination of  $< 45^\circ$ . The inclination from isophote fitting should be treated as an upper limit because of distortion of the isophotes by strong spiral arms (Yu & Ho 2020) and insufficient depth of the F444W image to detect the underlying smooth stellar disk. We caution that the current  $M_{\text{dyn}}$  estimate can

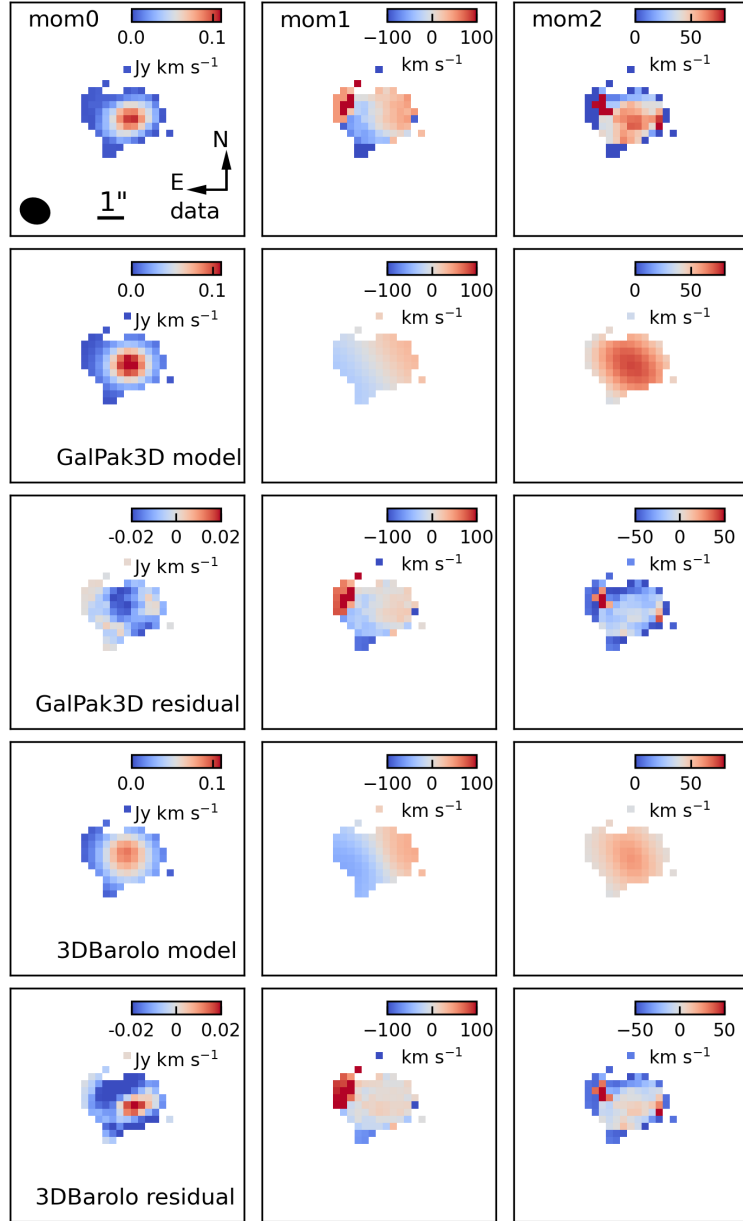


**Figure 19.** The zeroth, first, and second moment maps of the CO(4-3) emission line of J0107a. Also shown are the GalPak3D/3D-Barolo models and corresponding residual maps. The black ellipse in the top left panel indicates the beam size. The residual in the first moment map with redshifted velocity on the northeast edge overlaps with a horn-like structure in the zeroth moment map (Figure 16b, the right panel) and may originate from gas inflow. However, the S/N is low so further observation is needed to confirm it.



still have large uncertainty due to the low inclination, beam smearing effect, and a possible more complex rotation pattern due to the bar. Future high-resolution CO observations are needed to better constrain the dynamics and mass distribution.

### 3.4 Discussion and Conclusion: An Ultramassive Barred Spiral Galaxy at $z = 2.467$ and the Implications

A bright DSFG with a flux density of  $\sim 8$  mJy at the observed wavelength of  $888 \mu\text{m}$  is expected to be the product of a gas-rich major merger according to the conventional wisdom. Nonetheless, J0107a’s symmetric barred spiral morphology, lack of massive and gas-rich companion, and large dynamically cold gas disk all support a non-merger origin. Instead of merger-induced starburst, a more plausible formation channel would be cold mode accretion via inflowing gas streams from the cosmic web which penetrate the hot medium in the host halo and reach the central galaxy to fuel star formation and AGN activity (e.g., Kereš et al. 2009). Assuming the stellar-to-halo mass ratio  $\log(M_\star/M_{\text{halo}})$  ranges from  $-1.5$  dex to  $-1.8$  dex (Stach et al. 2021), J0107a has a halo mass of  $M_{\text{halo}} = (1-3) \times 10^{13} M_\odot$ , which lies at the boundary between hot and cold in hot modes of accretion (Dekel & Birnboim 2006) and represents the most efficient normal star-forming galaxy in converting gas into stars at this redshift. The predicted baryon accretion rate is  $1500-5400 M_\odot \text{ yr}^{-1}$  (Dekel et al. 2009), which is sufficient to supply J0107a’s star formation. If J0107a is indeed fed by such streams, it will be an extreme case with the maximum allowed accretion rate, thus an ideal target to directly detect such streams onto a bright DSFG and demonstrate their heterogeneous origins.

The large stellar bar of J0107a is of particular interest in the context of galaxy assembly. J0107a has the highest redshift among known  $z > 1$  galaxies with a clear stellar bar identified (e.g., Simmons et al. 2014; Guo et al. 2023), but also see a lensed case at  $z = 4.26$  (Smail et al. 2023) and potential gas/dust bars at  $z = 1.5-4.4$  (Hodge et al. 2019; Tsukui et al. 2023). In local strongly barred galaxies, the global SFR is suppressed compared to unbarred spiral galaxies with similar mass (e.g., Gavazzi et al. 2015; Géron et al. 2021), while J0107a lies above the  $z \sim 2.5$  star-forming main sequence. This may be interpreted as the bar-accelerated stellar mass build-up in the past (e.g., Kim et al. 2017; Fraser-McKelvie et al. 2020) due to the effective gas redistribution as we will discuss below, and J0107a is caught in the early starburst phase of a massive barred galaxy.

In addition to the stellar bar, the  $888 \mu\text{m}$  dust continuum map suggests the presence of a dust/gas bar (Figure 16b, the middle panel), which is the site of star formation. The dust emission shows three peaks and is reminiscent of the enhancement of SFR at the galactic center and the bar ends in local barred galaxies (Maeda et al. 2023). Elevated central star formation is common in local barred galaxies (e.g., Chown et al.

2019; Lin et al. 2020) and explained by theoretical studies as a consequence of gas being funneled by the bar toward the center and feeds the star formation and supermassive black hole (e.g., Carles et al. 2016). The higher central molecular gas concentration observed in local barred spiral galaxies (Kuno et al. 2007; Yu et al. 2022b) provides direct evidence for bar-driven gas inflow, and Yu et al. (2022b) also suggest the spiral arms can be playing a role in transporting gas to the center. On the other hand, barred galaxies with suppressed central SFR often exhibit weak to nearly vanished spiral arms (Wang et al. 2020; Yu et al. 2022a). J0107a possesses a strong stellar bar and pronounced spiral arms, and the high SFR may be triggered by gas inflow driven by stellar structures in its gas-rich disk.

Numerical simulations have shown that an isolated baryon-dominated and dynamically cold disk allows bar formation at early times (Rosas-Guevara et al. 2022; Bland-Hawthorn et al. 2023), though it has also been suggested that a high gas fraction can weaken the bar and slows down its formation (e.g., Athanassoula et al. 2013). Alternative formation channels of barred spiral structures include interaction with a companion galaxy (e.g., Elmegreen et al. 1990; Oh et al. 2008). The photometric redshift of the southeast spheroid galaxy does not exclude the possibility of it being a companion of J0107a. From the analysis of the JWST data, the spheroid galaxy will have  $M_*$  of  $\sim 1/6 \times$  J0107a and a distance of 13 kpc to J0107a if it is at  $z = 2.467$ , which is sufficient to affect J0107a's disk. While the southeast spiral arm indeed seems brighter, tidal features were not found. Furthermore, J0107a's CO disk is dynamically cold and dominated by ordered rotation ( $V_{\text{max}}/\sigma \sim 8$ ). Considering that cold accretion can also bring a low  $V_{\text{max}}/\sigma$  component (Ho 2007), secular bar formation is thus favored and consistent with the first massive and well-ordered disks emerging in the cosmic noon (Simons et al. 2017).

Previous simulations of bar formation have neither covered the parameter space with  $M_*$ , SFR, and gas fraction as high as J0107a, nor gas accretion from the surrounding environment. Refined simulations reproducing the properties of J0107a are needed to understand the formation mechanisms of stellar and gas bars in the earliest massive disks. In terms of observations, deep high-resolution spectroscopy is needed to confirm the isolated disk nature of J0107a and to investigate the interplay between bar, gas, and star formation.

Finally, J0107a has been mis-identified as a strongly lensed SMG magnified by approximately ten times in Mizukoshi et al. (2021) to explain the bright CO(4-3) emission with narrow line FWHM (FWHM =  $193 \pm 11$  km s<sup>-1</sup>;  $S\Delta v = 3.0 \pm 0.2$  Jy km s<sup>-1</sup>). However, it is now clear that this is caused by a low inclination of  $\sim 10^\circ$ , as the regular morphology and absence of a nearby massive source can rule out strong gravitational lensing effect. While the empirical relation between CO line FWHM and velocity-integrated intensity (e.g., Harris et al. 2012; Bothwell et al. 2013) is a natural consequence of the virial theorem for large samples of unlensed galaxies, the use of such relations to identify individual lensed source should be careful as the result

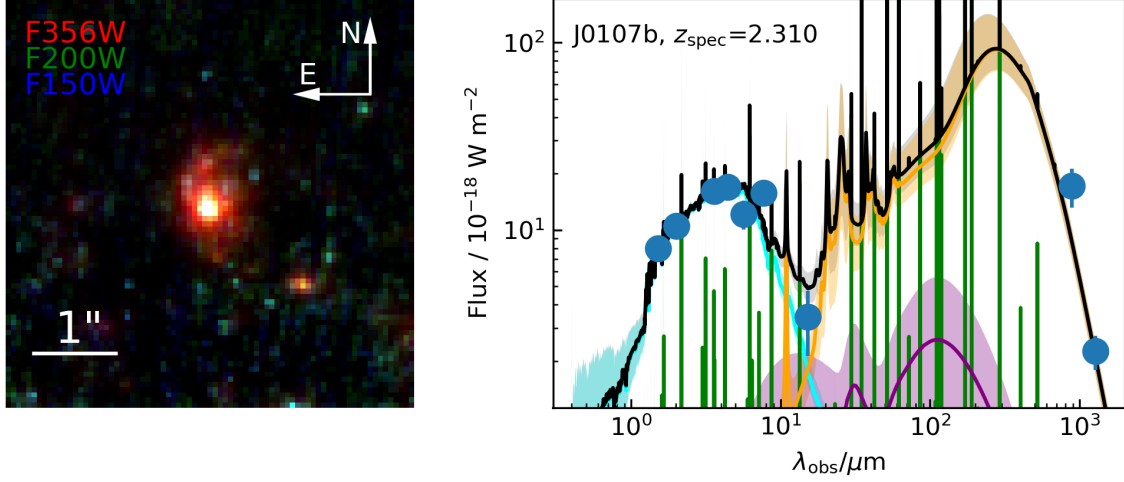


**Figure 20.** Left:  $5'' \times 5''$  JWST/NIRCam color composite image (red: F356W; green: F200W; blue: F150W) of J0107b; Right: SED fit of J0107b, symbols are the same as Figure 18.

is sensitive to the unknown inclination.

### 3.5 A Quick Glimpse of J0107b at $z = 2.310$

With the same method as J0107a, we also perform SED analysis of another blindly detected CO line source in the VV114 field, ALMA J010747.0-173010 (J0107b) at  $z = 2.310$ . The SED fit is shown in the right panel of Figure 20. From the fit we derive  $M_\star = 1.6^{+0.5}_{-0.5} \times 10^{11} M_\odot$ ,  $\text{SFR} = 144^{+93}_{-55} M_\odot \text{ yr}^{-1}$ , and dust mass of  $M_{\text{dust}} = 1.4^{+0.4}_{-0.4} \times 10^9 M_\odot$ . The SFR is  $0.6^{+0.6}_{-0.3} \times$  of the main sequence value at  $z = 2.310$  (Speagle et al. 2014).

Based on our new CO(1-0) observation (see Section 3.6.1), we derive updated molecular gas masses of  $M_{\text{mol}} = (2.9 \pm 0.4) \times 10^{11} M_\odot$  for J0107a and  $M_{\text{mol}} = (1.9 \pm 0.5) \times 10^{11} M_\odot$  for J0107b, assuming  $\alpha_{\text{CO}} = 3.6 M_\odot / (\text{K km s}^{-1} \text{ pc}^2)$ . The resulting gas depletion time scale of J0107a is  $\sim 43\%$  of J0107b, despite their similar position relative to the main sequence. Compared to J0107a, J0107b is a normal spiral galaxy (the left panel of Figure 20) without an X-ray AGN, and the faster gas consumption in J0107a can be explained by the effect of its strong stellar bar, as we have discussed in section 3.4.

### 3.6 Follow-up Observations of J0107a in the VV114 Field

#### 3.6.1 VLA Semester 2023B Follow-up Observation

To mitigate the uncertainties in molecular gas mass due to assumptions on excitation, we have conducted Karl G. Jansky Very Large Array (VLA) follow-up observation of J0107a to detect the CO(1-0) transition (project code VLA/23B-024, PI: Shuo Huang) on 2023 Nov 13. We use the Ka-band receiver and 8-bit sampler in D-array configuration. The WIDAR<sup>7</sup> correlator is configured to place two basebands centered at the sky frequency of 33.19 GHz and 34.88 GHz to cover the redshifted CO(1-0) emission lines from J0107a and J0107b. The subbands containing CO(1-0) emission lines were set to have 1 MHz channel widths, while the remaining channels have channel widths of 2 MHz. We observed 3C48 to calibrate bandpass and absolute flux scale. J0116-1136 was observed as phase calibrator. The on-source integration time was 1.68 hr.

The data were reduced using the standard VLA pipeline in the CASA package. Spectral cube was generated using the `tclean` task with Briggs weighting (`robust`= 0.5) and 30 km s<sup>-1</sup> channel width. The channel maps were cleaned down to 1 $\sigma$  noise level, resulting in a beam size of 2''.9  $\times$  1''.8 with a PA of 1° and an RMS noise of 0.14 mJy beam<sup>-1</sup> before primary beam correction.

The CO(1-0) emission line from J0107a is detected at a peak S/N of 7 in the channel maps. In addition, the CO(1-0) line of J0107b is detected at a peak S/N of  $\sim 5$ . The velocity-integrated line intensity maps and CO(1-0) spectra are shown in the left and right columns of Figure 21, respectively. From these maps, we measure velocity-integrated CO(1-0) line intensities of  $I'_{\text{CO}(1-0), \text{J0107a}} = 0.27 \pm 0.04 \text{ Jy km s}^{-1}$  for J0107a and  $I'_{\text{CO}(1-0), \text{J0107b}} = 0.20 \pm 0.05 \text{ Jy km s}^{-1}$  for J0107b.

#### 3.6.2 Total Molecular Gas Mass and Excitation of J0107a/J0107b

The detection of CO(1-0) line eliminates uncertainties in  $M_{\text{mol}}$  introduced by assuming a CO line ratio (e.g.,  $r_{31}$  or  $r_{41}$  in Section 3.3). However, a  $\sim 2\times$  error still exists if  $\alpha_{\text{CO}}$  is unknown. To constrain  $\alpha_{\text{CO}}$ , we perform CO spectral line energy distribution (SLED) modeling using the non-local thermal equilibrium radiative transfer code RADEX (van der Tak et al. 2007) assuming the large velocity gradient (LVG) approximation, from which we can infer the number density of hydrogen molecules and then use it to calculate  $\alpha_{\text{CO}}$ . The background temperature is set to the cosmic microwave background (CMB) temperature as  $(1+z) \times 2.7315$  K. There are three free parameters: kinematic temperature  $T_{\text{kin}}$ , number density of hydrogen molecules  $n_{\text{H}_2}$ , and column density of CO molecules  $N_{\text{CO}}$ . The parameter ranges are  $20 \text{ K} < T_{\text{kin}} < 300 \text{ K}$ ,  $10 \text{ cm}^{-3} < n_{\text{H}_2} < 10^7 \text{ cm}^{-3}$ , and  $10^{15} \text{ cm}^{-2} < N_{\text{CO}} < 10^{20} \text{ cm}^{-2}$ , evenly placed in a logarithmic grid. The

<sup>7</sup> Acronym for Wideband Interferometric Digital ARchitecture (Perley et al. 2011).

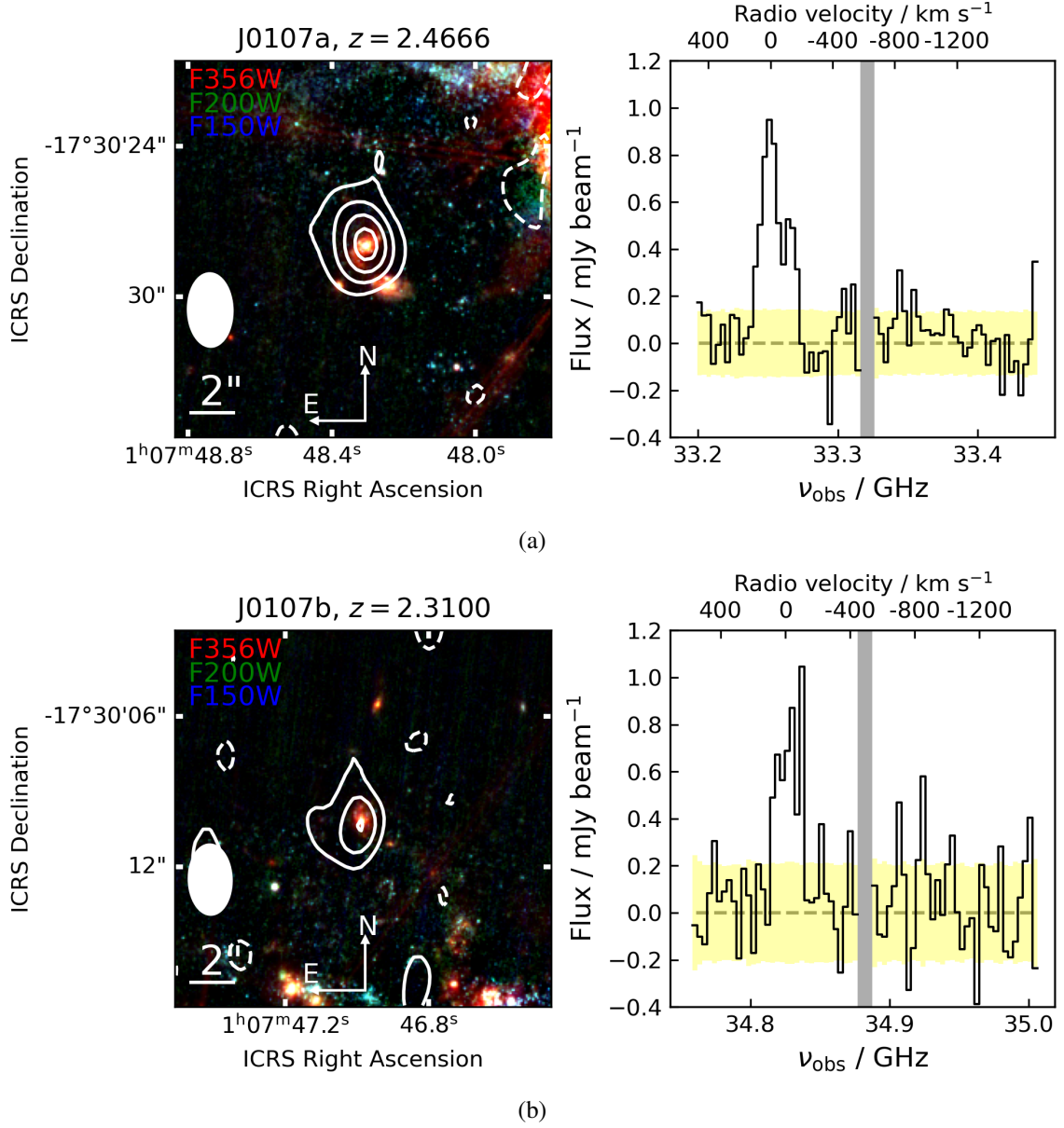


**Figure 21.** Left:  $15'' \times 15''$  JWST/NIRCam color composite image (red: F356W; green: F200W; blue: F150W) with CO(1-0) zeroth moment map overlaid as white contours. The white ellipses indicate beam size. Contour levels are  $-2, 2, 4, 6, 8 \dots \times \sigma$ ; Right: CO(1-0) spectra at the source centers with channel widths of  $30 \text{ km s}^{-1}$ . The gray stripes are band gaps. The yellow regions indicate the RMS noise levels. Panels (a) and (b) show data of J0107a and J0107b, respectively.

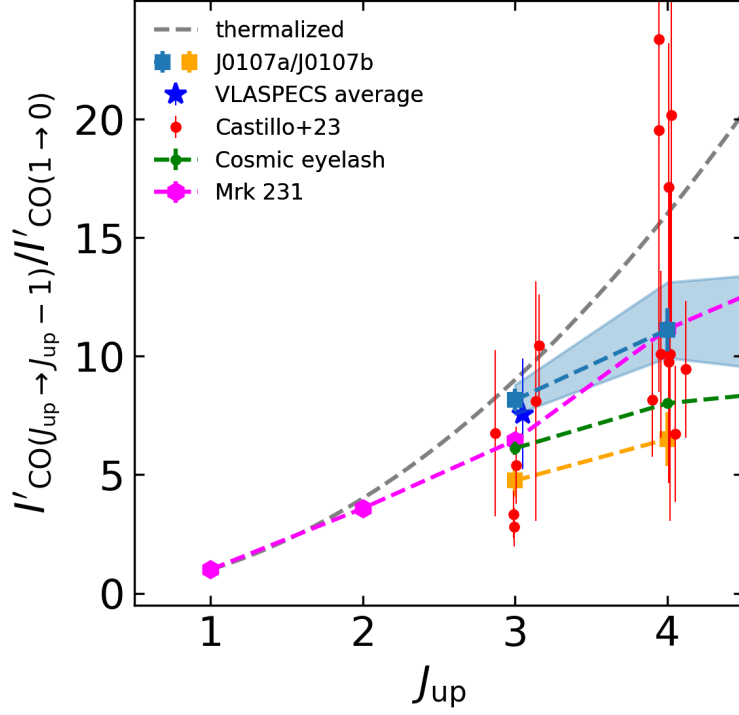


**Figure 22.** CO SLED of J0107a/J0107b. The 16th–84th percentile range of the RADEX fit is shown as the shaded region. For comparison we show literature samples of bright SMGs ( $S_{850\mu\text{m}} > 7.5$  mJy, [Frias Castillo et al. 2023](#)); average of  $z \sim 2.5$  MS star-forming galaxies (VLASPECS, [Riechers et al. 2020](#)); a  $z = 2.3259$  lensed SMG (the cosmic eyelash, [Danielson et al. 2011](#)); a local QSO (Mrk 231, [Papadopoulos et al. 2007](#)). The thermalized CO SLED ( $r_{J1} = 1$ ) is shown as the gray dashed line. Note that  $r_{J1} \times J^2 = I'_{\text{CO}(J \rightarrow J-1)} / I'_{\text{CO}(1 \rightarrow 0)}$ . For the purpose of visualization, the literature samples are shifted along the  $J_{\text{up}}$  axis.

likelihood of each parameter combination is calculated in a Bayesian manner.

By fitting the  $J = (1 - 0), (3 - 2), (4 - 3)$  transitions, we derive  $n_{\text{H}_2} = 0.8^{+2.2}_{-0.6} \times 10^3 \text{ cm}^{-3}$  for J0107a. Under LVG approximation,  $\alpha_{\text{CO}}$  is given by ([Papadopoulos et al. 2012](#)):

$$\alpha_{\text{CO}} = 2.65 \frac{\sqrt{n_{\text{H}_2}}}{T_{b,\text{CO}(1-0)} \text{ cm}^{-3/2}} \frac{\text{K}}{\text{K km s}^{-1} \text{ pc}^{-2}}, \quad (8)$$

where  $T_{b,\text{CO}(1-0)}$  is the brightness temperature of the CO(1-0) emission line. Since the VLA beam size is much larger than the actual source size, we correct the brightness temperature using the source area measured from the ALMA 1.3 mm continuum image, which has the best S/N and spatial resolution among available data. After correcting for redshift, we find  $T_{b,\text{CO}(1-0)} = 16.6 \text{ K}$  and  $\alpha_{\text{CO}} = 2.3^{+1.8}_{-1.3} M_{\odot} / (\text{K km s}^{-1} \text{ pc}^2)$ .

We note that (1) at high redshifts, the higher CMB temperature may lead to loss of contrast and reduce the observed CO(1-0) line fluxes (da Cunha et al. 2013), and this effect has not been corrected here; (2) the LVG approximation may not be valid for our target and the CO SLED is poorly sampled, so the derived  $n_{\text{H}_2}$  can be wrong. For J0107b, the RADEX fit did not converge. On a best-effort basis, we conclude that the conventional  $\alpha_{\text{CO}} = 3.6 M_{\odot} / (\text{K km s}^{-1} \text{ pc}^2)$  seems appropriate for J0107a/J0107b, and the updated  $M_{\text{mol}}$  estimates are already presented in Section 3.5.

In Figure 22 we plot the CO SLED of J0107a/J0107b and  $z > 2$  galaxies with CO(1-0) detection from literature. Our two targets have  $r_{31}$  and  $r_{41}$  values within the range spanned by the literature samples. The CO excitation of J0107a is similar to other bright SMGs (Frias Castillo et al. 2023), and the  $I'_{\text{CO}(3-2)} / I'_{\text{CO}(1-0)}$  value is close to average  $z \sim 2.5$  MS galaxies (Riechers et al. 2020). On the other hand, the molecular gas excitation in J0107b is much lower, lying on the lower end of literature values. This can be explained by less extreme star formation activity and the absence of a luminous AGN in J0107b. From the observed  $r_{31}$  between 0.79–1.10, Riechers et al. (2020) suggest that CO(3-2)-based gas mass of  $z = 2-3$  MS galaxies assuming  $r_{31} = 0.42 \pm 0.07$  in  $z \sim 1.5$  MS galaxies (Daddi et al. 2015) should be revised down by a factor of  $\approx 2$ . Here we show that  $r_{31}$  is diverse even for bright SMGs at  $z > 2$ . For a reliable  $M_{\text{mol}}$  estimate, CO(1-0) or alternative tracer (e.g., [C I](1-0) or dust continuum) is ultimately required.

### 3.6.3 ALMA Cycle 10 Follow-up Observations

In response to the need for high-resolution data raised in Section 3.4, we conduct follow-up observations of the CO(4-3) and [C I](1-0) lines using ALMA (project code 2023.1.01262.S, PI: Shuo Huang). We request a spatial resolution of  $0''.15$  and RMS sensitivity of  $0.15 \text{ mJy beam}^{-1}$  in  $20 \text{ km s}^{-1}$  channels to spatially resolve the velocity field and search for dynamical signatures of bar-driven gas inflow toward the starburst core. The correlator is tuned to cover the redshifted CO(4-3), [C I](1-0), and HNC(5-4) emission lines simultaneously, plus a continuum spectral window covering sky frequency 142.42–144.29 GHz. Additional observation in C-4 configuration with  $0''.6$  resolution will be used to recover the extended components.

At the time of writing this thesis, the long baseline part of ALMA observation is finished and waiting for quality assurance (QA). Due to ALMA transporter troubles, the first round of observations was executed in C-8 configuration with  $0''.1$  resolution. Unfortunately, the observations were affected by correlator issues and failed, only leaving usable continuum data. Then the target was re-observed in C-7 configuration with an on-source integration time of 3.36 hr. The continuum data with  $\sim 0''.1$  beam size, totaling an on-source integration time of 6.78 hr, reaches an RMS sensitivity of  $\sim 10 \mu\text{Jy beam}^{-1}$ . From the QA0+ report (Figure 23) we can see that the bar structure is clearly resolved.



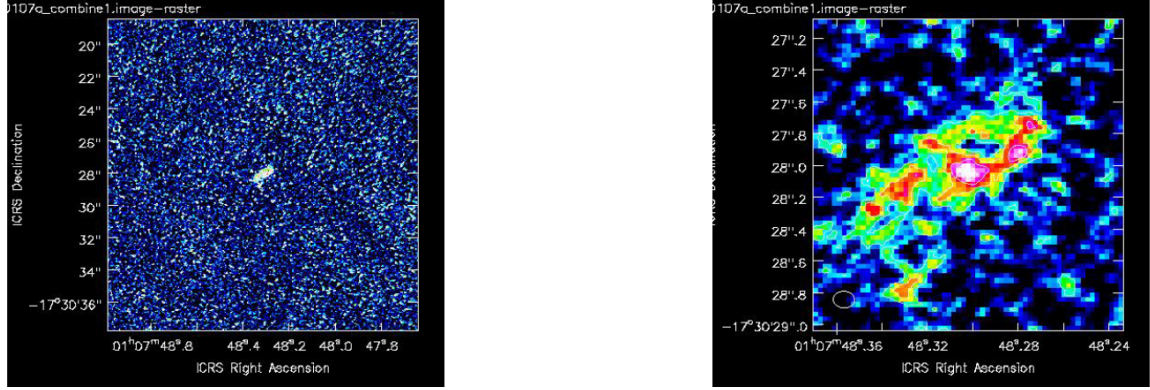


**Figure 23.** Left: High-resolution 2 mm continuum image from the ALMA follow-up observation of J0107a at  $z = 2.467$ . Right: Zoom-in image of the target. The cold dust is located on the leading side of the rotating bar (see Figure 16 and 17), which is strikingly similar to local barred spiral galaxies (e.g., NGC 1300). This similarity may indicate massive disk galaxies have already matured structure when they are still in actively star-forming phase at cosmic noon. The images are from ALMA QA0 reports and may be contaminated by emission lines.

The ALMA follow-up observations will enable an unprecedented close view of the interplay among the bar, gas disk, dusty starburst, and AGN. We list our goals as follows.

(1) measuring the gas distribution: We will obtain  $M_{\text{mol}}$  distribution traced by CO(4-3) and [C I](1-0) and SFR distribution from 2 mm continuum. Combining  $M_{\text{mol}}$  and SFR maps, we can study the resolved Kennicutt-Schmidt relation and quantify how much the dusty starburst can contribute to bar formation in a DSFG.

(2) resolving the gas motion: We will determine how the bar affects gas motion and star formation, especially whether there is gas inflow along the bar that feeds the dusty starburst, or perturbation from a possible companion. By measuring the rotation curve, we can derive the radial mass distribution and dark matter fraction to determine whether a massive and high-SFR DSFG like J0107a can fit into the cold stream scenario. Because of the tight margin between dynamical and baryon masses, this can also help constrain the  $\alpha_{\text{CO}}$ .

(3) direct search of cold stream: Emonts et al. (2023) have detected a stream with an inflow rate of  $\sim 450 M_{\odot} \text{ yr}^{-1}$  onto a  $z = 3.792$  radio galaxy using [C I](1-0) line, and the flux is  $\sim 0.5\text{--}0.6$  mJy in  $14.5 \text{ km s}^{-1}$  channels. If a similar stream feeds J0107a's star formation, its end might be detected by our observation as J0107a has a lower redshift. In the previous study, the relationships between the stream and its destination's dynamics and morphology were not explored. With our high-resolution data, we can study how a massive disk galaxy is built by star formation induced by cold streams.



## 4 Concluding Remarks and Future Prospects

With the aim to extend blind CO line surveys of high-redshift galaxies without asking for new expensive ALMA observations, we exploit archival spectral scan data and search for off-center emission lines in them. As a pilot study, we present a multiwavelength analysis of five massive galaxies discovered by their detections of millimeter emission lines in two different fields. We employ both photometric and spectroscopic data from X-ray to radio wavelengths to characterize their physical properties. This approach effectively expands the emission line sample and enables a better understanding of the nature of gas mass-selected galaxies in the distant universe.

In Section 2, we have performed a blind line search using the ALMA Band 3 spectral scan observation of the bright SMG SSA22-AzTEC26 covering sky frequency range 84.5–113.7 GHz. Using photometric redshift, we managed to derive redshift solution for three out of four emission line sources. The ALMA Band 3 line detections presented in this thesis are all CO rotational transitions originating from massive galaxies in the distant universe ( $z > 1$ ). When combined with two  $z \sim 2.4$  galaxies from shallower ALMA data of the VV114 field (Section 3), 4/5 of them are on the MS. The molecular gas mass and depletion timescales are in agreement with the scaling relation established by large targeted CO line surveys (e.g., PHIBSS1/2, Genzel et al. 2015; Tacconi et al. 2018). The source selection of targeted CO line surveys is often based on stellar mass and SFR derived from optical and NIR data, and sometimes limited to high SFR objects above the MS (hence expected to be more gas-rich) to ensure detection. Then, the results must be extrapolated to draw conclusions about more numerous galaxies on the MS. While depends on exact molecular gas properties such as temperature and spatial distribution, a flux-limited CO emission line sample mainly selects galaxies on their molecular gas mass and redshift (for an example of the selection function, see the Figure 4 of Pavesi et al. 2018). The lower average gas fraction in galaxies with blind CO(2-1) detections and consistency with scaling relations mean that our current knowledge about the gas-regulated assembly history of massive galaxies up to  $z = 2-3$  is, in general, correct, though the star-forming population has not been fully observed. On the other hand, we have found a possible quenched but yet gas-rich galaxy, which will neither be selected by CO survey of star-forming galaxies due to its low SFR, nor by that of passive galaxies because it is dusty and outside the quiescent region of classical color-color diagrams. This suggests that targeted surveys with a priori selection are indeed missing CO-emitting galaxies, and such galaxies may have important implications for galaxy evolution.

For the VV114 field, the blind search on the ALMA spectral scan data did not add new detection to the two galaxies identified manually by previous studies. Instead, we take advantage of the new JWST imaging

data to investigate the structure of galaxies discovered by line search in Section 3. We mainly focus on the brighter one, J0107a, and identify a prominent stellar bar and dynamically cold gas disk in this dusty star-forming galaxy, strongly suggesting its high SFR is caused by internal processes in a secular way, contrary to the common major merger scenario for explanation of starburst in bright SMGs. Such results could not have been obtained without JWST imaging data. With only galaxy-integrated physical properties from SED modeling of photometric data points, it is non-trivial to infer triggering mechanisms related to the structure of a single galaxy. This highlights the importance of high spatial resolution and millimeter spectroscopy in galaxy evolution studies. In addition, it also showcases the power of the synergy between JWST and ALMA in revealing the nature of high-redshift galaxies.

The bar structure in the bright DSFG J0107a has attracted great interest for follow-up observations. We have obtained CO(1-0) data using VLA Ka-band observation, and are conducting ALMA high-resolution observation to resolve this galaxy in both spatial and spectral dimensions. The preliminary results are encouraging, showing that we are starting to unveil the secrets about the stellar bar and gas disk in this ultramassive disk at  $z = 2.467$ . In addition, the gas-rich quiescent galaxy candidate in Section 2.5.2 may also be worth follow-up observations.

From the analysis of CO line emitters in the SSA22-AzTEC26 and VV114 fields, we demonstrate that targeted spectral scan observations at mm wavelengths can be used with the intent of blind CO line survey once the original target is masked. The two fields differ in depth, with the two galaxies detected in the VV114 field more gas-rich than all three galaxies detected in the SSA22-AzTEC26 field. Regardless of the difference in depth and sky position, we find consistency with the gas scaling relations for star-forming galaxies. This confirms the results of previous studies and the possibility of carrying out blind surveys in much larger sky regions by mining the ALMA archive. The discovery of a gas-rich quiescence galaxy candidate in the SSA22-AzTEC26 field and a barred spiral SMG in the VV114 field prove such surveys will be fruitful. Finally, next-generation wideband imaging spectrometers (e.g., Endo et al. 2019) on large single dish millimeter telescopes (Hughes et al. 2010; Kawabe 2018; Klaassen et al. 2020) will dramatically improve the efficiency of mm emission line surveys for high-redshift galaxies. We expect mm/submm emission line surveys will play a vital role in galaxy evolution studies of the next decades.

## 5 Bibliography

- Aihara, H., Armstrong, R., Bickerton, S., et al. 2018, PASJ, 70, S8, doi: [10.1093/pasj/psx081](https://doi.org/10.1093/pasj/psx081)
- Aird, J., Nandra, K., Laird, E. S., et al. 2010, MNRAS, 401, 2531, doi: [10.1111/j.1365-2966.2009.15829.x](https://doi.org/10.1111/j.1365-2966.2009.15829.x)
- Ao, Y., Matsuda, Y., Henkel, C., et al. 2017, ApJ, 850, 178, doi: [10.3847/1538-4357/aa960f](https://doi.org/10.3847/1538-4357/aa960f)
- Aravena, M., Decarli, R., González-López, J., et al. 2019, ApJ, 882, 136, doi: [10.3847/1538-4357/ab30df](https://doi.org/10.3847/1538-4357/ab30df)
- Astropy Collaboration, Price-Whelan, A. M., Sipőcz, B. M., et al. 2018, AJ, 156, 123, doi: [10.3847/1538-3881/aabc4f](https://doi.org/10.3847/1538-3881/aabc4f)
- Athanassoula, E., Machado, R. E. G., & Rodionov, S. A. 2013, MNRAS, 429, 1949, doi: [10.1093/mnras/sts452](https://doi.org/10.1093/mnras/sts452)
- Baldry, I. K., Glazebrook, K., Brinkmann, J., et al. 2004, ApJ, 600, 681, doi: [10.1086/380092](https://doi.org/10.1086/380092)
- Behroozi, P. S., Wechsler, R. H., & Conroy, C. 2013, ApJ, 770, 57, doi: [10.1088/0004-637X/770/1/57](https://doi.org/10.1088/0004-637X/770/1/57)
- Belli, S., Contursi, A., Genzel, R., et al. 2021, ApJL, 909, L11, doi: [10.3847/2041-8213/abe6a6](https://doi.org/10.3847/2041-8213/abe6a6)
- Berta, S., Lutz, D., Genzel, R., Förster-Schreiber, N. M., & Tacconi, L. J. 2016, A&A, 587, A73, doi: [10.1051/0004-6361/201527746](https://doi.org/10.1051/0004-6361/201527746)
- Bertin, E. 2011, in Astronomical Society of the Pacific Conference Series, Vol. 442, Astronomical Data Analysis Software and Systems XX, ed. I. N. Evans, A. Accomazzi, D. J. Mink, & A. H. Rots, 435
- Bertin, E., & Arnouts, S. 1996, A&AS, 117, 393, doi: [10.1051/aas:1996164](https://doi.org/10.1051/aas:1996164)
- Bezanson, R., Spilker, J., Williams, C. C., et al. 2019, ApJL, 873, L19, doi: [10.3847/2041-8213/ab0c9c](https://doi.org/10.3847/2041-8213/ab0c9c)
- Bezanson, R., Spilker, J. S., Suess, K. A., et al. 2022, ApJ, 925, 153, doi: [10.3847/1538-4357/ac3dfa](https://doi.org/10.3847/1538-4357/ac3dfa)
- Bland-Hawthorn, J., Tepper-García, T., Agertz, O., & Freeman, K. 2023, ApJ, 947, 80, doi: [10.3847/1538-4357/acc469](https://doi.org/10.3847/1538-4357/acc469)
- Bloom, J. S., Kulkarni, S. R., & Djorgovski, S. G. 2002, AJ, 123, 1111, doi: [10.1086/338893](https://doi.org/10.1086/338893)
- Boogaard, L. A., Decarli, R., González-López, J., et al. 2019, ApJ, 882, 140, doi: [10.3847/1538-4357/ab3102](https://doi.org/10.3847/1538-4357/ab3102)
- Boquien, M., Burgarella, D., Roehlly, Y., et al. 2019, A&A, 622, A103, doi: [10.1051/0004-6361/201834156](https://doi.org/10.1051/0004-6361/201834156)
- Bothwell, M. S., Smail, I., Chapman, S. C., et al. 2013, MNRAS, 429, 3047, doi: [10.1093/mnras/sts562](https://doi.org/10.1093/mnras/sts562)
- Bouché, N., Carfantan, H., Schroetter, I., Michel-Dansac, L., & Contini, T. 2015, AJ, 150, 92, doi: [10.1088/0004-6256/150/3/92](https://doi.org/10.1088/0004-6256/150/3/92)

- Bradley, L., Sipőcz, B., Robitaille, T., et al. 2022, *astropy/photutils*: 1.5.0, 1.5.0, Zenodo, Zenodo, doi: [10.5281/zenodo.6825092](https://doi.org/10.5281/zenodo.6825092)
- Brammer, G. B., van Dokkum, P. G., & Coppi, P. 2008, *ApJ*, 686, 1503, doi: [10.1086/591786](https://doi.org/10.1086/591786)
- Bromm, V., & Yoshida, N. 2011, *ARA&A*, 49, 373, doi: [10.1146/annurev-astro-081710-102608](https://doi.org/10.1146/annurev-astro-081710-102608)
- Buat, V., Ciesla, L., Boquien, M., Małek, K., & Burgarella, D. 2019, *A&A*, 632, A79, doi: [10.1051/0004-6361/201936643](https://doi.org/10.1051/0004-6361/201936643)
- Bundy, K., Bershad, M. A., Law, D. R., et al. 2015, *ApJ*, 798, 7, doi: [10.1088/0004-637X/798/1/7](https://doi.org/10.1088/0004-637X/798/1/7)
- Burkert, A., Genzel, R., Bouché, N., et al. 2010, *ApJ*, 725, 2324, doi: [10.1088/0004-637X/725/2/2324](https://doi.org/10.1088/0004-637X/725/2/2324)
- Caliendo, J. N., Whitaker, K. E., Akhshik, M., et al. 2021, *ApJL*, 910, L7, doi: [10.3847/2041-8213/abe132](https://doi.org/10.3847/2041-8213/abe132)
- Calzetti, D., Armus, L., Bohlin, R. C., et al. 2000, *ApJ*, 533, 682, doi: [10.1086/308692](https://doi.org/10.1086/308692)
- Caputi, K. I., Cirasuolo, M., Dunlop, J. S., et al. 2011, *MNRAS*, 413, 162, doi: [10.1111/j.1365-2966.2010.18118.x](https://doi.org/10.1111/j.1365-2966.2010.18118.x)
- Cardelli, J. A., Clayton, G. C., & Mathis, J. S. 1989, *ApJ*, 345, 245, doi: [10.1086/167900](https://doi.org/10.1086/167900)
- Carilli, C. L., & Walter, F. 2013, *ARA&A*, 51, 105, doi: [10.1146/annurev-astro-082812-140953](https://doi.org/10.1146/annurev-astro-082812-140953)
- Carles, C., Martel, H., Ellison, S. L., & Kawata, D. 2016, *MNRAS*, 463, 1074, doi: [10.1093/mnras/stw2056](https://doi.org/10.1093/mnras/stw2056)
- CASA Team, Bean, B., Bhatnagar, S., et al. 2022, *PASP*, 134, 114501, doi: [10.1088/1538-3873/ac9642](https://doi.org/10.1088/1538-3873/ac9642)
- Casey, C. M., Narayanan, D., & Cooray, A. 2014, *PhR*, 541, 45, doi: [10.1016/j.physrep.2014.02.009](https://doi.org/10.1016/j.physrep.2014.02.009)
- Chabrier, G. 2003, *PASP*, 115, 763, doi: [10.1086/376392](https://doi.org/10.1086/376392)
- Chang, Y.-Y., van der Wel, A., da Cunha, E., & Rix, H.-W. 2015, *ApJS*, 219, 8, doi: [10.1088/0067-0049/219/1/8](https://doi.org/10.1088/0067-0049/219/1/8)
- Chen, C.-C., Smail, I., Swinbank, A. M., et al. 2015, *ApJ*, 799, 194, doi: [10.1088/0004-637X/799/2/194](https://doi.org/10.1088/0004-637X/799/2/194)
- Chen, C.-C., Liao, C.-L., Smail, I., et al. 2022a, *ApJ*, 929, 159, doi: [10.3847/1538-4357/ac61df](https://doi.org/10.3847/1538-4357/ac61df)
- Chen, C.-C., Gao, Z.-K., Hsu, Q.-N., et al. 2022b, *ApJL*, 939, L7, doi: [10.3847/2041-8213/ac98c6](https://doi.org/10.3847/2041-8213/ac98c6)
- Cheng, C., Huang, J.-S., Smail, I., et al. 2023, *ApJL*, 942, L19, doi: [10.3847/2041-8213/aca9d0](https://doi.org/10.3847/2041-8213/aca9d0)
- Chown, R., Li, C., Athanassoula, E., et al. 2019, *MNRAS*, 484, 5192, doi: [10.1093/mnras/stz349](https://doi.org/10.1093/mnras/stz349)
- Conselice, C. J., Bershad, M. A., Dickinson, M., & Papovich, C. 2003, *AJ*, 126, 1183, doi: [10.1086/377318](https://doi.org/10.1086/377318)

- da Cunha, E., Groves, B., Walter, F., et al. 2013, *ApJ*, 766, 13, doi: [10.1088/0004-637X/766/1/13](https://doi.org/10.1088/0004-637X/766/1/13)
- da Cunha, E., Walter, F., Smail, I. R., et al. 2015, *ApJ*, 806, 110, doi: [10.1088/0004-637X/806/1/110](https://doi.org/10.1088/0004-637X/806/1/110)
- Daddi, E., Elbaz, D., Walter, F., et al. 2010a, *ApJL*, 714, L118, doi: [10.1088/2041-8205/714/1/L118](https://doi.org/10.1088/2041-8205/714/1/L118)
- Daddi, E., Bournaud, F., Walter, F., et al. 2010b, *ApJ*, 713, 686, doi: [10.1088/0004-637X/713/1/686](https://doi.org/10.1088/0004-637X/713/1/686)
- Daddi, E., Dannerbauer, H., Liu, D., et al. 2015, *A&A*, 577, A46, doi: [10.1051/0004-6361/201425043](https://doi.org/10.1051/0004-6361/201425043)
- Danielson, A. L. R., Swinbank, A. M., Smail, I., et al. 2011, *MNRAS*, 410, 1687, doi: [10.1111/j.1365-2966.2010.17549.x](https://doi.org/10.1111/j.1365-2966.2010.17549.x)
- Davé, R., Anglés-Alcázar, D., Narayanan, D., et al. 2019, *MNRAS*, 486, 2827, doi: [10.1093/mnras/stz937](https://doi.org/10.1093/mnras/stz937)
- Davé, R., Finlator, K., Oppenheimer, B. D., et al. 2010, *MNRAS*, 404, 1355, doi: [10.1111/j.1365-2966.2010.16395.x](https://doi.org/10.1111/j.1365-2966.2010.16395.x)
- Davidzon, I., Ilbert, O., Laigle, C., et al. 2017, *A&A*, 605, A70, doi: [10.1051/0004-6361/201730419](https://doi.org/10.1051/0004-6361/201730419)
- Davis, T. A., Greene, J. E., Ma, C.-P., et al. 2019, *MNRAS*, 486, 1404, doi: [10.1093/mnras/stz871](https://doi.org/10.1093/mnras/stz871)
- Davis, T. A., Rowlands, K., Allison, J. R., et al. 2015, *MNRAS*, 449, 3503, doi: [10.1093/mnras/stv597](https://doi.org/10.1093/mnras/stv597)
- Decarli, R., Walter, F., Aravena, M., et al. 2016, *ApJ*, 833, 70, doi: [10.3847/1538-4357/833/1/70](https://doi.org/10.3847/1538-4357/833/1/70)
- Decarli, R., Walter, F., González-López, J., et al. 2019, *ApJ*, 882, 138, doi: [10.3847/1538-4357/ab30fe](https://doi.org/10.3847/1538-4357/ab30fe)
- Decarli, R., Aravena, M., Boogaard, L., et al. 2020, *ApJ*, 902, 110, doi: [10.3847/1538-4357/abaa3b](https://doi.org/10.3847/1538-4357/abaa3b)
- Dekel, A., & Birnboim, Y. 2006, *MNRAS*, 368, 2, doi: [10.1111/j.1365-2966.2006.10145.x](https://doi.org/10.1111/j.1365-2966.2006.10145.x)
- Dekel, A., Birnboim, Y., Engel, G., et al. 2009, *Nature*, 457, 451, doi: [10.1038/nature07648](https://doi.org/10.1038/nature07648)
- Di Teodoro, E. M., & Fraternali, F. 2015, *MNRAS*, 451, 3021, doi: [10.1093/mnras/stv1213](https://doi.org/10.1093/mnras/stv1213)
- Draine, B. T., Aniano, G., Krause, O., et al. 2014, *ApJ*, 780, 172, doi: [10.1088/0004-637X/780/2/172](https://doi.org/10.1088/0004-637X/780/2/172)
- Dudzevičiūtė, U., Smail, I., Swinbank, A. M., et al. 2020, *MNRAS*, 494, 3828, doi: [10.1093/mnras/staa769](https://doi.org/10.1093/mnras/staa769)
- Dunne, L., Maddox, S. J., Papadopoulos, P. P., Ivison, R. J., & Gomez, H. L. 2022, *MNRAS*, 517, 962, doi: [10.1093/mnras/stac2098](https://doi.org/10.1093/mnras/stac2098)
- Elbaz, D., Daddi, E., Le Borgne, D., et al. 2007, *A&A*, 468, 33, doi: [10.1051/0004-6361:20077525](https://doi.org/10.1051/0004-6361:20077525)
- Elmegreen, D. M., Elmegreen, B. G., & Bellin, A. D. 1990, *ApJ*, 364, 415, doi: [10.1086/169424](https://doi.org/10.1086/169424)
- Elmegreen, D. M., Elmegreen, B. G., Marcus, M. T., et al. 2009, *ApJ*, 701, 306, doi: [10.1088/0004-637X/701/1/306](https://doi.org/10.1088/0004-637X/701/1/306)

- Emonts, B. H. C., Lehnert, M. D., Yoon, I., et al. 2023, *Science*, 379, 1323, doi: [10.1126/science.abh2150](https://doi.org/10.1126/science.abh2150)
- Endo, A., Karatsu, K., Laguna, A. P., et al. 2019, *Journal of Astronomical Telescopes, Instruments, and Systems*, 5, 035004, doi: [10.1117/1.JATIS.5.3.035004](https://doi.org/10.1117/1.JATIS.5.3.035004)
- Engel, H., Tacconi, L. J., Davies, R. I., et al. 2010, *ApJ*, 724, 233, doi: [10.1088/0004-637X/724/1/233](https://doi.org/10.1088/0004-637X/724/1/233)
- Evans, A. S., Frayer, D. T., Charmandaris, V., et al. 2022, *ApJL*, 940, L8, doi: [10.3847/2041-8213/ac9971](https://doi.org/10.3847/2041-8213/ac9971)
- Förster Schreiber, N. M., Genzel, R., Bouché, N., et al. 2009, *ApJ*, 706, 1364, doi: [10.1088/0004-637X/706/2/1364](https://doi.org/10.1088/0004-637X/706/2/1364)
- Fraser-McKelvie, A., Merrifield, M., Aragón-Salamanca, A., et al. 2020, *MNRAS*, 499, 1116, doi: [10.1093/mnras/staa2866](https://doi.org/10.1093/mnras/staa2866)
- French, K. D., Zabludoff, A. I., Yoon, I., et al. 2018, *ApJ*, 861, 123, doi: [10.3847/1538-4357/aac8de](https://doi.org/10.3847/1538-4357/aac8de)
- Freundlich, J., Combes, F., Tacconi, L. J., et al. 2019, *A&A*, 622, A105, doi: [10.1051/0004-6361/201732223](https://doi.org/10.1051/0004-6361/201732223)
- Frias Castillo, M., Hodge, J., Rybak, M., et al. 2023, *ApJ*, 945, 128, doi: [10.3847/1538-4357/acb931](https://doi.org/10.3847/1538-4357/acb931)
- Gaia Collaboration, Prusti, T., de Bruijne, J. H. J., et al. 2016, *A&A*, 595, A1, doi: [10.1051/0004-6361/201629272](https://doi.org/10.1051/0004-6361/201629272)
- Gaia Collaboration, Vallenari, A., Brown, A. G. A., et al. 2023, *A&A*, 674, A1, doi: [10.1051/0004-6361/202243940](https://doi.org/10.1051/0004-6361/202243940)
- Gao, Y., & Solomon, P. M. 1999, *ApJL*, 512, L99, doi: [10.1086/311878](https://doi.org/10.1086/311878)
- Gavazzi, G., Consolandi, G., Dotti, M., et al. 2015, *A&A*, 580, A116, doi: [10.1051/0004-6361/201425351](https://doi.org/10.1051/0004-6361/201425351)
- Gensior, J., & Kruijssen, J. M. D. 2021, *MNRAS*, 500, 2000, doi: [10.1093/mnras/staa3453](https://doi.org/10.1093/mnras/staa3453)
- Gensior, J., Kruijssen, J. M. D., & Keller, B. W. 2020, *MNRAS*, 495, 199, doi: [10.1093/mnras/staa1184](https://doi.org/10.1093/mnras/staa1184)
- Genzel, R., Tacconi, L. J., Gracia-Carpio, J., et al. 2010, *MNRAS*, 407, 2091, doi: [10.1111/j.1365-2966.2010.16969.x](https://doi.org/10.1111/j.1365-2966.2010.16969.x)
- Genzel, R., Förster Schreiber, N. M., Lang, P., et al. 2014, *ApJ*, 785, 75, doi: [10.1088/0004-637X/785/1/75](https://doi.org/10.1088/0004-637X/785/1/75)
- Genzel, R., Tacconi, L. J., Lutz, D., et al. 2015, *ApJ*, 800, 20, doi: [10.1088/0004-637X/800/1/20](https://doi.org/10.1088/0004-637X/800/1/20)
- Géron, T., Smethurst, R. J., Lintott, C., et al. 2021, *MNRAS*, 507, 4389, doi: [10.1093/mnras/stab2064](https://doi.org/10.1093/mnras/stab2064)
- Gobat, R., Daddi, E., Magdis, G., et al. 2018, *Nature Astronomy*, 2, 239, doi: [10.1038/s41550-017-0352-5](https://doi.org/10.1038/s41550-017-0352-5)

- González-López, J., Decarli, R., Pavesi, R., et al. 2019, *ApJ*, 882, 139, doi: [10.3847/1538-4357/ab3105](https://doi.org/10.3847/1538-4357/ab3105)
- Grimes, J. P., Heckman, T., Hoopes, C., et al. 2006, *ApJ*, 648, 310, doi: [10.1086/505680](https://doi.org/10.1086/505680)
- Guillard, P., Boulanger, F., Lehnert, M. D., et al. 2015, *A&A*, 574, A32, doi: [10.1051/0004-6361/201423612](https://doi.org/10.1051/0004-6361/201423612)
- Guo, Y., Jogee, S., Finkelstein, S. L., et al. 2023, *ApJL*, 945, L10, doi: [10.3847/2041-8213/acacfb](https://doi.org/10.3847/2041-8213/acacfb)
- Hamanowicz, A., Zwaan, M. A., Péroux, C., et al. 2023, *MNRAS*, 519, 34, doi: [10.1093/mnras/stac3159](https://doi.org/10.1093/mnras/stac3159)
- Harris, A. I., Baker, A. J., Frayer, D. T., et al. 2012, *ApJ*, 752, 152, doi: [10.1088/0004-637X/752/2/152](https://doi.org/10.1088/0004-637X/752/2/152)
- Harris, C. R., Millman, K. J., van der Walt, S. J., et al. 2020, *Nature*, 585, 357, doi: [10.1038/s41586-020-2649-2](https://doi.org/10.1038/s41586-020-2649-2)
- Hayashi, M., Tadaki, K.-i., Kodama, T., et al. 2018, *ApJ*, 856, 118, doi: [10.3847/1538-4357/aab3e7](https://doi.org/10.3847/1538-4357/aab3e7)
- Hayashino, T., Matsuda, Y., Tamura, H., et al. 2004, *AJ*, 128, 2073, doi: [10.1086/424935](https://doi.org/10.1086/424935)
- Hayward, C. C., Jonsson, P., Kereš, D., et al. 2012, *MNRAS*, 424, 951, doi: [10.1111/j.1365-2966.2012.21254.x](https://doi.org/10.1111/j.1365-2966.2012.21254.x)
- Hayward, C. C., Kereš, D., Jonsson, P., et al. 2011, *ApJ*, 743, 159, doi: [10.1088/0004-637X/743/2/159](https://doi.org/10.1088/0004-637X/743/2/159)
- Hayward, C. C., Narayanan, D., Kereš, D., et al. 2013, *MNRAS*, 428, 2529, doi: [10.1093/mnras/sts222](https://doi.org/10.1093/mnras/sts222)
- Hickox, R. C., Wardlow, J. L., Smail, I., et al. 2012, *MNRAS*, 421, 284, doi: [10.1111/j.1365-2966.2011.20303.x](https://doi.org/10.1111/j.1365-2966.2011.20303.x)
- Ho, L. C. 2007, *ApJ*, 668, 94, doi: [10.1086/521270](https://doi.org/10.1086/521270)
- Hodge, J. A., Smail, I., Walter, F., et al. 2019, *ApJ*, 876, 130, doi: [10.3847/1538-4357/ab1846](https://doi.org/10.3847/1538-4357/ab1846)
- Hopkins, P. F., & Elvis, M. 2010, *MNRAS*, 401, 7, doi: [10.1111/j.1365-2966.2009.15643.x](https://doi.org/10.1111/j.1365-2966.2009.15643.x)
- Hopkins, P. F., Hernquist, L., Cox, T. J., et al. 2006, *ApJS*, 163, 1, doi: [10.1086/499298](https://doi.org/10.1086/499298)
- Hopkins, P. F., Hernquist, L., Cox, T. J., & Kereš, D. 2008, *ApJS*, 175, 356, doi: [10.1086/524362](https://doi.org/10.1086/524362)
- Hsieh, B.-C., Wang, W.-H., Hsieh, C.-C., et al. 2012, *ApJS*, 203, 23, doi: [10.1088/0067-0049/203/2/23](https://doi.org/10.1088/0067-0049/203/2/23)
- Hughes, D. H., Serjeant, S., Dunlop, J., et al. 1998, *Nature*, 394, 241, doi: [10.1038/28328](https://doi.org/10.1038/28328)
- Hughes, D. H., Jáuregui Correa, J.-C., Schloerb, F. P., et al. 2010, in *Society of Photo-Optical Instrumentation Engineers (SPIE) Conference Series*, Vol. 7733, *Ground-based and Airborne Telescopes III*, ed. L. M. Stepp, R. Gilmozzi, & H. J. Hall, 773312, doi: [10.1117/12.857974](https://doi.org/10.1117/12.857974)
- Hurley, P. D., Oliver, S., Betancourt, M., et al. 2017, *MNRAS*, 464, 885, doi: [10.1093/mnras/stw2375](https://doi.org/10.1093/mnras/stw2375)

- IRSA. 2022, Spitzer Heritage Archive, doi: [10.26131/IRSA543](https://doi.org/10.26131/IRSA543)
- Iwata, I., Inoue, A. K., Matsuda, Y., et al. 2009, *ApJ*, 692, 1287, doi: [10.1088/0004-637X/692/2/1287](https://doi.org/10.1088/0004-637X/692/2/1287)
- Kato, Y., Matsuda, Y., Smail, I., et al. 2016, *MNRAS*, 460, 3861, doi: [10.1093/mnras/stw1237](https://doi.org/10.1093/mnras/stw1237)
- Kauffmann, G., Heckman, T. M., White, S. D. M., et al. 2003, *MNRAS*, 341, 54, doi: [10.1046/j.1365-8711.2003.06292.x](https://doi.org/10.1046/j.1365-8711.2003.06292.x)
- Kawabe, R. 2018, in *Atacama Large-Aperture Submm/mm Telescope (AtLAST)*, 18, doi: [10.5281/zenodo.1159037](https://doi.org/10.5281/zenodo.1159037)
- Kennicutt, R. C., J. 1981, *AJ*, 86, 1847, doi: [10.1086/113064](https://doi.org/10.1086/113064)
- Kereš, D., Katz, N., Fardal, M., Davé, R., & Weinberg, D. H. 2009, *MNRAS*, 395, 160, doi: [10.1111/j.1365-2966.2009.14541.x](https://doi.org/10.1111/j.1365-2966.2009.14541.x)
- Kereš, D., Katz, N., Weinberg, D. H., & Davé, R. 2005, *MNRAS*, 363, 2, doi: [10.1111/j.1365-2966.2005.09451.x](https://doi.org/10.1111/j.1365-2966.2005.09451.x)
- Khim, D. J., Yi, S. K., Pichon, C., et al. 2021, *ApJS*, 254, 27, doi: [10.3847/1538-4365/abf043](https://doi.org/10.3847/1538-4365/abf043)
- Kim, E., Hwang, H. S., Chung, H., et al. 2017, *ApJ*, 845, 93, doi: [10.3847/1538-4357/aa80db](https://doi.org/10.3847/1538-4357/aa80db)
- Klaassen, P. D., Mroczkowski, T. K., Cicone, C., et al. 2020, in *Society of Photo-Optical Instrumentation Engineers (SPIE) Conference Series*, Vol. 11445, *Ground-based and Airborne Telescopes VIII*, ed. H. K. Marshall, J. Spyromilio, & T. Usuda, 114452F, doi: [10.1117/12.2561315](https://doi.org/10.1117/12.2561315)
- Kohandel, M., Pallottini, A., Ferrara, A., et al. 2023, *arXiv e-prints*, arXiv:2311.05832, doi: [10.48550/arXiv.2311.05832](https://doi.org/10.48550/arXiv.2311.05832)
- Kuno, N., Sato, N., Nakanishi, H., et al. 2007, *PASJ*, 59, 117, doi: [10.1093/pasj/59.1.117](https://doi.org/10.1093/pasj/59.1.117)
- Lawrence, A., Warren, S. J., Almaini, O., et al. 2007, *MNRAS*, 379, 1599, doi: [10.1111/j.1365-2966.2007.12040.x](https://doi.org/10.1111/j.1365-2966.2007.12040.x)
- Lee, M. M., Tanaka, I., Iono, D., et al. 2021, *ApJ*, 909, 181, doi: [10.3847/1538-4357/abdbb5](https://doi.org/10.3847/1538-4357/abdbb5)
- Leja, J., Carnall, A. C., Johnson, B. D., Conroy, C., & Speagle, J. S. 2019a, *ApJ*, 876, 3, doi: [10.3847/1538-4357/ab133c](https://doi.org/10.3847/1538-4357/ab133c)
- Leja, J., Johnson, B. D., Conroy, C., et al. 2019b, *ApJ*, 877, 140, doi: [10.3847/1538-4357/ab1d5a](https://doi.org/10.3847/1538-4357/ab1d5a)
- Leroy, A. K., Bolatto, A., Gordon, K., et al. 2011, *ApJ*, 737, 12, doi: [10.1088/0004-637X/737/1/12](https://doi.org/10.1088/0004-637X/737/1/12)
- Lilly, S. J., Carollo, C. M., Pipino, A., Renzini, A., & Peng, Y. 2013, *ApJ*, 772, 119, doi: [10.1088/0004-637X/772/2/119](https://doi.org/10.1088/0004-637X/772/2/119)
- Lin, L., Li, C., Du, C., et al. 2020, *MNRAS*, 499, 1406, doi: [10.1093/mnras/staa2913](https://doi.org/10.1093/mnras/staa2913)
- Linden, S. T., Evans, A. S., Armus, L., et al. 2023, *ApJL*, 944, L55, doi: [10.3847/2041-8213/acb335](https://doi.org/10.3847/2041-8213/acb335)
- Liske, J., Baldry, I. K., Driver, S. P., et al. 2015, *MNRAS*, 452, 2087, doi: [10.1093/mnras/stv1436](https://doi.org/10.1093/mnras/stv1436)
- Lotz, J. M., Jonsson, P., Cox, T. J., et al. 2011, *ApJ*, 742, 103, doi: [10.1088/0004-637X/742/2/103](https://doi.org/10.1088/0004-637X/742/2/103)



- Lovell, C. C., Geach, J. E., Davé, R., Narayanan, D., & Li, Q. 2021, MNRAS, 502, 772, doi: [10.1093/mnras/staa4043](https://doi.org/10.1093/mnras/staa4043)
- Lower, S., Narayanan, D., Leja, J., et al. 2020, ApJ, 904, 33, doi: [10.3847/1538-4357/abbfa7](https://doi.org/10.3847/1538-4357/abbfa7)
- Madau, P., & Dickinson, M. 2014, ARA&A, 52, 415, doi: [10.1146/annurev-astro-081811-125615](https://doi.org/10.1146/annurev-astro-081811-125615)
- Maeda, F., Egusa, F., Ohta, K., Fujimoto, Y., & Habe, A. 2023, ApJ, 943, 7, doi: [10.3847/1538-4357/aca664](https://doi.org/10.3847/1538-4357/aca664)
- Maiolino, R., Nagao, T., Grazian, A., et al. 2008, A&A, 488, 463, doi: [10.1051/0004-6361:200809678](https://doi.org/10.1051/0004-6361:200809678)
- Man, A. W. S., Lehnert, M. D., Vernet, J. D. R., De Breuck, C., & Falkendal, T. 2019, A&A, 624, A81, doi: [10.1051/0004-6361/201834542](https://doi.org/10.1051/0004-6361/201834542)
- Martig, M., Bournaud, F., Teyssier, R., & Dekel, A. 2009, ApJ, 707, 250, doi: [10.1088/0004-637X/707/1/250](https://doi.org/10.1088/0004-637X/707/1/250)
- Martig, M., Crocker, A. F., Bournaud, F., et al. 2013, MNRAS, 432, 1914, doi: [10.1093/mnras/sts594](https://doi.org/10.1093/mnras/sts594)
- McDermid, R. M., Alatalo, K., Blitz, L., et al. 2015, MNRAS, 448, 3484, doi: [10.1093/mnras/stv105](https://doi.org/10.1093/mnras/stv105)
- Miettinen, O., Delvecchio, I., Smolčić, V., et al. 2017, A&A, 606, A17, doi: [10.1051/0004-6361/201730762](https://doi.org/10.1051/0004-6361/201730762)
- Mizukoshi, S., Kohno, K., Egusa, F., et al. 2021, ApJ, 917, 94, doi: [10.3847/1538-4357/ac01cc](https://doi.org/10.3847/1538-4357/ac01cc)
- Mo, H., van den Bosch, F. C., & White, S. 2010, Galaxy Formation and Evolution
- Mundy, C. J., Conselice, C. J., Duncan, K. J., et al. 2017, MNRAS, 470, 3507, doi: [10.1093/mnras/stx1238](https://doi.org/10.1093/mnras/stx1238)
- Murphy, E. J., Condon, J. J., Schinnerer, E., et al. 2011, ApJ, 737, 67, doi: [10.1088/0004-637X/737/2/67](https://doi.org/10.1088/0004-637X/737/2/67)
- Muzzin, A., Marchesini, D., Stefanon, M., et al. 2013, ApJ, 777, 18, doi: [10.1088/0004-637X/777/1/18](https://doi.org/10.1088/0004-637X/777/1/18)
- Nakamura, E., Inoue, A. K., Hayashino, T., et al. 2011, MNRAS, 412, 2579, doi: [10.1111/j.1365-2966.2010.18077.x](https://doi.org/10.1111/j.1365-2966.2010.18077.x)
- Narayanan, D., Hayward, C. C., Cox, T. J., et al. 2010, MNRAS, 401, 1613, doi: [10.1111/j.1365-2966.2009.15790.x](https://doi.org/10.1111/j.1365-2966.2009.15790.x)
- Narayanan, D., Turk, M., Feldmann, R., et al. 2015, Nature, 525, 496, doi: [10.1038/nature15383](https://doi.org/10.1038/nature15383)
- Neri, R., Genzel, R., Ivison, R. J., et al. 2003, ApJL, 597, L113, doi: [10.1086/379968](https://doi.org/10.1086/379968)
- Nesvadba, N. P. H., Boulanger, F., Salomé, P., et al. 2010, A&A, 521, A65, doi: [10.1051/0004-6361/200913333](https://doi.org/10.1051/0004-6361/200913333)
- Noll, S., Burgarella, D., Giovannoli, E., et al. 2009, A&A, 507, 1793, doi: [10.1051/0004-6361/200912497](https://doi.org/10.1051/0004-6361/200912497)

- Oh, S. H., Kim, W.-T., Lee, H. M., & Kim, J. 2008, *ApJ*, 683, 94, doi: [10.1086/588184](https://doi.org/10.1086/588184)
- Papadopoulos, P. P., Isaak, K. G., & van der Werf, P. P. 2007, *ApJ*, 668, 815, doi: [10.1086/520671](https://doi.org/10.1086/520671)
- Papadopoulos, P. P., van der Werf, P., Xilouris, E., Isaak, K. G., & Gao, Y. 2012, *ApJ*, 751, 10, doi: [10.1088/0004-637X/751/1/10](https://doi.org/10.1088/0004-637X/751/1/10)
- Pavesi, R., Sharon, C. E., Riechers, D. A., et al. 2018, *ApJ*, 864, 49, doi: [10.3847/1538-4357/aacb79](https://doi.org/10.3847/1538-4357/aacb79)
- Perley, R. A., Chandler, C. J., Butler, B. J., & Wrobel, J. M. 2011, *ApJL*, 739, L1, doi: [10.1088/2041-8205/739/1/L1](https://doi.org/10.1088/2041-8205/739/1/L1)
- Planck Collaboration, Aghanim, N., Akrami, Y., et al. 2020, *A&A*, 641, A1, doi: [10.1051/0004-6361/201833880](https://doi.org/10.1051/0004-6361/201833880)
- Puglisi, A., Daddi, E., Valentino, F., et al. 2021, *MNRAS*, 508, 5217, doi: [10.1093/mnras/stab2914](https://doi.org/10.1093/mnras/stab2914)
- Riechers, D. A., Pavesi, R., Sharon, C. E., et al. 2019, *ApJ*, 872, 7, doi: [10.3847/1538-4357/aafc27](https://doi.org/10.3847/1538-4357/aafc27)
- Riechers, D. A., Boogaard, L. A., Decarli, R., et al. 2020, *ApJL*, 896, L21, doi: [10.3847/2041-8213/ab9595](https://doi.org/10.3847/2041-8213/ab9595)
- Rizzo, F., Vegetti, S., Powell, D., et al. 2020, *Nature*, 584, 201, doi: [10.1038/s41586-020-2572-6](https://doi.org/10.1038/s41586-020-2572-6)
- Rodighiero, G., Daddi, E., Baronchelli, I., et al. 2011, *ApJL*, 739, L40, doi: [10.1088/2041-8205/739/2/L40](https://doi.org/10.1088/2041-8205/739/2/L40)
- Rodriguez-Gomez, V., Genel, S., Vogelsberger, M., et al. 2015, *MNRAS*, 449, 49, doi: [10.1093/mnras/stv264](https://doi.org/10.1093/mnras/stv264)
- Rosas-Guevara, Y., Bonoli, S., Dotti, M., et al. 2022, *MNRAS*, 512, 5339, doi: [10.1093/mnras/stac816](https://doi.org/10.1093/mnras/stac816)
- Rudnick, G., Hodge, J., Walter, F., et al. 2017, *ApJ*, 849, 27, doi: [10.3847/1538-4357/aa87b2](https://doi.org/10.3847/1538-4357/aa87b2)
- Saintonge, A., Catinella, B., Tacconi, L. J., et al. 2017, *ApJS*, 233, 22, doi: [10.3847/1538-4365/aa97e0](https://doi.org/10.3847/1538-4365/aa97e0)
- Sanders, D. B., & Mirabel, I. F. 1996, *ARA&A*, 34, 749, doi: [10.1146/annurev.astro.34.1.749](https://doi.org/10.1146/annurev.astro.34.1.749)
- Sargent, M. T., Béthermin, M., Daddi, E., & Elbaz, D. 2012, *ApJL*, 747, L31, doi: [10.1088/2041-8205/747/2/L31](https://doi.org/10.1088/2041-8205/747/2/L31)
- Sargent, M. T., Daddi, E., Bournaud, F., et al. 2015, *ApJL*, 806, L20, doi: [10.1088/2041-8205/806/1/L20](https://doi.org/10.1088/2041-8205/806/1/L20)
- Schlegel, D. J., Finkbeiner, D. P., & Davis, M. 1998, *ApJ*, 500, 525, doi: [10.1086/305772](https://doi.org/10.1086/305772)
- Schreiber, C., Pannella, M., Elbaz, D., et al. 2015, *A&A*, 575, A74, doi: [10.1051/0004-6361/201425017](https://doi.org/10.1051/0004-6361/201425017)
- Simmons, B. D., Melvin, T., Lintott, C., et al. 2014, *MNRAS*, 445, 3466, doi: [10.1093/mnras/stu1817](https://doi.org/10.1093/mnras/stu1817)
- Simons, R. C., Kassin, S. A., Weiner, B. J., et al. 2017, *ApJ*, 843, 46, doi: [10.3847/1538-4357/aa740c](https://doi.org/10.3847/1538-4357/aa740c)
- Smail, I., Ivison, R. J., & Blain, A. W. 1997, *ApJL*, 490, L5, doi: [10.1086/311017](https://doi.org/10.1086/311017)

- Smail, I., Dudzevičiūtė, U., Stach, S. M., et al. 2021, MNRAS, 502, 3426, doi: [10.1093/mnras/stab283](https://doi.org/10.1093/mnras/stab283)
- Smail, I., Dudzeviciute, U., Gurwell, M., et al. 2023, arXiv e-prints, arXiv:2306.16039, doi: [10.48550/arXiv.2306.16039](https://doi.org/10.48550/arXiv.2306.16039)
- Solomon, P. M., & Vanden Bout, P. A. 2005, ARA&A, 43, 677, doi: [10.1146/annurev.astro.43.051804.102221](https://doi.org/10.1146/annurev.astro.43.051804.102221)
- Speagle, J. S. 2020, MNRAS, 493, 3132, doi: [10.1093/mnras/staa278](https://doi.org/10.1093/mnras/staa278)
- Speagle, J. S., Steinhardt, C. L., Capak, P. L., & Silverman, J. D. 2014, ApJS, 214, 15, doi: [10.1088/0067-0049/214/2/15](https://doi.org/10.1088/0067-0049/214/2/15)
- Spilker, J., Bezanson, R., Barišić, I., et al. 2018, ApJ, 860, 103, doi: [10.3847/1538-4357/aac438](https://doi.org/10.3847/1538-4357/aac438)
- Springel, V., White, S. D. M., Jenkins, A., et al. 2005, Nature, 435, 629, doi: [10.1038/nature03597](https://doi.org/10.1038/nature03597)
- Stach, S. M., Smail, I., Amvrosiadis, A., et al. 2021, MNRAS, 504, 172, doi: [10.1093/mnras/stab714](https://doi.org/10.1093/mnras/stab714)
- Stalevski, M., Ricci, C., Ueda, Y., et al. 2016, MNRAS, 458, 2288, doi: [10.1093/mnras/stw444](https://doi.org/10.1093/mnras/stw444)
- Strateva, I., Ivezić, Ž., Knapp, G. R., et al. 2001, AJ, 122, 1861, doi: [10.1086/323301](https://doi.org/10.1086/323301)
- Tacconi, L. J., Genzel, R., & Sternberg, A. 2020, ARA&A, 58, 157, doi: [10.1146/annurev-astro-082812-141034](https://doi.org/10.1146/annurev-astro-082812-141034)
- Tacconi, L. J., Genzel, R., Smail, I., et al. 2008, ApJ, 680, 246, doi: [10.1086/587168](https://doi.org/10.1086/587168)
- Tacconi, L. J., Genzel, R., Neri, R., et al. 2010, Nature, 463, 781, doi: [10.1038/nature08773](https://doi.org/10.1038/nature08773)
- Tacconi, L. J., Neri, R., Genzel, R., et al. 2013, ApJ, 768, 74, doi: [10.1088/0004-637X/768/1/74](https://doi.org/10.1088/0004-637X/768/1/74)
- Tacconi, L. J., Genzel, R., Saintonge, A., et al. 2018, ApJ, 853, 179, doi: [10.3847/1538-4357/aaa4b4](https://doi.org/10.3847/1538-4357/aaa4b4)
- Tadaki, K.-i., Kodama, T., Nelson, E. J., et al. 2017, ApJL, 841, L25, doi: [10.3847/2041-8213/aa7338](https://doi.org/10.3847/2041-8213/aa7338)
- Tamura, Y., Saito, T., Tsuru, T. G., et al. 2014, ApJL, 781, L39, doi: [10.1088/2041-8205/781/2/L39](https://doi.org/10.1088/2041-8205/781/2/L39)
- Tamura, Y., Kohno, K., Nakanishi, K., et al. 2009, Nature, 459, 61, doi: [10.1038/nature07947](https://doi.org/10.1038/nature07947)
- Tasca, L. A. M., Le Fèvre, O., Ribeiro, B., et al. 2017, A&A, 600, A110, doi: [10.1051/0004-6361/201527963](https://doi.org/10.1051/0004-6361/201527963)
- Thomas, D., Maraston, C., Schawinski, K., Sarzi, M., & Silk, J. 2010, MNRAS, 404, 1775, doi: [10.1111/j.1365-2966.2010.16427.x](https://doi.org/10.1111/j.1365-2966.2010.16427.x)
- Tomczak, A. R., Quadri, R. F., Tran, K.-V. H., et al. 2014, ApJ, 783, 85, doi: [10.1088/0004-637X/783/2/85](https://doi.org/10.1088/0004-637X/783/2/85)
- Tsukui, T., Wisnioski, E., Bland-Hawthorn, J., et al. 2023, arXiv e-prints, arXiv:2308.14798, doi: [10.48550/arXiv.2308.14798](https://doi.org/10.48550/arXiv.2308.14798)
- Umehata, H., Tamura, Y., Kohno, K., et al. 2014, MNRAS, 440, 3462, doi: [10.1093/mnras/stu447](https://doi.org/10.1093/mnras/stu447)
- Valentino, F., Magdis, G. E., Daddi, E., et al. 2018, ApJ, 869, 27, doi: [10.3847/1538-4357/aaeb88](https://doi.org/10.3847/1538-4357/aaeb88)

- van de Voort, F., Davis, T. A., Matsushita, S., et al. 2018, MNRAS, 476, 122, doi: [10.1093/mnras/sty228](https://doi.org/10.1093/mnras/sty228)
- van der Tak, F. F. S., Black, J. H., Schöier, F. L., Jansen, D. J., & van Dishoeck, E. F. 2007, A&A, 468, 627, doi: [10.1051/0004-6361:20066820](https://doi.org/10.1051/0004-6361:20066820)
- Virtanen, P., Gommers, R., Oliphant, T. E., et al. 2020, Nature Methods, 17, 261, doi: [10.1038/s41592-019-0686-2](https://doi.org/10.1038/s41592-019-0686-2)
- Walter, F., Weiß, A., Downes, D., Decarli, R., & Henkel, C. 2011, ApJ, 730, 18, doi: [10.1088/0004-637X/730/1/18](https://doi.org/10.1088/0004-637X/730/1/18)
- Walter, F., Decarli, R., Aravena, M., et al. 2016, ApJ, 833, 67, doi: [10.3847/1538-4357/833/1/67](https://doi.org/10.3847/1538-4357/833/1/67)
- Wang, J., Athanassoula, E., Yu, S.-Y., et al. 2020, ApJ, 893, 19, doi: [10.3847/1538-4357/ab7fad](https://doi.org/10.3847/1538-4357/ab7fad)
- Webb, T. M. A., Yamada, T., Huang, J. S., et al. 2009, ApJ, 692, 1561, doi: [10.1088/0004-637X/692/2/1561](https://doi.org/10.1088/0004-637X/692/2/1561)
- Weinberger, R., Springel, V., Hernquist, L., et al. 2017, MNRAS, 465, 3291, doi: [10.1093/mnras/stw2944](https://doi.org/10.1093/mnras/stw2944)
- Whitaker, K. E., Pope, A., Cybulski, R., et al. 2017, ApJ, 850, 208, doi: [10.3847/1538-4357/aa94ce](https://doi.org/10.3847/1538-4357/aa94ce)
- Whitaker, K. E., van Dokkum, P. G., Brammer, G., & Franx, M. 2012, ApJL, 754, L29, doi: [10.1088/2041-8205/754/2/L29](https://doi.org/10.1088/2041-8205/754/2/L29)
- Williams, C. C., Spilker, J. S., Whitaker, K. E., et al. 2021, ApJ, 908, 54, doi: [10.3847/1538-4357/abcbf6](https://doi.org/10.3847/1538-4357/abcbf6)
- Woodrum, C., Williams, C. C., Rieke, M., et al. 2022, ApJ, 940, 39, doi: [10.3847/1538-4357/ac9af7](https://doi.org/10.3847/1538-4357/ac9af7)
- Wuyts, S., Förster Schreiber, N. M., van der Wel, A., et al. 2011, ApJ, 742, 96, doi: [10.1088/0004-637X/742/2/96](https://doi.org/10.1088/0004-637X/742/2/96)
- Yamada, T., Nakamura, Y., Matsuda, Y., et al. 2012, AJ, 143, 79, doi: [10.1088/0004-6256/143/4/79](https://doi.org/10.1088/0004-6256/143/4/79)
- Yu, S.-Y., & Ho, L. C. 2020, ApJ, 900, 150, doi: [10.3847/1538-4357/abac5b](https://doi.org/10.3847/1538-4357/abac5b)
- Yu, S.-Y., Xu, D., Ho, L. C., Wang, J., & Kao, W.-B. 2022a, A&A, 661, A98, doi: [10.1051/0004-6361/202142533](https://doi.org/10.1051/0004-6361/202142533)
- Yu, S.-Y., Kalinova, V., Colombo, D., et al. 2022b, A&A, 666, A175, doi: [10.1051/0004-6361/202244306](https://doi.org/10.1051/0004-6361/202244306)
- Zakamska, N. L., Hamann, F., Pâris, I., et al. 2016, MNRAS, 459, 3144, doi: [10.1093/mnras/stw718](https://doi.org/10.1093/mnras/stw718)
- Zavala, J. A., Casey, C. M., Manning, S. M., et al. 2021, ApJ, 909, 165, doi: [10.3847/1538-4357/abdb27](https://doi.org/10.3847/1538-4357/abdb27)